Forschungszentrum Karlsruhe
in der Helmholtz-Gemeinschaft

Wissenschaftliche Berichte
FZKA 7240

Regional Climate Change and the Impact on Hydrology in the Volta Basin of West Africa

G. Jung

Institut für Meteorologie und Klimaforschung

Oktober 2006

Forschungszentrum Karlsruhe

in der Helmholtz-Gemeinschaft

Wissenschaftliche Berichte
FZKA 7240

Regional Climate Change and the Impact on Hydrology in the Volta Basin of West Africa

Gerlinde Jung

Institut für Meteorologie und Klimaforschung

von der Fakultät für Naturwissenschaften
der Universität Augsburg
genehmigte Dissertation

Forschungszentrum Karlsruhe GmbH, Karlsruhe
2006

Forschungszentrum Karlsruhe GmbH
Postfach 3640, 76021 Karlsruhe

Mitglied der Hermann von Helmholtz-Gemeinschaft
Deutscher Forschungszentren (HGF)

ISSN 0947-8620

urn:nbn:de:0005-072407

Abstract

The Volta Basin is a climate sensitive, semi-arid to sub-humid region in West Africa. Livelihood of the population is mainly dependent on agriculture and therefore highly vulnerable to rainfall variability and climate change. For an investigation of the impact of a possible global climate change to regional climate and surface, as well as sub-surface hydrology in the region of the Volta Basin, coupled regional climate-hydrology simulations were performed. Therefore, the mesoscale meteorological model MM5 was set up, fully coupled to a 1-dimensional SVAT (Soil Vegetation Atmosphere Transfer) model, to account for soil-atmosphere feedback mechanisms. After a validation was performed, MM5 was used as a regional climate model to simulated two 10-years time slices: 1991-2000 and 2030-2039. The emission scenario IS92a output of the global climate model ECHAM4 was downscaled dynamically, to a final resolution of 9km, for the Volta Basin. These regional climate simulations were then coupled to the physically based, distributed hydrological model WaSiM, after the calibration and adaptation of the hydrological model to the study region.

A comparison the GCM output, as well as the RCM output for present-day climate simulation to observations showed a wet bias over the Sahel and a sufficient accuracy in temperature representation for the ECHAM4, present-day simulation (1961-1990). In the regional climate simulations, the displacement of the Inter Tropical Discontinuity (ITD) to the North at the beginning of the rainy season, as well as the displacement South, at the end occur too early. Rainfall also showed a negative deviation along the coast but a sufficient accuracy in the Volta Basin.

The results of the MM5 and WaSiM simulations show an annual mean temperature increase by 1.2-1.3°C in West Africa and the Volta Basin. This temperature change significantly exceeds inter-annual variability. Mean annual precipitation increases for both, the sahelian and the coastal region of West Africa. Averaged over the region of the Volta Basin, this increase is about 5%. Only in the Sahel, the mean annual change signal exceeds simulated inter-annual variability. Spatially the increase is highly heterogeneous, reaching from -20% to +50%. A dipole pattern of rainfall variability in the Sahel and the Guinea Coast region was detected for June and July. An overall increase in precipitation was found for September, and a strong decrease for April. Causes for the rainfall variability were found in the dynamics of the Tropical Easterly Jet (TEJ), the African Easterly Jet (AEJ) and in the position of the ITD. For the Volta basin it is demonstrated, that the decrease in April at the beginning of the rainy season is not only connected to smaller rainfall amounts, but also to a delay in the onset of the rainy season. In addition, inter-annual variability in the Volta Basin increases in the early stage of the rainy season, while annual mean aridity in the Volta Basin does not change significantly.

No significant changes in discharge follow the precipitation decrease at the onset of the rainy season. During the rainy season, most of the surplus rainfall evaporates, due to the increase in potential evaporation, as a consequence of higher near surface air temperatures.

The study demonstrates the ability of the coupled modelling system to reasonably simulate West African climate and hydrology conditions. For the selected scenario and time slices, the change signal in precipitation, as well as surface and subsurface hydrology variables lies with few exceptions, within the range of inter-annual variability, whereas temperature shows a clear increase.

Regionaler Klimawandel und der Einfluss auf die Hydrologie des Volta Beckens in West Afrika

Das Volta Becken ist eine klimasensitive, semi-aride bis sub-humide Region in West Afrika. Der wichtigste Wirtschaftsfaktor ist die Landwirtschaft. Demnach sind die Lebensbedingungen der Bevölkerung stark von der Variabilität des Niederschlags und von Klimaänderungen abhängig. Um den Einfluß einer globalen Klimaänderung auf das regionale Klima und die Hydrologie des Volta Beckens zu untersuchen, wurden gekoppelte regionale Klima-Hydrologiesimulationen durchgeführt. Dabei wurde das mesoskalige meteorologische Modell MM5 verwendet. Nach einer durchgeführten Modellvalidierung wurde MM5 als regionales Klimamodell eingesetzt, um zwei Zeitscheiben von je 10 Jahren zu berechnen: 1991-2000 und 2030-2039. Dabei wurde Output des globalen Klimamodells (GCM) ECHAM4 (Szenario: IS92a) dynamisch bis auf eine Auflösung von 9 km für die Region des Volta Beckens herunterskaliert. Nach der Kalibrierung des physikalisch basierten, flächendifferenzierten hydrologischen Modells WaSiM und dessen Anpassung an das Untersuchungsgebiet wurde dieses an die regionalen Klimasimulationen gekoppelt.

Bei einem Vergleich, sowohl des GCM, als auch des RCM Outputs für das Jetztzeitklima mit Beobachtungen war der Sahel zu niederschlagsreich. Die Temperatur der ECHAM4 Simulation zeigte eine ausreichende Genauigkeit. Die Verlagerung der Innertropischen Diskontinuität (ITD) geschah in den regionalen Klimasimulationen sowohl zu Beginn der Regenzeit nach Norden, als auch am Ende der Regenzeit nach Süden, zu schnell. Der simulierte Niederschlag zeigte, verglichen mit langjährigen Beobachtungen, einen negativen Bias im Küstenbereich, jedoch eine ausreichende Genauigkeit im Volta Becken.

Die Ergebnisse der MM5 und WaSiM Simulationen zeigen einen mittleren jährlichen Temperaturanstieg von 1.2-1.3°C in West Afrika und dem Volta Becken. Diese Temperaturänderung übersteigt die interannuelle Variabilität deutlich. Der mittlere Jahresniederschlag für sowohl den Sahel als auch die Küstenregion nimmt zu. Im Mittel über das Volta Becken liegt diese Zunahme bei 5%. Nur im Sahel übersteigt das mittlere jährliche Änderungssignal die simulierte interannuelle Variabilität. Räumlich ist die Niederschlagsänderung sehr heterogen mit Werten zwischen -20% und +50%. Im Juni und Juli wurde ein Dipolmuster der Niederschlagsvariabilität im Sahel und der Küstenregion ermittelt. Der September zeigt einen genereller Anstieg des Niederschlags im gesamten Gebiet, der April dagegen eine starke Abnahme. Erklärungsansätze für die Niederschlagsvariabilität finden sich in der Dynamik des Tropical Easterly Jet (TEJ), des African Easterly Jet (AEJ) und in der Lage der ITD. Für das Volta Becken wurde gezeigt, dass die Niederschlagsabnahme im April, zu Beginn der Regenzeit, nicht nur mit geringeren Niederschlagsmengen im Zusammenhang steht, sondern auch mit einem verspäteten Eintreten der Regenzeit. Zusätzlich nimmt die interannuelle Variabilität im Volta Becken in der ersten Phase der Regenzeit zu, während die Aridität im Jahresmittel keine signifikante Änderung aufweist. Der Niederschlagsabnahme im April folgen keine signifikanten Änderungen im Abfluss. Aufgrund der Zunahme der potentiellen Verdunstung durch die Temperaturzunahme geht während der Regenzeit der Hauptanteil des zusätzlichen Niederschlags als Verdunstung verloren.

Diese Untersuchung demonstriert die Eignung des gekoppelten Modellsystems, das Klima und die Hydrolgie in West Afrika angemessen abzubilden. Für das ausgewählte Szenario und die ausgewählten Zeitscheiben liegt das Klimaänderungssignal sowohl im Niederschlag, als auch in den hydrologischen Variablen mit wenigen Ausnahmen im Bereich der interannuellen Variabilität. Dagegen zeigt die Temperature eine klare Zunahme.

Contents

Abbreviations

AEJ	African Easterly Jetstream
AEW	African Easterly Waves
AGCM	Atmosphere Global Circulation Model
AOGCM	Atmosphere Ocean Global Circulation Model
AWD	African Wave Disturbance
CRU	Climate Research Unit
DEM	Digital Elevation Model
dMI	de Martonne Aridity Index
DOY	Day Of Year
ECMWF	European Centre for Medium-Range Weather Forecasts
GCM	Global Circulation Model
GDP	Gross Domestic Product
GHG	Greenhouse Gas
IDW	Inverse Distance Weighting
ITCZ	Inter Tropical Convergence Zone
ITD	Inter Tropical Discontinuity
LAI	Leaf Area Index
LAM	Limited Area Model
LSM	Land Surface Model
MM5	Mesoscale Meteorological Model
MSLP	Mean Sea Level Pressure
NCAR	National Center for Atmospheric Research
NCEP	National Centers for Environmental Prediction
NSE (NSM)	Nash-Sutcliffe Efficiency
OGCM	Ocean General Circulation Model
PEST	Parameter Estimation Tool
PSU	Penn State University
RCM	Regional Climate Model
RMSE	Root Mean Square Error
SAT	Surface Air Temperature
SN	Signal to Noise Ratio
SST	Sea Surface Temperature
STJ	Subtropical Jetstream
SVAT	Soil Vegetation Atmosphere Transfer
TEJ	Tropical Easterly Jetstream
WAM	West African Monsoon
WaSiM	Water Balance Simulation Model

List of Figures

List of Tables

Chapter 1

Introduction and Objectives

Human impact on climate

Since mankind started agriculture, around 8000 years ago, their activities have influenced the climate system. The changes in land-use induced by human beings first comprised deforestation and drainage of wetlands.

One reason for an increase in anthropogenic impacts on the climate system can be found in an increase in the world's population. Until 1500 approximately 500 million people populated the entire globe, approximately twice as many as during the times from the settlement of Homo Sapiens on earth, 50.000 years before, to the Roman Empire (Bliefert, 1997). Population doubled once again from 1500 to 1900, and has now reached a number of around 6.5 billion people living on Earth. This development lead to an intensification of land-use through a higher demand for agricultural productivity. Over the last 200 years the use of nitrogen fertilizers, increasing animal breeding and rice growing wetlands lead to higher emissions of methane (CH_4) and nitrous oxide (N_2O) to the atmosphere. Industrialization, starting in the 19th century, caused an additional modification of the composition of the atmosphere. The dominant factor in developed countries, with their transport and industrial sectors is the increase in NO_x and CO_2 emissions from burning of fossil fuels. This increase in CO_2 and other so called greenhouse gases is believed to have contributed to the global warming, that is observed over the last century and has intensified since 1970.

The greenhouse effect was first described by Svant August Arrhenius in 1896 (Bliefert, 1997). The most important gases contributing to the greenhouse effect through their ability to absorb and emit long-wave radiation, are water vapour (H_2O) and carbon dioxide (CO_2). The largest component of the greenhouse warming is 'natural', preventing the earth from its atmosphere-less energy balanced temperature of around -18°C. This natural greenhouse effect globally accounts for a warming of about 33°C. The anthropogenic influence on atmospheric composition therefore means an additional radiative forcing. The two main factors responsible are agriculture and the burning of fossil fuels. Agriculture accounts for approximately 23% of the CO_2, 60% of the CH_4 emissions and 23% of the N_2O emissions world wide (Bliefert, 1997).

As the most important component of this additional greenhouse gas forcing, global CO_2 concentrations have increased from a preindustrial level of 280 ppmv to 370 ppmv at the beginning of the 21st century, accounting for a radiative forcing of over 1.5 W m^{-2}. Also CH_4 emissions increased remarkably from 0.7 to 1.7 ppmv, equaling 0.5 W

m^{-2} of radiative forcing (RAMASWAMY et al., 2001). Increases in N_2O and a variety of halocarbons do additionally contribute to the anthropogenic forcing of the greenhouse effect. Tropospheric ozone leads to a positive radiative forcing as well, whereas due to the decrease of the ozone layer in the stratosphere, stratospheric ozone evokes a negative radiative forcing. Including a high degree of uncertainty, aerosols also contribute to the radiative forcing, through direct (radiation scattering, absorption and emission), as well as indirect effects on cloud properties.

Some non-anthropogenic mechanisms contributing to the overall radiative forcing should not be forgotten. For example, the variability in solar activity leads to a forcing of 0.2 - 0.3 W m^{-2} since 1850. Another example is volcanic activity that leads to temporally limited (in the order of years), but nevertheless strong influences, such as the eruption of Mt. Pinatubo in 1991 demonstrated, with a forcing of -4 W m^{-2} (RAMASWAMY et al., 2001). These values all represent the forcing at the global scale and can vary significantly at regional scales (HOUGHTON et al., 1995).

From data that are available from the middle of the 19th century, an increase in annual mean global temperature of 0.6 °C per century was observed since 1900. Since 1976, temperatures have risen approximately three times faster. The largest increase was observed in regions between 40-70°N in winter and springtime. Precipitation shows an increase between 55°-85°N and a decrease south of 40°N in the northern hemisphere. For the southern hemisphere no reliable conclusion can be drawn (WMO, 2002).

This development in global climate and the impact of mankind motivated attempts to estimate the impacts of anthropogenic modification of the atmospheric composition on future climate. Therefore, emission scenarios were established (HOUGHTON et al., 1995), that incorporate different assumptions about socio-economic, technologic and demographic development, to estimate the increase in greenhouse gases. A variety of global circulation models (GCMs) worldwide use these scenarios, to investigate the range of possible future climate conditions. For a simulation of the local effect of these global change perspectives, regional climate models are used. These determine the respective local climate, and can furthermore deliver input fields for regional climate change impact studies in different scientific disciplines. The impact on hydrology raises different questions. Where in midlatitudes the impacts on extreme events like floods or on hydropower generation is at issue, for the climate sensitive region of West Africa and the Volta Basin, the impact on water availability is of particular interest.

The Volta Basin

The Volta Basin is situated in a semi-arid to sub-humid environment of West Africa (figure 1.1). It covers an area of 414000 km^2. The countries that share over 80% of the basins' area are Burkina Faso (42.07%) and Ghana (40.25%). Almost half of Togo forms part of the Volta Basin as well, with a share of 6.25% of the basin area. The other countries that occupy minor parts of the Volta Basin are Benin, Mali and Ivory Coast (OBENG-ASIEDU, 2004).

The livelihood of the population is mainly dependent on rain-fed agriculture, especially in the northern part of the basin. Furthermore, energy production, and therefore development potential, especially in Ghana is linked to hydropower production at Akosombo Dam in the South of the basin. This dam was built in 1965, not long after Ghana reached

Figure 1.1: Location of the Volta Basin, basin area: 414.000 km^2 (Satellite image: *http://earth.google.com*)

independence as the first West African state in 1957. The construction of the dam led to the formation of one of the largest artificial lakes in the world - Lake Volta. With the damming of the lake, energy and water demanding industries, like the aluminium industry, settled in southern Ghana, pushing the countries economic development a large step forward. Now Ghana with a GDP of 1302$ per capita (WHO, 2005) is one out of few African countries that looks optimistically to the future. Main economic income sources are gold, cocoa and tourism. In Burkina Faso agriculture is the main economic sector due to the lack of exploitable natural resources. Subsequently Burkina Faso is still one of the five poorest countries of the world, with a GDP of 885$ per capita (WHO, 2005) and even more dependent than Ghana on sufficient rainfall amounts for agricultural production.

Due to the increasing population pressure, a growth in irrigated areas can be observed, especially in the Burkinabè and the northern Ghanaian part of the basin, where water is scarce. Population growth rates are 2.3% in Ghana, and 2.9% in Burkina Faso (WHO, 2005) with a total population of 15-20 million people in the entire Volta Basin. These factors lead to competing water demands from the Volta River Authority for energy production,

and from farmers in upstream areas for agriculture. This is especially intensifying, when the increasing demand in hydropower, as well as in water for irrigation purposes meets suboptimal climatic conditions, like extremely dry years.

Precipitation intensities, as well as annual rainfall amounts in West Africa show a strong inter-annual, inter-decadal and even intra-seasonal variability. Therefore the vulnerability to climate change and variability will increase in West African and the Volta Basin, as long as population growth continues at high levels.

Decreasing rainfall amounts and increasing temperatures have been observed in West Africa over the past decades and analyzed in a variety of studies (LeBarbé et al., 2002; Servant et al., 1998; Amani, 2001; Nicholson, 1993, 2001; Hulme et al., 2001). A striking decrease in annual rainfall in the Sahel region occurred, with a decrease of around 20 to 40% from 1931-60 to 1968-97 (Nicholson, 2001).

This development lead to increasing scientific efforts to understand West African climate and its variability and to estimate future climate conditions within the region.

Objectives

The problems associated with global climate change outlined above, and their impacts on regional climate and hydrology, in combination with the specific regional economic and socio-economic conditions in the Volta Basin lead to a central research question, the estimation of the influence of a globally changing climate on water availability. The objective of the present work is the simulation and analysis of the impact of a globally changing climate on regional climate conditions, as well as surface and subsurface hydrology in the Volta Basin. The main concern within this scientifically challenging work concentrates on rainfall, rainfall variability, as well as the impact of temperature and precipitation changes to surface runoff, as well as groundwater recharge. To meet this task, within the present study, coupled regional climate - hydrology simulations were performed. This included the setup and adaptation of the models to the study region, the calibration and validation of the models, as well as the performance of the coupled simulations. In the validation a particular focus was set on the comparison of simulated and observed present-day climate conditions, as well as on model intercomparison on different scales. Within the analysis of the modelling results, one central objective of the study was to identify the climate change signal with respect to simulated climate variability in the region. This was achieved through the definition of a signal-to-noise ratio for various meteorological and hydrological model outputs.

Innovation

Innovative work, performed within the scope of this thesis included:

- High resolution (9 km) regional climate simulations are still rarely performed, and have not been performed for a West African environment before.

- A physically based, distributed hydrological model run for a catchment of the scale of the Volta, in a comparable fine resolution (1 km), was seldom performed before and is new for West Africa.

- The coupling of climate and hydrological models for impact analysis is a relatively new development. Coupled models have not been used previously for the assessment of the impacts of climate change in a West African basin.

The GLOWA-Volta project

This study was performed within the framework of the GLOWA-Volta project (*www.glowa-volta.de*). The GLOWA-Volta project is a science project, funded by the BMBF (*German Ministry for Education and Research*). The main aim of the project is to develop a decision support tool for water sector decision makers. The decision support process is intended to address the main questions of water availability of the region. Therefore natural scientists, investigating the hydrological cycle of the Volta Basin are working in close cooperation with social scientists and economists, who analyze social and political structures, as well as economic development potential and its impact on water use.

Outline of the thesis

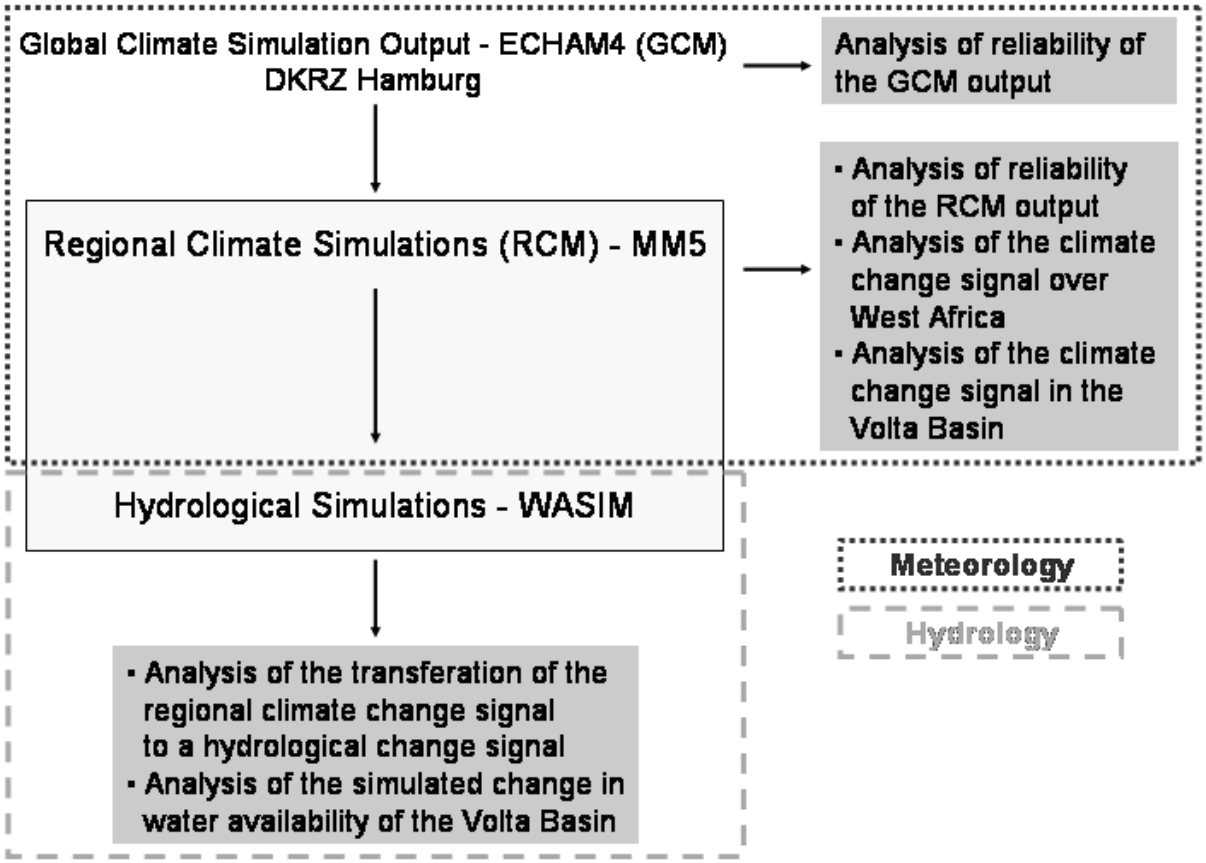

Figure 1.2: Structure of the thesis

The present thesis forms a combination of hydrological and meteorological sciences, with a strong focus on modelling. Within the study, a dynamical downscaling of output of

the global climate model ECHAM4 of the emission scenario IS92a was performed for two time slices, using the mesoscale meteorological model MM5 as a regional climate model. A reference state climate for the time slice 1991-2000 and a proposed future climate scenario for 2030-2039 were simulated. The regional climate model output is then passed as input to the physically based, distributed hydrological model WaSiM, for an impact analysis of future water availability of the Volta Basin.

CHAPTER 2, begins with an overview over the meteorology, climate and hydrology of the study region.

CHAPTER 3 gives a short overview of the topic of global and regional climate modelling, as well as hydrological modelling, and provides some examples of climate and hydrology modelling approaches for West Africa, and coupled climate-hydrology modelling in general.

This is followed in CHAPTER 4 by a short description of the modelling system, including the emission scenario used, the global climate model ECHAM4, the mesoscale meteorological model MM5, and the hydrological model WaSiM.

In CHAPTER 5 the setup of the regional climate model and the hydrological model is described in detail. Within this chapter the calibration procedure for the hydrological model is included. In addition the technical realisation of the simulations and the coupling procedure are described.

CHAPTER 6 summarizes the validation of the modelling system. First, the global climate output of ECHAM4 is analysed for its reliability in simulating present-day climate conditions, and MM5 is validated for regular hindcasts, using reanalysis data as input to achieve an insight into the general performance of MM5 for the Volta Basin. In addition, the reliability of the regional climate simulations, with respect to mean present-day climate conditions is analysed. Furthermore, the validation of the coupled modelling system, with respect to river runoff is illustrated. Finally, this chapter offers a brief discussion of the coupled climate-hydrology simulations against the background of modelling uncertainties.

In CHAPTER 7, the results of the regional climate simulations, as well as the coupled climate-hydrology simulations are presented. Within this chapter, first an analysis of the climate change signal of the meteorology and large-scale dynamics of West Africa is performed. This is followed by an analysis of climate change within the region of the Volta Basin, with a focus on temperature, precipitation, aridity and the onset of the rainy season. The analysis of results concludes with an investigation of changes in land-surface hydrology components for the entire Volta Basin and its subcatchments. Finally this chapter closes with a discussion of the results obtained.

CHAPTER 8 gives a short summary and conclusion of the thesis, and an outlook to possible future investigations.

Chapter 2

Climate and Hydrology of the Volta Basin

2.1 Climate of the Volta Basin and Large Scale Dynamics

The climate of the Volta Basin can be described as semi-arid to sub-humid. In a semi-arid climate potential evaporation exceeds precipitation in 6-9 months. In contrast, a climate is defined as sub-humid, when in 6-9 months precipitation exceeds potential evaporation (Hayward and Oguntoyinbo, 1987). Furthermore, the rainfall regime with its division into dry and rainy season is influenced by the *West African Monsoon* (WAM).

Temperature Mean annual temperature in the Volta Basin lies between 27 and 36°C in the northern part, with an annual range of 9°C (Oguntunde, 2004) and a daily range of 8-14°C. In the South of the basin, annual temperature range is around 6°C, from 24°C in August, to 30°C in March. Daily temperature range is about 3-5°C (Hayward and Oguntoyinbo, 1987).

Evaporation Mean annual potential evaporation is lower than 1500 mm in the South, but exceeds 2500 mm in the North of the basin. Evapotranspiration accounts for approximately 80% of the rainfall amount during the rainy season (Oguntunde, 2004). Real evapotranspiration within the basin lies between 10 mm/d in the rainy season and 2 mm/d in the dry season, and mainly depends on soil moisture (Martin, 2005).

Precipitation Around 80% of annual rainfall occurs from July to September with the monsoonal rains. Mean annual precipitation ranges from less than 300 mm up to more than 1500 mm, showing a strong North-South gradient, with higher rainfall amounts in the tropical South and smaller amounts in the semi-arid North of the basin. In addition, in the south-western corner of Ghana, which is actually not part of the Volta Basin, annual precipitation exceeds 2100 mm, whereas in south-eastern Ghana it's less than 800 mm. This shows, that not only a North-South gradient is apparent, but also a quite strong West-East gradient can be found.

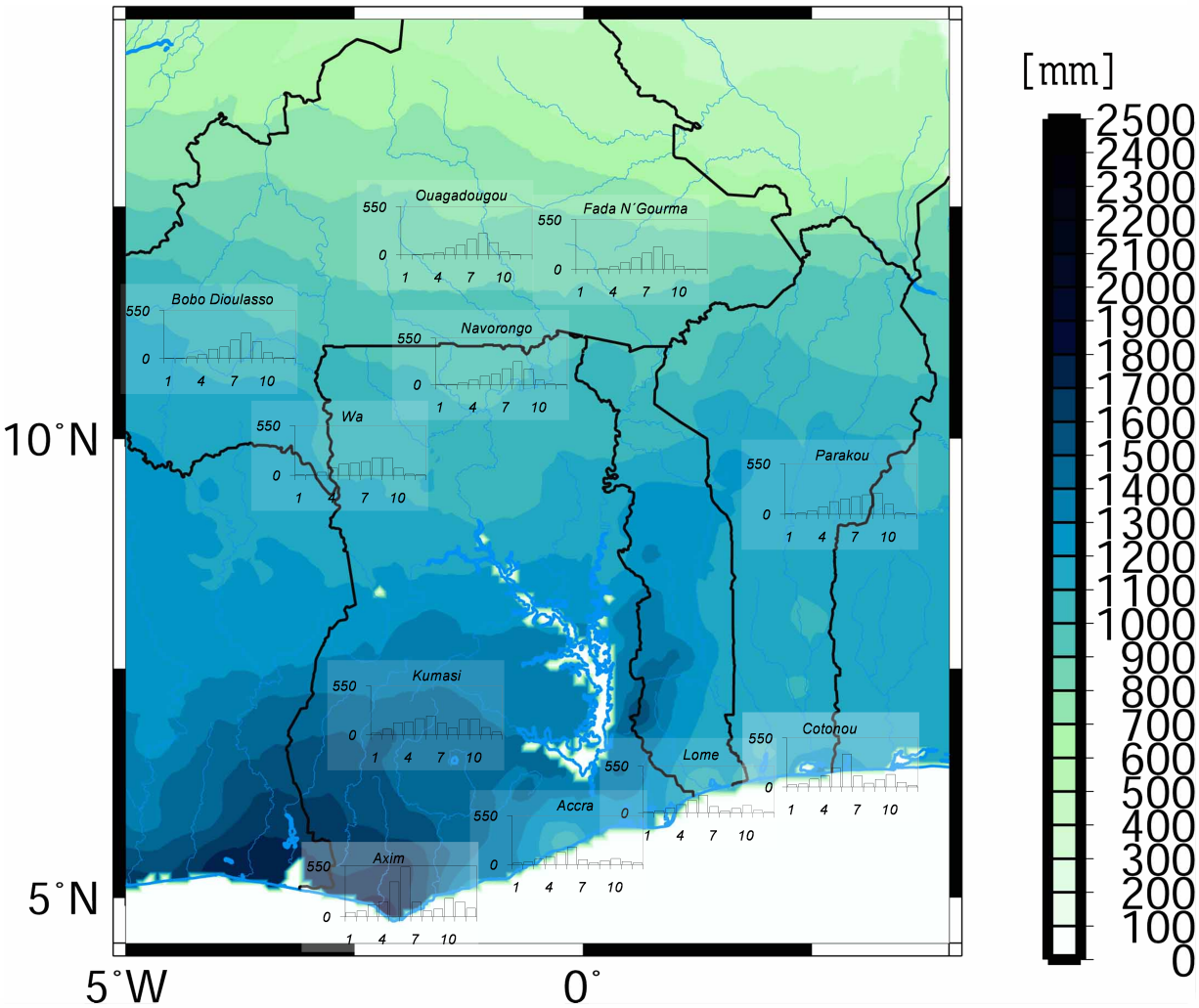

Figure 2.1: Mean annual precipitation [mm] in the Volta region (spatially interpolated station data)

This spatial distribution of annual precipitation[1] is illustrated in figure 2.1. Additionally, selected monthly station values demonstrate the annual cycle of precipitation with its unimodal characteristic of a single rainy season in the northern, sahelian part and the bimodal curve with its little dry season (July/August) separating the two peaks in rainfall during the rainy season along the coast.

Togo Gap and Dahomey Gap The afore mentioned region east of 1°W along the coast of Ghana and Togo and in general in southern Benin presents a striking contrast relative to surrounding areas due to low annual rainfall accumulation. In literature this region of reduced rainfall often is denoted as Togo Gap, meaning the dry sequence along the coast of Ghana and Togo. The part of the dry zone extending inland in Benin, Ghana and Togo is

[1]Spatially interpolated station data: the data consists of 95 stations' time series with a minimum length of 25 years. The spatial interpolation was done with a combination of inverse distance weighting (IDW) and multiple linear regression (MLR), weighting IDW with 60%. For the MLR, latitude, longitude, height, slope, curvature and aspect were considered

called Dahomey Gap or Ghana Dry Zone. The causes for these dry zones are summarized and discussed in detail in VOLLMERT et al. (2003) and are a good example of the complexity of the climate system within the region of interest.

For the coastal dry zone, thereafter, the dominating influence can be found in a divergence anomaly which induces subsidence. This anomaly is induced by differing averting of the coastal parallel monsoonal winds due to friction. Furthermore an up-welling of cold water along the coast intensifies the effect in stabilizing the lower troposphere. This upwelling is on one hand due to the Ekman drift, orthogonal to the coastal parallel winds. On the other hand it is reinforced by coastal Kelvin waves that transport the signal of an oceanic flow divergence with origin in the western Atlantic to the Gulf of Guinea.

For dry spells reaching further inland in Benin, three major influences are found. First, a velocity divergence can be found near the monsoon low of Lake Tschad. Moreover a lee effect is apparent in the northern region east of the Togo Mountains. Forced ascent of air masses on the western side of the mountains leads to high rainfall amounts there, leaving air masses with reduced amounts of precipitable water for the eastern side of the mountain range. A third reason lies in squall lines that originate from mountainous regions, with a maximum of generation in the Nigerian plateaus of Jos and Bauchi, that reach the Dahomey gap in a state of dissolution without a reinforcement, due to the flatness of the terrain.

Large Scale Dynamics As the general climate characteristics of a region, like the annual cycle of meteorological variables, and their spatial distribution are determined primarily by large scale dynamics, an overview of the most important features of West African climate dynamics will be given in the following.

On the global scale, as a consequence of the latitudinal dependence of solar insolation and the subsequent permanent thermal deficit in polar regions, the global circulation system is induced. Within this global circulation, the Hadley circulation, which is the mean meridional circulation in lower latitudes and the Walker circulation which is the mean zonal circulation along the meteorological equator are the dominating factors determining West African dynamics and its variability.

The Hadley cell is a thermally driven, direct circulation cell with a rising of warm, light air at the meteorological equator, and rapidly descending colder, heavier air in the subtropics, associated with a production of kinetic energy.

The *Inter Tropical Convergence Zone* (ITCZ) along the meteorological equator will in the following be denoted as the *Inter Tropical Discontinuity* (ITD), following HAYWARD and OGUNTOYINBO (1987). In the lower troposphere air masses from higher latitudes flow southwards. The discontinuity that is separating the subsident air masses of the Hadley circulation from these low level, southward moving cooler air masses is the trade inversion. Only within the range of the ITD, the trade inversion vanishes due to the intense lifting of air masses.

The upbranch of the Hadley circulation is adjacent to the northern edge of the monsoon circulation (VIZY and COOK, 2002) that controls moisture transport to the continent. The north-eastern, lower tropospheric trade winds floating from the subtropics equatorwards form the lower branch of the Hadley circulation (PEIXOTO and OORT, 1992).

In the subtropics, above the downwards directed branch of the Hadley cell, at around

200 hPa, we find the *Subtropical Jetstream* (STJ), which spans around the entire globe. Though the STJ affects large scale convection in the lower troposphere, for West Africa it plays a role of minor importance.

The main factors determining climate and its variability in West Africa are illustrated in figure 2.2 and described in the following.

Most flow characteristics in West Africa are connected with the ITD. The ITD separates humid maritime monsoon air masses from dry, continental air masses from the Sahara. Within an annual cycle the ITD moves northwards, up to 30°N in summer and southwards in winter as far down as to the (geographical) equator, triggered by the position of the sun.

As a consequence of the northward movement of the ITD the cross-equatorial moist cool monsoonal air masses from the Gulf of Guinea penetrate deep into the continent during the rainy season. In the dry season the dominating flow is the Harmattan, originating from the Sahara desert.

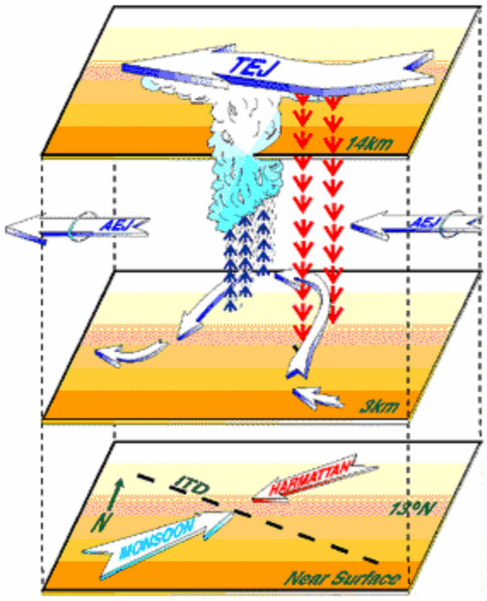

Schematic U–shaped AWD is shown at the middle of three levels in the atmosphere. Arrows indicate winds at different altitudes.
TEJ = Tropical Easterly Jet;
AEJ = African Easterly Jet;
ITD = Intertropical Discontinuity, where monsoon winds from the ocean meet dry Saharan harmattan winds.

Figure 2.2: Jetstreams, ITD and African Wave Disturbance (AWD) (www.giss.nasa.gov/research/briefs/druyan.01)

In addition, the *African Easterly Jet* (AEJ) that is found in 600-700 hPa, and the *Tropical Easterly Jet* (TEJ) in 200 hPa are related to the ITD. The formation of both of these jetstreams, depends on barotropic, as well as baroclinic instabilities in regions of high temperature and moisture gradients along the discontinuity. Cook (1999) stated that the horizontal soil moisture gradient is the major player in the formation of the AEJ. Due to the existence of these easterly jet streams over West Africa the circulation system is not explainable solely through the idealized Hadley circulation, but zonal contributions to the flow are also important (Vizy and Cook, 2002).

Strength and location of both, the AEJ, as well as the TEJ influence the climatic conditions of the region. Instabilities of the AEJ are responsible for the formation of *African Wave Disturbances* (AWD), or *African Easterly Waves* (AEW) (Burpee, 1972; Redelsperger et al., 2002). Most important for the generation of the kinetic energy of these waves is the horizontal shearing within the AEJ.

The waves in turn trigger the formation of squall lines and mesoscale convective complexes (Fink and Reiner, 2003). The greatest share of precipitation in West Africa is associated with either one of these convective systems (Hodges and Thorncroft, 1997), and so AEWs play a key role modulating convection and rainfall in West Africa. While

the development is triggered by AEWs, the enhancement of deep convection is related to an increase in low-level moisture, due to the strengthening of the monsoon flow (Duvel, 1990).

Squall Lines Squall lines are organized, long-lived convective systems whose generation is mainly dependent on daytime surface heating, topography, moisture supply by the monsoonal flow and large scale convergence (Rowell and Milford, 1993). Roux and Testud (1984) give a detailed description of pressure, temperature and humidity structure and the dynamics of squall lines and Weisman and Rotunno (2004) give a good overview over the theory. According to Redelsperger et al. (2002) squall lines are important in transporting heat, moisture and momentum due to the high degree of organization and the fast propagation. Therefore squall lines are in addition an important factor influencing the large scale state of the atmosphere.

West African Rainfall Variability One of the most striking characteristics of the West African rainfall regime is its high inter-annual, as well as inter-decadal variability. Significantly dry years differ from wet years by up to 50% in terms of precipitation amount.

A common notion is, that African rainfall variability is related to an anomalous excursion of the ITD (Kraus, 1977). Following Nicholson (2000) this can only be observed in some of the wet years, whereas no systematic anomalous southward displacement of the ITD is evident in dry years.

Observations suggest, that the inter-annual variability in West Africa can be partly explained by a connection of the Hadley, and the Walker circulation. In drought years a stronger Hadley circulation could be observed, whereas in wetter years a stronger Walker circulation was evident (Burpee, 1972). This can be linked to the observation that dry years were connected to a weaker TEJ and a stronger AEJ. In wet years the opposite was observed (Nicholson, 1980).Via Walker circulations and the Indian monsoon, the West African monsoon is also related to ENSO dynamics (Maynard et al., 2002).

A rainfall anomaly dipole fluctuation with a time-scale of less than 5 years (Rowell et al., 1995) was found from observation, with an anti-correlation of rainfall variability in the Sahel and the Guinea coast region in most cases. This dipole was first described by Klaus (1978). Bader (2005) identified the eastern tropical Atlantic and the Indian Ocean as areas driving rainfall anomaly patterns in West Africa. Accordingly for the Guinea Coast variability the influence of *Sea Surface Temperature* (SST) in the tropical Atlantic is dominating. Rainfall north of 10°N was found to be linked to Indian Ocean SST via large-scale atmospheric circulation. A detailed description of the dipole and rainfall variability in the West African Sahel can e.g. be found in Fontaine et al. (1995) or Nicholson and Grist (2001).

Various influences on the variability as well as on the persistence of rainfall regimes could be identified from the results of several investigations. Here Eltahir (1996) and Nicholson (2000) give a good overview on the dominant mechanisms. These range from an influence of SST variations in neighbouring oceans on the variability of rainfall (Lamb, 1978a,b; Druyan, 1991; Vizy and Cook, 2001, 2002) to an influence of bio-geophysical feedback mechanisms, for example through land-use change, on the persistence of a certain rainfall regime (Charney, 1975; Lare and Nicholson, 1994).

Vegetation dynamics plays a prime role in enhancing climate variability in the Sahel region (Wang and Eltahir, 2000). In addition, soil moisture-rainfall interactions are found to show a positive feedback and therefore can be responsible for the persistence of a rainfall anomaly (Walker and Rowntree, 1977; Zheng and Eltahir, 1997). Nevertheless a negative feedback loop was identified in case of soil moisture-rainfall interaction dependent on the scale of consideration (Jung, 2001; Kunstmann and Jung, 2003). In mesoscale meteorological simulations, Jung (2001) found a positive feedback, with an increase in precipitation following an increase in soil moisture when entire West Africa was simulated. For the Volta region (∼660000 km^2) an increase in rainfall could be observed, when the initial soil moisture content was reduced, due to an increase in convective activity in combination with sufficient moisture supply from the adjacent ocean. Kunstmann and Jung (2003) additionally observed a spatially highly heterogeneous response of rainfall with respect to changes in landuse. These examples demonstrate the sensitivity of the regional rainfall regime to land-surface conditions.

2.2 Hydrology of the Volta Basin

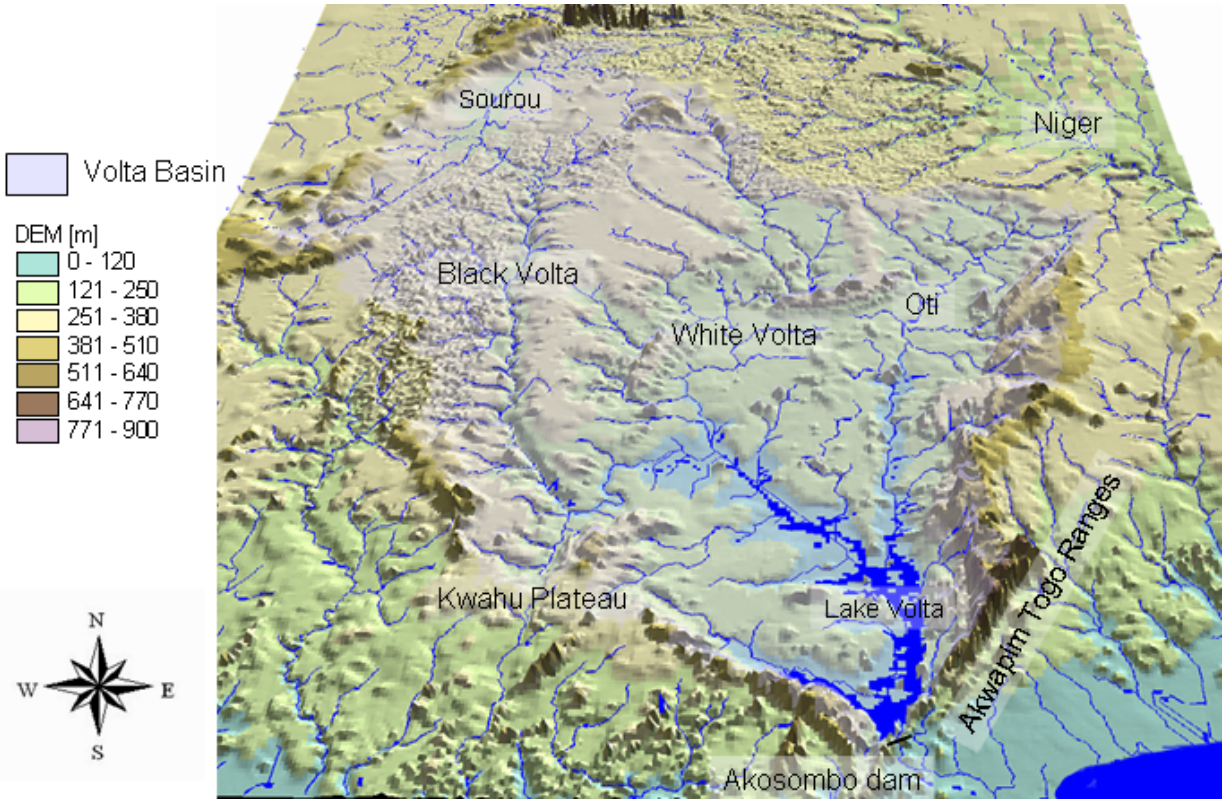

Figure 2.3: The Volta Basin: Geography

Discharge The terrain, which drains the Volta is of extreme flatness. All rivers of the basin drain into Lake Volta, one of the worlds' largest artificial lakes. From there, the Volta river flows to the sea, via regulated spillways. The dam is situated near Akosombo, in the

gorge where the river leaves a sandstone and shale basin of south-eastern Ghana and cuts across the Akwapim hills. Lake Volta has an approximate length of 400 km, a surface area of 8500 km^2 and, with a mean depth of 70 m reaches a capacity of 153 km^3 (Shahin, 2002). Mean annual controlled discharge downstream Akosombo dam is 38.2 km^3.

Runoff generation in the tropics is dominated by the Hortonian flow, that originates from infiltration excess overland. The Dunne's flow that is by contrast due to a saturation excess mechanism can be found in flood plains and valley bottoms (Peugeot et al., 1997). Due to the high intensity rainfall events, in combination with poor infiltration properties of the soil, Hortonian flow is favoured in the Volta Basin. In the valleys near rivers, and in areas with very shallow soil depth, the Dunne flow is the dominant runoff generation process (Ajayi, 2004).

The runoff coefficient, defined as

$$RC = \frac{Q}{P}100 \tag{2.1}$$

with river discharge Q and precipitation P, is relatively low in the Volta Basin. On average 9% of rainfall becomes river discharge. For the Black Volta catchment it is only 4.9%, for the White Volta its 7.1% and for the Oti 13.5% due to the steeper terrain in north-eastern Ghana and in Togo. The high nonlinearity of the rainfall-runoff response is demonstrated by Andreini et al. (2000). They estimate, that approximately 340 km^3 of rainfall have to occur, before a significant amount of runoff can be observed. Hence runoff response is also strongly dependent on the initial soil moisture content.

As a response to the high inter-annual variability in precipitation, runoff is even more variable in time. Where rainfall in the Volta Basin has a mean variations coefficient of 7%, for river discharge it is 57% (Andreini et al., 2000). This indicates the high sensitivity of runoff with respect to rainfall and implies that relatively small changes in annual precipitation can cause large changes in river flow (Obeng-Asiedu, 2004).

Observations of river runoff at the Volta river before the building of the dam have shown a high seasonal variability. Mean discharge in the driest month is approximately 240 times less, than mean peak flows (Andreini et al., 2000). In the Burkinabè part of the basin most of the rivers even run dry during the dry season, where the Mouhoun is the only permanent river. During the rainy season large areas of adjacent floodplains are subject to regular shallow flooding of less than 100 cm (van de Giesen, 2001)

One tributary of the Mohoun is to be mentioned separately, the Sourou. The Sourou, coming from Mali, joins the Mohoun where it turns its flow from a northward to a southward direction. The Sourou flows through a North-South trough, the so called Sourou depression (figure 5.3, section 5.2.1). The Sourou depression naturally regulates the runoff of the Mohoun. During the rainy season, when discharge of the Mohoun exceeds a certain level, water from the Mouhoun flows to the Sourou depression and is stored there. In low-flow times it takes up its normal flow and feeds the Mohoun. Therefore it helps to rout the flood wave, and retain lots of its sediment load (Shahin, 2002). In 1984 a regulation mechanism was installed to control the flow and to allow a storage of up to 0.25 km^3 of flood flow water and give some of the surplus water back to the Mohoun in the dry season (Bro, 2001). The Sourou is assumed to have been a tributary of the Belin, which flows to the Niger in the quartenary, where the Sourou was already fed by the floods of the Mohoun (Guillobez, 1993). Downstream of Sourou, at the gauge Boromo, the Mohoun

(Black Volta) is characterized by a very low runoff coefficient of less than 3% due to the depression and the flatness of the terrain (SHAHIN, 2002).

River Network As illustrated in figure 2.3, the main tributaries to Lake Volta in the South are the Black Volta (while in Burkina Faso it is called Mohoun), the White Volta (Nakanbé), and its main tributary the Red Volta (Nazinon), and the Oti (Pendjari) river in the East. They all originate from Burkina Faso. In the South-West the basin is bordered by the Kwahu plateau, which separates the Volta Basin from the rivers flowing directly to the Atlantic ocean in the West.

Land Cover Land cover in the Volta Basin is dominated by savannah type vegetation. From South to North a transition from guinea savannah, via shrub savannah to Sudan savannah occurs.

Several studies demonstrated the high influence of land cover type on runoff processes. CHEVALLIER and PLANCHON (1993), for example, investigated runoff processes in the small Booro-Borotou basin, in a savannah environment in Ivory Coast and detected a dominant influence of vegetation on the high variability of infiltration. For Benin, GIERTZ (2004) discussed similar results (see also section 3.4.2).

Soils The soils of Burkina Faso are predominantly of lateritic type. In the southern part of the basin, the soils are mainly lixisols. These are strongly weathered soils with predominantly kaolinite clays and high contents of iron, aluminium and titanium oxide. The aggregate stability at the surface is low and soils are prone to erosion if vegetation cover is removed (ADAMS et al., 1996).

The other main group of soils in the Volta Basin are the arenosols, mainly to be found in the northern, arid part of the basin. The basis is sand, coated with iron oxides, which gives the soil its specific reddish colour. These soils are characterized by high infiltration rates.

A study on soil properties by AGYARE (2004) at two sites in the Ghanaian Volta Basin revealed high discrepancies between subsoil and topsoil due to less soil disturbance in the subsoil. Saturated hydraulic conductivity (K_{sat}) turned out to be highly variable in space for both soil layers considered. Another study by GIERTZ (2004) supported these findings. In an investigation of soil characteristics of the Aguima catchment in Benin, she demonstrated, that Lixisols and Acrisols have a high variability of saturated hydraulic conductivity due to a strong influence of macro pore flux.

Geology The dominant geological systems of the basin are a Precambrian platform and a sedimentary layer, which is of minor importance for the basin as a whole, but covers a large area in the Ghanaian part.

The Ghanaian sedimentary layer, which underlies the Volta Basin, is known as the Voltaian formation. A detailed description of the geohydrology can be found in VAN DER SOMMEN and GEIRNAERT (1988), and, with a special emphasis on the ghanaian part of the basin, in AGYARE (2004).

Burkina Faso is dominated by crystalline and metamorphic rocks of the West African shield, formed primarily from Precambrian platform rocks, which are essentially imperme-

able. Fractures and channels, that enable the transmission and storage of groundwater only developed through tectonic movements (SHAHIN, 2002).

The basement and the overlying weathered zone form a two-layer aquifer that reaches from 25 m to 65 m below ground. The average depth of the decomposed zone in the Ghanaian part of the Precambrian platform is given as 40 m and aquifers are characterized through low transmissivities (7.5-30 m^2 d^{-1}) and low storativities (0.003-0.008).

A detailed geohydrological map of the Volta Basin was set up and analyzed by MARTIN and VAN DE GIESEN (2005).

Groundwater The groundwater aquifer system is characterized by two different aquifer types. One is of reservoir type, meaning a weathered mantle of high porosity, but low permeability. This type provides the main aquifer storage (ADAMS et al., 1996). The other type developed in fractured bedrock, has low porosity and high permeability.

It is generally assumed, that the aquifer systems in the basin are highly discontinuous with individual compartments in which isolated groundwater circulation occurs (AMISIGO, 2005).

Surface water and groundwater are regarded as separate resources with little or no interaction. Groundwater flow to rivers in the basin is regarded as insignificant (VAN DER SOMMEN and GEIRNAERT, 1988).

Groundwater recharge was found to be very heterogeneous spatially and it seems to derive largely from excess rainfall (VAN DER SOMMEN and GEIRNAERT, 1988). According to MARTIN and VAN DE GIESEN (2005), recharge is comparably low and no recharge at all is observed below an annual rainfall of 170 mm for sandstone aquifers and below 380 mm for weathered rock aquifers. Nevertheless, for the Mohoun catchment in Burkina Faso, another study assumes that groundwater recharge accounts for approximately 16% of annual rainfall (BRO, 2001). For the sub-catchment of the Nakanbé, the authors assume 13.4%.

2.3 Present Climate Trends in West Africa, the Volta Basin and Global Climate Change

Climate Trends in West Africa The event that led to an intensification of research in precipitation variability, and the detection of climate trends in West Africa, especially in the Sahel was the extremely dry period starting in the 1970s. Following LEBARBÉ and LEBEL (1997), SERVANT et al. (1998) or AMANI (2001), an overall tendency towards a decrease in rainfall has been observed since the discontinuity of the 1960s and 70s. According to NICHOLSON (1993) the 80s were the driest period of the 20th century in West Africa. A weak increase in rainfall occurred in the 90s, but never reaching values comparable to the 60s.

Nevertheless LEBEL et al. (2000) stated, that 'the available observations in West Africa are not sufficient to diagnose whether this drought is only a low probability event in a globally stable climate or the premise of a long lasting change'.

HULME et al. (2001) and NICHOLSON (2001) additionally investigated the spatial patterns of rainfall trends. HULME et al. (2001) found a decrease in precipitation exceeding 25% within the last century over some western and eastern parts of the Sahel, whereas

for most of equatorial Africa, they found a wetting of up to 10% within the 20th century. Similar results were obtained by NICHOLSON (2001), considering the 30yr mean of 1968-97 with respect to the 1931-1960 mean.

According to LEBARBÉ and LEBEL (1997) the drought period was characterized by a decrease in the number of rainfall events, and not by changes in the efficiency of rainfall events.

A decrease in discharge could be observed, associated with the lack of sahelian rainfall (AMANI et al., 2002).

Observations of temperature show a warming of the African continent for the last 100 years of about 0.5°C. The rates of warming, as well as the periods of most rapid warming (1910-1930 and from 1970 on) were similar to what can be observed globally (HOUGHTON et al., 2001).

Climate Trends in the Volta Basin Concentrating on the study area, a linear trend analysis was performed for the Volta Basin by NEUMANN et al. (2005). Within this analysis the linear trend of temperature, precipitation and discharge time series of Ghana and Burkina Faso were calculated. Furthermore, the trends were tested for significance, using the Mann-Kendall trend test (KENDALL, 1975) and the trend stability was calculated, using the reverse arrangement test. The study revealed strongly differing trend signals for the three variables considered.

- For temperature time series a clear trend of an increase over the last decades was concluded. The trend analysis predominantly showed positive significant trends (figure 2.4). Among the three variables tested, only temperature exhibited predominantly stable trends.

- For precipitation time series, both, negative and positive trends could be derived, but only a small number of trends were significant. Due to the fact, that almost all significant trends (figure 2.5) were negative, the conclusion of a weak trend towards a decrease in precipitation could be concluded.

- No linear relationship between the trend in precipitation and river discharge was found, revealing the non-linearity of the response of the discharge signal to the signal in precipitation. A reduction of discharge in the dry season and an increase in the wet season was concluded from the analysis, leaving the question of the reasons, and the weight of the anthropogenic influences (enhanced irrigation, building of dams etc.) to future studies.

Connection to Global Climate Change For 40 years time series of south-western Ghana, OPOKU-ANKOMAH and AMISIGO (1998) detected a statistically significant reduction of rainfall and runoff in the region, which they assumed to be linked to climate change.

Nevertheless it is difficult to connect small precipitation change signals to global climate change due to the fact, that the variability in West African rainfall is a highly nonlinear problem, that is, in first instance connected to the variability of the SST in adjacent oceans, and additionally influenced by land surface-atmosphere feedback mechanisms (compare section 2.1).

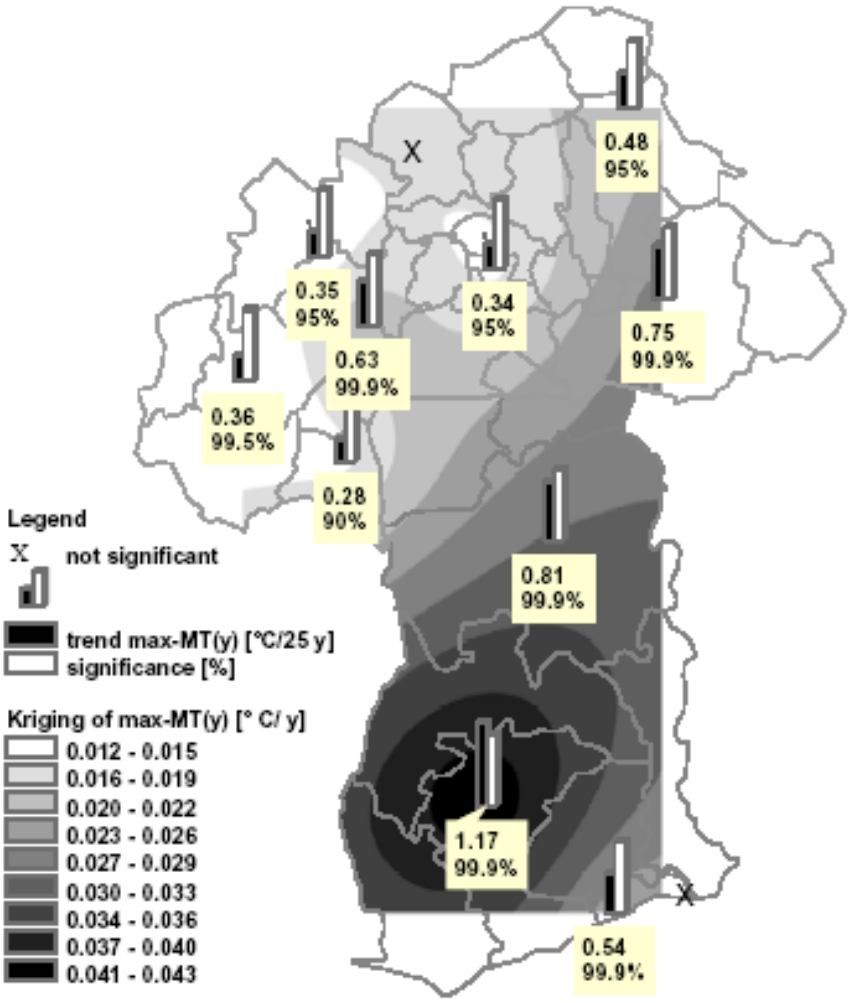

Figure 2.4: Trend in temperature [°C] and level of significance [%] for several stations, and kriged spatial distribution of the trend

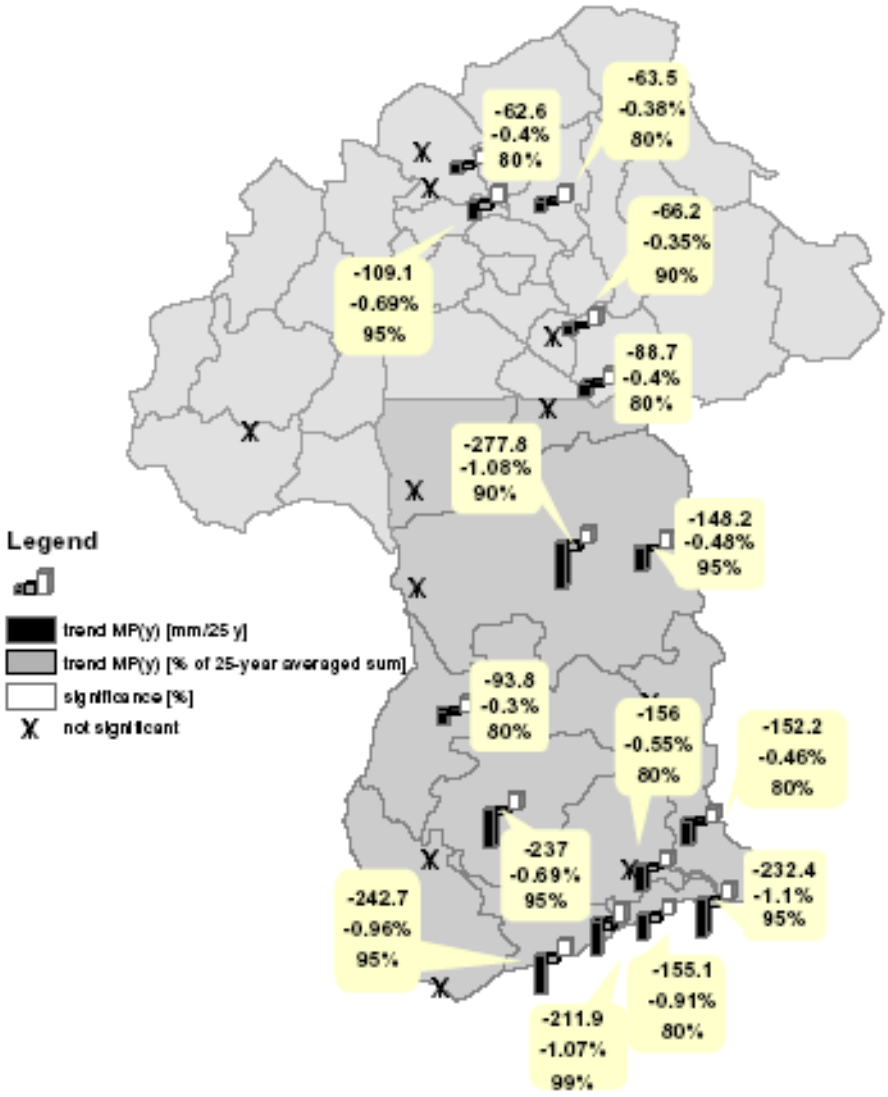

Figure 2.5: Absolute [mm] and relative trends [%] in annual precipitation, with level of significance [%] for several stations

How and to what extent rainfall is affected by a global climate change impacted SST is not answered simply.

Considering the Clausius-Clapeyron equation (e.g. PEIXOTO and OORT (1992)) leads to the conclusion, that in general, with globally rising temperatures, an increase in precipitation is expected, due to the fact, that warmer air masses can contain more moisture than colder ones. But HULME et al. (2001) already stated that no simple correlation between temperature and rainfall could be observed for West Africa. The Clausius-Clapeyron model does not take into account the strong influence of the dynamics of the atmosphere on the local stamping of a precipitation regime.

For West Africa, the complex monsoon dynamics (section 2.1) is of major importance for rainfall amounts. But since this dynamics is not stable and neither is it linearly linked to the influences of a possible global climate change, the question of how West African precipitation might change with global climate change can not be answered easily.

PAETH and HENSE (2004) for example state, that a warming of the Atlantic Ocean due to radiative forcing can lead to an increase in precipitation as a consequence of an enhancement of latent heat fluxes to the monsoonal flow. MAYNARD et al. (2002) additionally observed an enhancement of the West African monsoon circulation due to global climate change in climate simulations. PAETH et al. (2005) did not only find a strengthening of the monsoonal flow, when the tropical Atlantic SST was increased in regional climate simulations, but also an enhancement of the north-easterly dry Harmattan, leading to higher (lower) precipitation amounts in the Guinea Coast (Sahel) region, confirming the known dipole structure of precipitation variability (section 2.1).

Another fact to consider is, that additional influences, like changes in land use also influence West African monsoon dynamics and might thereafter serve as a counter actor to the enhancement of the hydrological cycle due to higher temperatures. ZHENG and ELTAHIR (1997) even claim a possible collapse of the monsoon system as a consequence of deforestation in coastal regions of West Africa.

Consequently the trend signal in precipitation that can be observed so far can not be easily ascribed to a single cause.

Trend in the Onset of the Rainy Season For a detection of trends in climate variables of West Africa, the determination of the trend in the onset of the rainy season is important, because the onset, as well as the length of the rainy season determines the success of agricultural activities and are therefore of prime importance for the livelihood of the people.

LEBARBÉ et al. (2002) divided the onset of the rainy season into two different dynamical regimes. The first onset is connected to the onset of the rains starting in the coastal regions of West Africa around February, and propagating regularly north, up to 13°N in May. SULTAN and JANICOT (2003) defined this as the pre-onset of the monsoon. The second onset is the onset of rains in the Sahel region and occurs simultaneously between 9° and 13°N. This onset is connected to a shift in the position of the ITD from a quasi-stationary location at 5°N in May/June to another quasi-stationary position at 10°N in July/August (SULTAN and JANICOT, 2000). This northward shift of the ITD is connected to westward travelling cyclonic circulation over the western Sahel. GU and ADLER (2004) and SULTAN and JANICOT (2000) give a complex explanation of this shift in the ITD, considering SST, thermal forcing and an interaction of the different large-scale dynamic features (AEJ, TEJ,

AEW, low-level westerly flow and moist convection).

Following LEBEL and VISCHEL (2005), no significant change in the date of this second or main onset could be observed, as it always can be observed in the last week of June. LEBARBÉ et al. (2002) found the length of the rainy season in the Sahel unchanged, but a shortening of the second rainfall period within the bimodal rainy season along the coast of around 10 days, accompanied by an earlier start, as well as an earlier end of the rain period.

An analysis of the onset of the rainy season is also performed within the GLOWA-Volta project (LAUX et al., 2005). The definition of the onset date closely follows STERN et al. (1981), with some variations by DODD and JOLLIFFE (2001), that were especially adapted to the needs in Burkina Faso. Thereafter, the following three criteria determine the onset of the rainy season:

1. A period of 6 consecutive days occurs in which at least 25 mm of rainfall occurs
2. The start day and at least two other days in the period are wet (at least 0.1 mm rainfall recorded
3. No dry period of 10 or more consecutive days occurs in the following 40 days

Following this approach a preliminary trend analysis of the onset dates shows a delay of the onset of the rainy season between 5 and 28 days within 30 years. The minor trend signal is found along the coast, whereas the strongest signal is observed in the Sahelian parts of Burkina Faso.

Chapter 3

Climate and Hydrology Modelling: Theory and Application in West Africa

The basic concepts of global climate modelling, various downscaling methods and hydrological modelling are described in this chapter. In addition examples of coupled modelling studies and regional climate, as well as hydrological modelling attempts in West Africa are discussed.

3.1 Emission Scenarios

Emission scenarios are a central component of any assessment of climate change, as certain assumptions have to be made to investigate the impact of increasing anthropogenic *Greenhouse Gas* (GHG) emissions on future climate through radiative forcing.

To obtain future GHG concentrations for the use in global climate simulations, certain assumptions on factors influencing the emissions of greenhouse gases, have to be made. The main determinants for future emissions are the technical, as well as the socio-economic, and demographic development on regional, and global scale.

Due to the uncertainties underlying these assumptions, the emission scenarios are neither predictions nor forecasts, they are just images of the future, or alternative futures (Houghton et al., 1995).

In 1992, the IPCC developed the six IS92 scenarios.

In the evaluation of the scenarios in 1995 the following weaknesses associated with the IS92 scenarios were found: A limited range of carbon emissions per unit energy, the absence of scenarios including a closure in the income gap between developed and developing countries, and the lack of influence of recent and possible future legislation concerning sulphur emissions, resulting in a too rapid growth of the atmospheric SO_2 concentration (Houghton et al., 1995).

From 1996 on, a revision of the IS92 scenarios was done, which resulted in 40 new so called SRES scenarios (Nakicenovic, 2000). A higher differentiation of the various developments was included. These scenarios are grouped in the four main groups A1, A2, B2 and B2.

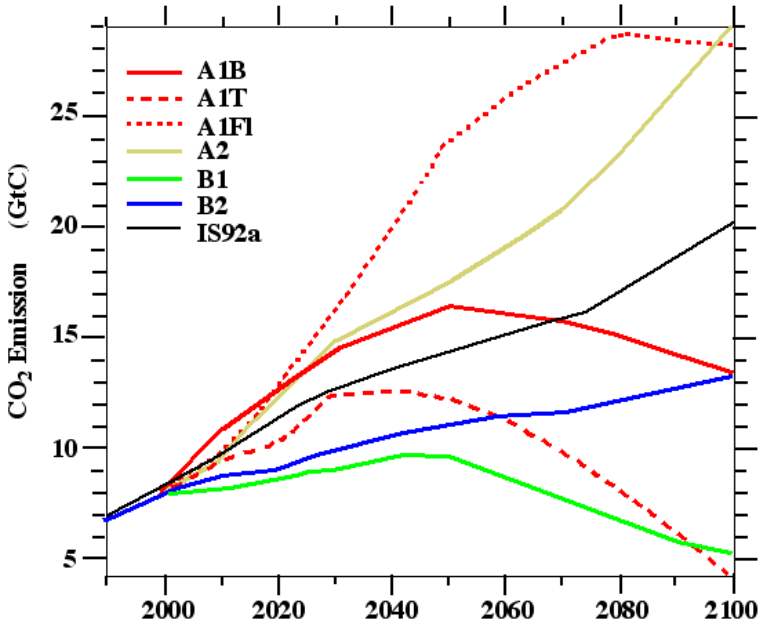

Figure 3.1: CO_2 emissions of IS92a and the newer SRES emission scenarios (*www.ipcc.ch/present/graphics.htm*)

Within this study, only the IS92a ('business as usual') scenario was available. It lies in a central position for CO_2 (figure 3.1) and NO_2 concentrations with respect to the newer SRES scenarios. For methane it is in an upper range. The assumption behind the IS92a scenario is an increase in CO_2 emissions of 1% per year, from 1990 on.

3.2 Global Climate Modelling

One approach for an investigation of the influence of increasing greenhouse gas concentrations in the atmosphere to global climate is numerical modelling with *Global Circulation Models* (GCMs). These GCMs were originally developed for weather forecasting and adapted for the use as global climate models. Where the first models only consisted of an atmospheric part (and are therefore also called AGCMs), the newer models are mostly AOGCMs (*Atmosphere Ocean General Circulation Models*), where the AGCM is coupled to an *Ocean General Circulation Model* (OGCM).

Among input data required by these GCMs are the emissions, derived from the scenarios described in the previous section.

Global GCM Performance Most GCMs manage to represent large scale patterns of climate variables very well. Broad response to the Pacific ocean forcing of ENSO (El Nino - Southern Oscillation) and to SSTs in adjacent basins, like Atlantic and Indian ocean can be detected in GCM simulations (Washington et al., 2004). GCM ensemble simulations were performed within a variety of studies to asses the uncertainty of the global climate runs and test the reliability of the models. A study by Govindan et al. (2002) comparing 7

GCMs including ECHAM4/OPYC showed that these AOGCMs in general underestimated the long-range persistence of the atmosphere and overestimated the trends. Therefore the conclusion was drawn, that the global warming trend might also be overestimated by the models. Nevertheless, global climate models proved their ability to represent the most important large-scale dynamics and teleconnections.

GCM Performance for the African Continent A model inter-comparison of different GCMs, with a focus on the African continent, was performed in the study of Hulme et al. (2001). Their multiple model simulations showed small signal to noise ratios, and therefore high uncertainties, for precipitation scenarios. In addition different signs of precipitation change were found in different model simulations. The ensemble median revealed a drying for the Sahel region. An analysis of skill for ECHAM4, with prescribed SST for the tropics was performed by Moron et al. (1998). Their study confirmed that also ECHAM4 was able to capture most important tropical rainfall teleconnections with SST. For West Africa they detected a dependence of skill on ENSO dynamics in northern hemispheric winter, but a stronger influence of tropical Atlantic SST in the summer months. An exaggerated northward movement of the ITD in boreal summer and an underestimation of inter-annual rainfall variability, due to an insufficient representation of feedback mechanisms with the local vegetation cover and albedo was detected by Schnitzler et al. (2001). Maynard et al. (2002) pointed out, that all GCMs that were compared within the WAMP (West African Monsoon Project) have a large wet bias over West Africa. Giorgi and Francisco (2000) compared the performance of different AOGCMs for selected regions, among others West Africa. For the ECHAM4/OPYC simulations they found an overestimation of temperature by 0.5°C in the months of June, July and August (JJA) and 1°C in the months of December, January and February (DJF) over West Africa for the years 1961-1990. Rainfall estimates for the same period had a bias of 140% in DJF, and up to 25% in JJA. Within an analysis of ECHAM4 runs with prescribed SST Paeth and Friederichs (2004) found a generally good representation of West African climate, but an underestimation of inter-annual variability over the sub-Saharan region and a displacement of the ITD too far to the North in the rainy season. These weaknesses are most likely due to the insufficient representation of land cover - atmosphere feedback mechanisms (Schnitzler et al., 2001).

Nevertheless several weaknesses of global models were found, like an inaccurate temporal positioning of the onset of rains in the Sahel in some models and a reversed cross-Atlantic Ocean temperature gradient in coupled AOGCM simulations. Still some additional progress needs to be made in the representation of coupled land surface - atmosphere feedbacks and Saharan dust, which is not included in most models.

Global Climate Change Projections Global mean annual *Surface Air Temperature* (SAT) changes are summarized for the scenario IS92a of the present study and for the scenarios recently used most frequently, A2 and B2 in table 3.1, following the IPCC report of 2001 (Cubasch et al., 2001).

In general, global model projections show a stratospheric cooling, and a tropospheric warming, which is larger over land, than over the ocean. Global mean evaporation, water vapour, and precipitation increase. In the subtropics, precipitation decreases, whereas in

Table 3.1: Mean changes in global surface air temperature for 2021-2050 with respect to 1961-1990, ensemble means and inter-simulation ranges [°C]

	Mean [°C]	Range [°C]
IS92a	+1.6	1.0-2.1
A2	+3	1.3-4.5
B2	+2.2	0.9-3.4

the tropics and in midlatitudes an increase occurs. Inter-model differences were found to be as large as inter-scenario differences. The signal to noise ratio of temperature is larger, than that of precipitation, indicating a higher reliability of the temperature change signal.

For ECHAM4/OPYC climate scenarios an enhancement of ENSO activities was found (Ashrit et al., 2001; Hu et al., 2001), due to an enhancement of the Walker circulation within the considered time period (2040-2099).

African Climate Change Projections For the IS92a scenario simulation, Giorgi and Francisco (2000) found an increase in SAT of 4.3°C in DJF and 3.5°C in JJA over West Africa. Rainfall was simulated to increase by 5% for DJF and by 10% for JJA. Results from climate scenario simulations with the newer SRES scenarios A2 and B2 (Nakicenovic, 2000) also show a temperature increase in West Africa greater than the global mean, and increases in rainfall, smaller than the inter-annual and inter-decadal variability. Kamga (2000) compared different global climate model outputs for the region of Cameroon and neighbouring areas. They found no significant changes in mean rainfall for the 2040-2070 period, neither for the HadCM2, nor for the ECHAM4 model. Temperature change was found to be significant for both, with an increase of 2.5-3°C within the region. Hulme et al. (2001) demonstrated a sophisticated analysis of African climate change based on observations on one hand, and regional analysis of GCM simulations on the other hand, but without any regional downscaling. They analyzed 7 GCMs with different scenario runs (the SRES scenarios A1, A2, B1 and B2) for the climate changes within different African regions. They found that the inter-model range of rainfall change was with few exceptions larger than the magnitude of the median model response. For example for the Sahel region, inter-model ranges were as large as 100%. Where in general, no confidence about rainfall change neither in magnitude, nor in direction could be delineated, a continent wide warming of between 2°C and 6°C was found in the different models and scenarios.

In general, the different studies on African climate change, agree with respect to the increase in temperature, but yield diverging results for precipitation. What they nevertheless do agree in is the fact that precipitation changes are mostly to be found within the range of climate variability.

3.3 Regional Climate Modelling

How good any global circulation model might be, for the sake of computation time the resolution of a GCM must always be relatively coarse. Within the resolution of most GCMs, that are used nowadays, it is not possible to achieve an explicit representation of mesoscale forcings, like land-use, orography and land-sea contrasts.

3.3.1 Regional Scale Forcing in the Volta Basin

In the region of the Volta Basin the following regional scale influences have to be considered:

Topographic Influences The mountain range along the border between Togo and Ghana in particular has to be mentioned as important orographic characteristic in the Volta region. Due to a higher resolved topography, lee effects, and an orographic enhancement of convection are accounted for in more detail in the smaller scale simulations.

Land cover A high resolution of land cover is also essential for small scale dynamics, as land-atmosphere interactions are not only a large-scale phenomenon.

Convective Precipitation Although convection is triggered by large scale forcing (compare section 2.1), small and mesoscale convective systems are observed in West Africa. This means, that convective processes happen predominantly below grid scale in coarser resolved simulations. In coarsely resolved simulations, convective parameterization schemes, although required, provide only a limited representation of small scale rainfall processes, and are one of the largest sources of meteorological modelling uncertainty.

Land-Sea Interaction Furthermore, land-sea interactions are of major importance for small scale climate conditions in the Volta Basin. If we consider phenomena, like the Togo-gap (section 2.1), that are strongly dependent on small scale SST fluctuation, like the up-welling of cold water along the coast, these can not be represented unless the regional climate model is coupled to a mesoscale ocean model.

These mesoscale, and even smaller scale forcings have to be represented properly for a sophisticated hydrological impact analysis with a high resolution, distributed hydrological model.

3.3.2 Downscaling Methods

Obtaining regional information directly from a highly resolved AOGCM or a global model with variable resolution would be the optimal way to get high resolution model output for physical consistency, but these methods are limited by computational power and cpu time demand. Another possibility is the downscaling of GCM output data, where two approaches can be distinguished: Dynamical and statistical downscaling.

Dynamical Downscaling Dynamical downscaling means the performance of a Limited Area Model (LAM) (e.g. a Regional Climate Model (RCM)). This includes the numerical solution of the whole set of atmospheric equations of motion, and the balance equations of energy, and momentum. Several sub-gridscale physical processes are parameterized using physically based approaches. Initial conditions, as well as lower and lateral boundary conditions are derived from GCM output fields. This indicates the dependence of the LAM results on the GCM output fields.

The first attempts at long-term regional climate simulations were performed by DICKINSON et al. (1989), GIORGI (1990), and GIORGI and MEARNS (1999). Recently the development in regional climate modeling is directed towards a coupling of other climate relevant processes and models to RCMs, like regional ocean models, hydrological models, and biosphere models.

Statistical Downscaling Another possibility for the regionalization of global climate change scenarios is offered by statistical downscaling.

Statistical downscaling encompasses a variety of statistical methods, that are applied to derive small scale meteorological fields from GCM simulations output. Basically regional information is derived by determining a statistical model, which relates large-scale climate variables to regional and local variables (GIORGI et al., 2001). Different methods of statistical downscaling include weather generators, weather typing, for example through the classification of circulation patterns (STEHLÍK and BÀRDOSSY, 2002) and transfer functions.

The transfer function approach utilizes empirically determined transfer functions that relate variables of regional or local interest to atmospheric-model simulated large-scale variables. A variety of methods can be incorporated to specify these transfer functions, like linear and nonlinear regression, Artificial Neural Networks, Principal Component Analysis (PCA), Canonical Correlation Analysis (CCA), Empirical Orthogonal Functions (EOF), Singular Value Decomposition (SVD), Non-homogenous hidden Markov models, Expanded Downscaling (EDS) and etc. (LEAVESLEY et al., 2005).

Statistical versus Dynamical Downscaling Undoubtedly a more physical representation of the effects of e.g. orographic precipitation is achieved by dynamical downscaling. MACHENHAUER et al. (1996) showed, that spatial patterns of downscaled RCM simulations had better agreement with observations, than the driving GCM simulation, due to a better representation of high-resolution forcings.

Nevertheless, in regions, where orographic contrasts are not striking, uncertainties that lie in physics parameterizations, and their sensitivity to grid-spacing might overwhelm any benefit of a higher resolution (DUFFY et al., 2003; NOBRE et al., 2001).

A serious limitation to predictability in dynamical downscaling approaches lies in the lateral boundary conditions. The numerical techniques used for interfacing the grids of the RCM and the GCM generate errors that propagate onto the RCM grid (WARNER et al., 1997). In addition, negative effects can be introduced from the different solution at the RCM lateral boundary, and within the model domain, due to different physics and/or resolutions of RCM and GCM. Strong forcing at the lateral boundary can also have a negative effect on the internal model solution. Another disadvantage of the dynamical downscaling is the high demand for computer power. Particularly in West Africa, this often is a limiting factor to the performance of sophisticated highly resolved, long term model runs for local institutes.

Therefore, in less technically developed countries, statistical downscaling has an obvious advantage. One example in this context is the Canada-Nigeria Climate Change Capacity Development Project (CN-CCCDP) (*www.nest-interactive.org*). Nevertheless, statistical downscaling demands a higher observational data density to provide more comprehensive statistical downscaling functions. The scarcity of data is another problem that scientists in

development countries often face.

An advantage of dynamical downscaling lies in the higher transferability between differing climate states, due to their physical realism (Hay et al., 2002). In addition, with dynamically downscaled GCM scenarios regional feedback mechanisms are accounted for.

A disadvantage of statistical downscaling therefore lies in the assumption, that statistical relationships developed for present-day climate also hold under different forcing conditions of possible future climates. However, statistical downscaling can help to eliminate systematic errors in global climate simulations, where dynamical downscaling is always affected by the errors in the global model.

If a downscaling is required for mean climate conditions, comparable to present-day observed climate, or in the case of a significant systematic bias within the GCM data, a statistical downscaling may be sufficient.

If the purpose of the downscaling is a derivation of regional climate for changed forcing conditions, and in data sparse regions, dynamical downscaling has to be favoured.

If the resolution of regional climate models is not sufficiently high for an impact analysis, or is subject to systematic modelling errors in high resolution, a combined dynamical-statistical downscaling approach might be feasible. This means, that the GCM output is in a first step downscaled dynamically and then, an additional statistical downscaling, or bias correction is applied.

Downscaling in this Study Within the study area, only a small number of longer time series of the different meteorological variables that are needed as input by the hydrological model were available. While in the case of rainfall, there were almost 100 stations, for temperature there were only 25 longer time series. The other necessary input variables (global radiation or sunshine duration, wind velocity and relative humidity) were extremely rare. Therefore no statistical downscaling could be performed, and a dynamical downscaling approach was chosen.

3.3.3 Regional Climate Modelling in West Africa

Few regional downscaling studies have been performed for West Africa so far. Most climate projections for West Africa were performed either by considering GCM output directly (compare section 3.2) or with statistical downscaling approaches.

A statistical downscaling approach was utilized by Penlap et al. (2003) for Cameroon. The authors analyzed the little rainy season of Cameroon for the global climate change scenario IS92a. Downscaling was performed by Self-Organizing Maps (SOFM), a neural networks method that incorporated the application of PCA and CCA to determine a statistical downscaling model. They investigated the periods 1951-1990 and 2011-2050 for CO_2-only forcing, as well as the years 2010-2049 for CO_2+SO_4 forcing. The results showed no significant change signal with respect to GCM and downscaling uncertainty.

Maynard et al. (2002) performed global climate simulations with the ARPEGE climate model for an investigation of the underlying mechanisms behind West African monsoon variability in the model. They concluded that a better representation of topography and orography, and therefore a downscaling may be needed for a more detailed analysis of the African monsoon.

Recently, a regional downscaling approach was undertaken by PAETH et al. (2005) , testing the performance of the regional climate model REMO for West Africa in a resolution of 0.5°, but without an application for climate change.

So far, no sophisticated, high resolved dynamical downscaling approaches were performed for West Africa to address the question of future climate change.

3.4 Hydrological Modelling

3.4.1 Approaches

Within the field of hydrological modelling a variety of concepts exist. First, **deterministic models** have to be distinguished from **stochastic/statistical models**.

Statistical models are based mainly on a description of observational variables and do not take cause-effect connections into consideration (BÁRDOSSY, 2003). In contrast, deterministic models do not include randomness, but are based on more or less complex physical laws and relationships. Also mixed **statistic-deterministic models** exist, because in many cases causal influences on the hydrological system can only be described via statistics, whereas the behaviour of the hydrological system can be described physically.

The structure of the deterministic models is a connection of cause and effect on the basis of either physical laws (**physically based models**), or based on an analysis of short time series (**empirical models**). Black box models are based mainly on simple empirical equations, determined e.g. by regressions or neural networks. In contrast, physically based models are characterized by a high degree of process understanding, as the hydrological processes are described through basic physical equations. In addition, these models are not limited to simple rainfall-runoff process modelling, but also simulate all most important processes within the hydrological cycle (e.g. evaporation, infiltration, interflow, and runoff). Furthermore, **conceptual models** that combine approaches of physically based models with empirical concepts are in use.

Deterministic models can furthermore be divided into **distributed models**, and **lumped models**. Distributed models work with parameters and variables that are functions of space dimensions. This can be achieved via a simulation of different subcatchments or through the calculation of the hydrological variables on a grid. Lumped models simply consider the catchment as a single unit. Stochastic models are spatially distinguished as **space-correlated** or **space-independent**, dependent on whether the random variables at different locations influence each other, or not (CHOW et al., 1988).

Empirical versus Physically Based Models Problems may be encountered in attempting to transfer empirical models to other subcatchments, or different climate and environmental conditions, as the model parameters are subcatchment, and climate specific. Therefore, these models are not suitable to analyze climate or land-use change scenarios.

This is where the advantage of physically based distributed models is found. A disadvantage of these models is the high parameter need that demands for a high degree of knowledge on soil physics, geohydrology and vegetation dynamics of the catchment. This leads to an increasing uncertainty, in case of sparse data.

For a determination of runoff processes often simpler models yield better results in data sparse regions. Furthermore it stays questionable, to what degree physically based model parameters, that are originally valid for equations of small scale physics of homogenous systems really represent the processes of heterogeneous grid cells and whether these processes can be described by the same set of equations at all. BEVEN (1989) discussed the conceptual nature of physically based models and concluded that generally distributed physically based models are essentially lumped conceptual models.

If the aim is a consideration of simple rainfall-runoff relationships, the use of an empirical model might be sufficient, and especially to be favoured in data sparse regions.

If the aim is a climate change impact study that demands for a high degree of transferability of the model, or an analysis of discharge relevant processes, a physically based model is to be preferred.

Hydrological Model Choice for this Study For the present study, the demand to the hydrological model was a high degree of transferability. First transferability between different subcatchments was necessary, because not for all subcatchments data availability was sufficient for calibration. Even more important was the transferability to different climatic conditions, because an investigation of the transference of a climate change signal from atmosphere to hydrosphere was the main task. Also a high degree of physics in the model was demanded for, because the analysis aimed at physically based process understanding, to gain some insight into the processes of importance for runoff generation and the hydrological cycle. Consequently, despite the high degree of parameter uncertainty due to low data availability, the use of a physically based model was essential.

3.4.2 Hydrological Modelling in West Africa

As mentioned before, the use of most hydrological models in the tropics is limited by the fact, that they were mainly developed for temperate conditions and are not easily transferable (KLEMES, 1993). This is especially true for simple lumped empirical or conceptual models due to their lack of physics representation.

Another limiting factor for reliable hydrological simulations in the tropics is insufficient data availability. Therefore, most hydrological analysis in the tropics are based on a large-scale description of the hydrological cycle, or concentrate on the atmospheric part of the hydrological cycle, just accounting for soil moisture and vegetation - atmosphere feedback mechanisms, not considering runoff processes in detail. Especially with physically based models with their high degree of parameter need, only few studies were performed so far.

To assure the transferability of the hydrological model to different climatic conditions, an explicit, physically based treatment of evapotranspiration modelling is demanded for. This was already discussed by BERGSTROEM and FORSMAN (1973) and PATUREL et al. (2003) mentioned a precise evapotranspiration simulation as especially important for West African catchments.

From a comparison of the distributed hydrological model TOPLATS, and a conceptual lumped model for the Ouémé catchment in Benin, BORMANN and DIEKKRÜGER (2003) found a good prediction of discharge with the simple model, but point out, that environmental change scenario analysis requires the application of distributed models to get a

detailed description of land cover change.

Giertz (2004) demonstrated a successful application and comparison of the physically based, distributed model TOPLATS, the physically based one-dimensional model SIMULAT and the conceptual, lumped model UHP to the Aguima catchment in Benin. The aim of this study was an investigation of runoff processes with a combined observational and multi-scale modelling approach. The analysis revealed a good performance of the models UHP and SIMULAT-H, but no sufficient results could be derived from TOPLATS simulations, due to an overestimation of saturated overland flow.

Bormann and Diekkrüger (2004) demonstrated the performance of the UHP model to the Térou catchment in Benin. They analysed the uncertainty, based on Monte-Carlo approach, using the Latin Hypercube sampling scheme, and found a significant impact of model parameters and spatial resolution of the input data on model performance.

Within the named studies no physically based approaches were found to be dealing with an investigation of climate change impact studies.

3.5 Coupled Climate-Hydrology Modelling for Impact Analysis

Since global and regional climate models increasingly simulate reliable scenario outputs, the demand to use these for an impact analysis in related research fields, like hydrology, but also in biology, agronomy, chemistry and even economy has grown in recent years.

The majority of the model coupling is still done one-way, feeding the respective model with the output of regional climate simulations. But also sophisticated two-way coupling approaches exist, like the coupling of climate and chemistry with the regional climate-chemistry model MCCM by Forkel and Knoche (2005).

Some studies were performed, that directly use global climate model output for an impact analysis on land surface hydrology. This is subsequently restricted to a coarsely resolved analysis of hydrology, and often applied for global or continental scale investigations of the hydrological cycle.

An analysis of the hydrological sensitivity to climate change for nine large, continental river basins (none of them in Africa), using the statistically downscaled data of four GCMs was performed by Nijssen et al. (2001). They found a decrease of annual discharge in most basins, despite a precipitation increase, but a varying seasonal runoff behaviour between catchments in higher and lower latitudes.

Chiew et al. (1995) demonstrated an impact assessment approach for Australia. They were using temperature and precipitation change information derived from different GCMs, to manipulate the input for a conceptual rainfall-runoff model, to estimate climate change impact on hydrology for the entire continent, divided into 28 catchments.

Another example of statistically downscaled impact analysis was performed by Salathé (2005) for the simulations of stream-flow of the Yakima River in the USA. They derived the global climate change signal from three different GCMs and two different scenarios (A2 and B2). They found a clearly good and sufficient performance using input from the global circulation model ECHAM4 with a simple statistical downscaling method.

For a mid-latitudinal environment, the Ammer catchment in Germany, a dynamical

downscaling, combined with a bias correction method yielded reasonable results for the models' sensitivity to global climate change (KUNSTMANN et al., 2004). Another example for a dynamical downscaling approach and coupled hydrological simulations with the aim of analyzing the impact of global climate change is a process study for the Rhine basin by KLEINN (2002). This study also included a comparison of the dynamically downscaled precipitation fields to the ones derived by two different methods of statistical downscaling. Both statistical downscaling methods did not provide satisfactory results, as precipitation amounts were underestimated by over 45%.

HAY et al. (2002) performed an analysis of using regional climate model output of the RegCM model in a 52 km resolution as input for hydrological simulations. They found, that a statistical bias correction of the regionally downscaled data had to be performed to achieve reasonable results, due to the still relatively coarse resolution of the regional model.

Where for West Africa, in general, the focus of climate change impact analysis in hydrology lies in an assessment of endangered water availability, for European and other mid-latitudinal regions, impacts on extreme events, like floods, or impacts on hydropower production are more important.

Studies of BERGSTROEM and FORSMAN (1973) and SCHÄFLI (2005) both demonstrate the influence of a regionally changing climate to hydropower production. They both follow a statistical-dynamical downscaling approach, using the information derived from regional climate simulations for a perturbation of the meteorological time series that serve as input to the hydrological model.

A two-way coupling approach of the operational variable resolution GCM ARPEGE of Météo-France to a distributed hydrological model MODCOU is described by OTTLÉ et al. (2001). Off line from meteorological modelling, the ARPEGE land surface model, coupled to the distributed, hydrological model MODCOU (CISRE) was applied for climate change studies for the Rhone basin, with a simple approach of adding monthly anomalies of ARPEGE GCM climate change scenarios to observed meteorology.

For southern Africa ARNELL et al. (2003) performed regional climate simulations and hydrological simulations with a macroscale runoff model in a resolution of 0.5°. They found that in case of underestimation or overestimation of precipitation by the regional climate model, a better approach would be to apply modelled changes in climate to observed data to drive the runoff model.

Regional downscaling of GCM outputs was performed for West Africa in a number of studies (section 3.3.3), as well as hydrological simulations (section 3.4.2), but the approach of a joint dynamical downscaling-hydrological modelling was not performed for a West African environment before.

Chapter 4

The Modelling System

Within the present study, output of the coupled *Atmosphere-Ocean Global Circulation Model* (AOGCM) ECHAM4/OPYC was downscaled dynamically with the mesoscale meteorological model MM5, and coupled to the hydrological model WaSiM to assess the impact of a globally changing climate on regional climate and hydrology. Within this chapter the different models are briefly described.

4.1 The Global Climate Model - ECHAM4/OPYC

The AGCM ECHAM4 is based on the ECMWF (*European Centre for Medium Range Weather Forecasts*) global meteorological model, and was further developed to be used as a global climate model at the Max-Planck-Institute for Meteorology and the DKRZ (Deutsches Klimarechenzentrum) in HAMburg. The prognostic variables that are calculated and made available as output at 12 hours resolution are vorticity, divergence, logarithm of surface pressure, temperature, specific humidity, and cloud water mixing ratio. A detailed description of the ECHAM4 model can be found in DKRZ (1993).

Horizontal Discretization ECHAM4 is a spectral transform model, at a medium resolution with triangular truncation at wave number 42 (T42). The partial differential equations are discretized using a pseudo-spectral method, which means non-linear and diabatic terms are calculated on a Gaussian grid at a resolution of 2.81 x 2.81 degrees.

Vertical Discretization For the vertical discretization a hybrid-sigma-pressure system with 19 non-equidistant layers is used. The upper boundary lies at a height of 10 hPa ($\sim$ 30 km).

Temporal Discretization A semi-implicit leap-frog-scheme employing a weak Asselin-filter (Asselin, 1972), suppressing the numerical mode is used for temporal discretization at a time step of 24 minutes for physics and dynamics. Additionally, a semi-implicit treatment of the terms of zonal advection of vorticity, divergence, humidity, temperature and surface pressure is included. The time step of radiation is 2 hours, and annual, as well as diurnal cycle of solar forcing are simulated. For the calculation of advection of water

vapour, cloud water and chemical substances a semi-Lagrangian method is used, in order to reduce truncation errors (WILLIAMSON and RASCH, 1994).

Horizontal Diffusion Horizontal diffusion is expressed using a hyper-Laplacian form, which leads to a damping of short wavelengths at the end of the spectrum.

Upper Boundary Condition To avoid fictitious reflection at the upper model boundary a high-diffusion sponge zone is built in, and applied to vorticity, divergence and temperature.

Radiation The radiation scheme uses a broad-band formulation of the radiative transfer equations. Absorption due to water vapour, CO2 and ozone are taken into account, as well as scattering and absorption due to aerosols and clouds, following the Mie-theory (ROCKEL et al., 1991).

Boundary Layer Processes and Eddy-Fluxes The calculation of vertical turbulent surface fluxes (momentum, heat, water vapour and cloud water) is based on Monin-Obuchov similarity theory for the surface layer, to account for the dependence of surface fluxes and diffusion coefficients from the stability of the atmosphere. In higher layers the eddy diffusivity approach is used (LOUIS, 1979).

Gravity Wave Drag The atmospheric loss of momentum through the formation of gravity waves, due to an interaction of stable layered flows with orography, is parameterized using directionally dependent sub-grid-scale orographic variances, obtained from a high resolution dataset (US Navy) (MILLER et al., 1989).

Gridscale (Explicit) Precipitation and Clouds Gridscale cloud water content is calculated from the respective budget equation, including transport of cloud water and a simplified representation of microphysical processes like condensation, evaporation, formation of cloud droplets through coalescence, and sedimentation of ice crystals. Sub-gridscale cloud formation is also parameterized (SUNDQUIST, 1978)

Sub-Gridscale (Implicit) Precipitation The bulk mass flux scheme of TIEDTKE (1989) is used to represent convective precipitation processes. Deep, mid level and shallow convection are considered. Organized entrainment is calculated from buoyancy, organized detrainment is computed from a spectrum of clouds detraining at different heights. An adjustment type scheme is used, rather than a moisture convergence closure scheme, which is used in the Tiedke scheme.

Land Surface Model (LSM) The soil and land surface model comprises the budgets of soil heat and water, snow cover and the heat budget of land ice. It takes into consideration the stomatal control of surface evapotranspiration through vegetation (SELLERS et al., 1986), interception, and the dependence of the sensible heat flux on snow coverage in a highly parameterized form. The LSM also includes a catchment based runoff scheme, that accommodates differing field capacities over inhomogeneous terrain.

Ocean model - OPYC The AGCM ECHAM4 was in addition coupled quasi- synchronously to the OPYC (Coupled Snow, Sea-Ice, Mixed Layer and IsoPYCnal Ocean Model) OGCM (Oberhuber, 1993). The two components of the coupled GCM exchange data on a daily basis. Momentum, heat and freshwater are passed from the AGCM to OPYC, which returns SST and sea ice variables (Röckner et al., 1999) to the atmospheric component.

4.2 The Regional Climate Model - MM5

MM5 is a mesoscale meteorological community model that was developed at the *National Center for Atmospheric Research* (NCAR) and the *Pennsylvania State University* (PSU) (Dudhia et al., 2003). It is a non-hydrostatic, multi-nesting capable model. MM5 offers a large variety of physics parameterizations for sub-gridscale processes, making it applicable to climatic and dynamic conditions around the globe.

Due to the large user community worldwide, it has been validated and tested intensively under different conditions. In the following section a short overview of MM5 as it is used within the present study is given, based mainly on Grell et al. (1995) and Dudhia et al. (2003).

Horizontal Discretization The horizontal discretization scheme of MM5 uses an Arakawa-B-grid staggering. Scalar variables are defined in the centre of the grid cell, whereas the horizontal velocity components are calculated in the corners. This allows a larger maximum time step compared to other methods.

Vertical Discretization The vertical discretization is performed in a sigma-pressure system, with respect to the hydrostatic reference pressure p_0. As a result, the pressure levels are height dependent, which makes this vertical sigma-pressure coordinate equivalent to terrain-following height coordinates (Grell et al., 2000). Scalar variables and horizontal velocity components are defined in the middle of each vertical model layer. The vertical velocity component is defined at full sigma levels.

Temporal Discretization A second order leapfrog scheme is used for temporal discretization of temperature, moisture and the slow terms of pressure and momentum. Sound waves, as components of the nonhydrostatic equations of motion, must be calculated with a shorter time step within the nonhydrostatic model for reasons of numeric stability. This is done using a semi-implicit time splitting scheme after Klemp and Wilhelmson (1978), in which vertically propagating sound waves are treated implicitly, whereas horizontally propagating sound waves are treated explicitly and time centred. A horizontal divergence damping technique after Skamarok and Klemp (1994) is applied. This leads to the short time step being solely dependent on the horizontal and independent of the vertical resolution.

Nonhydrostasy Given the purposes of this study non-hydrostasy is of major importance, as the hydrostatic equation can only be a good estimate of the atmospheric state at a

larger scale, specifically as long as the scale of vertical circulation features are smaller than the horizontal patterns' scale (PICHLER, 1997). In order to simulate the Volta Basin climate with a reasonably high resolution, nonhydrostatic dynamics must be considered. This includes the use of the fully compressible mass continuity equation. The diabatic heating term within the pressure tendency equation is the only term that is neglected.

Lateral Boundary Condition A relaxation procedure is induced to 'relax' the model-predicted variables at the lateral boundary towards the large-scale analysis. This is accomplished using a relaxation function that decreases linearly from the lateral boundary (GRELL et al., 1995). Vertical velocity is not nudged. A zero gradient condition is defined for cloud water, rain water, snow and ice on outflow, and additionally no inflow of these variables occurs.

Radiation The cloud-radiation scheme used incorporates short wave and long wave interactions with clear sky and explicit clouds (GRELL et al., 1995). Interaction with cloudy skies is simulated by a cloud parameterization scheme. An upper radiative boundary condition that allows wave energy to pass through unreflected was developed (KLEMP and DURRAN, 1983; BOUGEAULT, 1983).

Planetary Boundary Layer (PBL) The Hong-Pan PBL scheme, based on a nonlocal boundary layer vertical diffusion scheme of Troen and Mahrt was used in the present study (HONG and PAN, 1996). The largest difference between this non-local K approach and the local K approach is that transport of mass and momentum in the planetary boundary layer are determined by the bulk properties of the PBL rather than the local properties. This is important, because these transports strongly depend on large eddies in the PBL. Within this PBL scheme vertical diffusion is simulated, using an implicit scheme to allow a longer time step (DUDHIA et al., 2003).

Gridscale (Explicit) Precipitation and Clouds For the calculation of gridscale precipitation, microphysical processes that influence precipitation formation and conversion processes between the different phases of water must be parameterized. This scheme is activated as soon as saturation at a grid point is reached. The Reisner Graupel scheme is used within the present study. This scheme is based on the Reisner mixed phase scheme (REISNER et al., 1998), and includes the calculation of cloud water, cloud ice, rain water, snow, super cooled water, melting of snow, graupel and ice particle number concentration.

Sub-Gridscale (Implicit) Precipitation The sub-gridscale precipitation scheme, often referred to as the cumulus parameterization, produces precipitation before gridscale saturation is reached, to account for sub-gridscale processes as well as grid-scale instability associated with a saturated conditionally unstable atmosphere (BETTS, 1986). The Grell scheme used here (GRELL and KUO, 1991) includes updraft and downdraft. No entrainment and no detrainment are considered along the cloud edges. Therefore, mixture of clouds and surrounding air only takes place at the top and the bottom of the circulations. A constant mass flux with height is assumed. In addition, no cloud water is produced; all condensate water immediately falls out as rain/snow. The closure scheme relates the amount of

convection to the destabilization rate by the environment. A quasi-equilibrium between destabilization by the large-scale environment and stabilization by convection is assumed.

Shallow Convection Additionally a shallow convection scheme is implemented to account for shallow, non precipitating convection that is forced by sub-grid scale processes (Grell et al., 1995).

Lower Boundary Conditions Originally MM5 used fixed lower boundary conditions for SST, soil moisture and soil temperature. MM5 version 3.5 introduced the option of using variable lower boundary conditions. In this context the introduction of a variable SST is very important for West Africa, because a large portion of climatic variability is connected to SST anomalies (section 2.1). Another improvement was the coupling of a land surface model to the lower boundary.

Because mesoscale structures within the planetary boundary layer are strongly influenced by topography, soil moisture and vegetation, one of the most important features for long-term integrated model runs is a sophisticated Land Surface Model (LSM). Given the capacity of the soil to act as a memory of past meteorological conditions, soil-atmosphere feedback mechanisms must be considered. These feedback mechanisms have been shown by Jung (2001) and Kunstmann and Jung (2003) to be especially important for rainfall in the Volta Basin (compare section 2.1).

The introduction of the Oregon State University land surface model (OSU-LSM) into MM5 Version 3 established the conditions, under which MM5 can be utilized as a regional climate model. The OSU-LSM is a fully developed 1-dimensional SVAT (*Soil Vegetation Atmosphere Transfer*) Model. It consists of 4 soil layers with a thickness of 10, 30, 60 and 100 cm, respectively. Soil temperature is derived by solving the diffusion equation, including heat capacity and thermal conductivity as a function of soil moisture (θ). Hydraulic conductivity and diffusivity are also functions of θ. Evaporation from the soil surface, as well as interception, direct runoff, interflow and vertical, gravitational soil water fluxes are considered. A simple snow model is included in OSU-LSM that, while unimportant for West Africa, is an indispensable feature for other regions. Temperature at the lower boundary of the model is defined as the mean of the annual cycle and assumed to be found at 3 meters below surface.

4.3 The Hydrological Model - WaSiM

The hydrological model that was used for the present study is the Water Balance Simulation Model, abbreviated as WaSiM, developed at the *Swiss Federal Institute of Technology* (ETH). It is a physically based hydrological model, suitable for flood modeling as well as for long-term water balance simulations, and designed for application in mesoscale and large scale basins (spatial resolutions between some meters and kilometers) and temporal resolutions from hours to days. The physical part of the model is the simulation of the unsaturated zone, whereas discharge generation is parameterized. A detailed description of WaSiM, its basic equations, and a detailed tutorial can be found in Schulla (1997) and Schulla and Jasper (2002).

Preprocessing

The Topographical ANALYSis preprocessor TANALYS calculates input information for WaSiM, including flow net structure, flow directions, flow times, sub-catchment boundaries, exposition and slope from the *Digital Elevation Model* (DEM).

Processing

Figure 4.1 shows the flow chart of the processing within WaSiM, including the different modules. These will be described briefly in the following.

Precipitation Correction A correction is performed on precipitation input in the case where observational data is used, because rainfall measurements are typically subject to errors (in WaSiM only the wind induced measurement error is accounted for). For the coupled climate-hydrology simulations no precipitation correction was performed.

Meteorological Input Handling Meteorological input data are: precipitation, temperature, relative humidity, wind velocity, global or net radiation, sunshine duration and vapour pressure. Of these input variables only temperature and precipitation are essential. These data, given as station values, are then interpolated on a regular grid. Different methods are available for interpolation:

- *Inverse Distance Weighting (IDW)*
  This interpolation scheme uses all available station data within a specified search radius and performs a distance weighting.
- *Altitude dependent regression*
  In mountainous catchments this can be very important for variables that have a stronger dependence on altitude than on horizontal position, like temperature, wind speed and vapour pressure.
- *Combination*
  A combination of both altitude dependant regression and IDW is feasible, if variables are both, horizontal and vertical dependent, especially if temporal and spatial resolution are coarse.
- *Thiessen Polygons*
  This method is similar to IDW, but only considers the influence of the station nearest to a certain grid point.
- *Bilinear Interpolation*
  IN the particular cases of equidistant, gridded input data or almost equidistant station data with a high density the method of bilinear interpolation is less time consuming but effective.

Within the present study, IDW interpolation was satisfactory for an interpolation of observational station data in the calibration runs. Due to the flatness of the terrain altitudinal regression was not required. For the coupled model runs the bilinear interpolation method was applied.

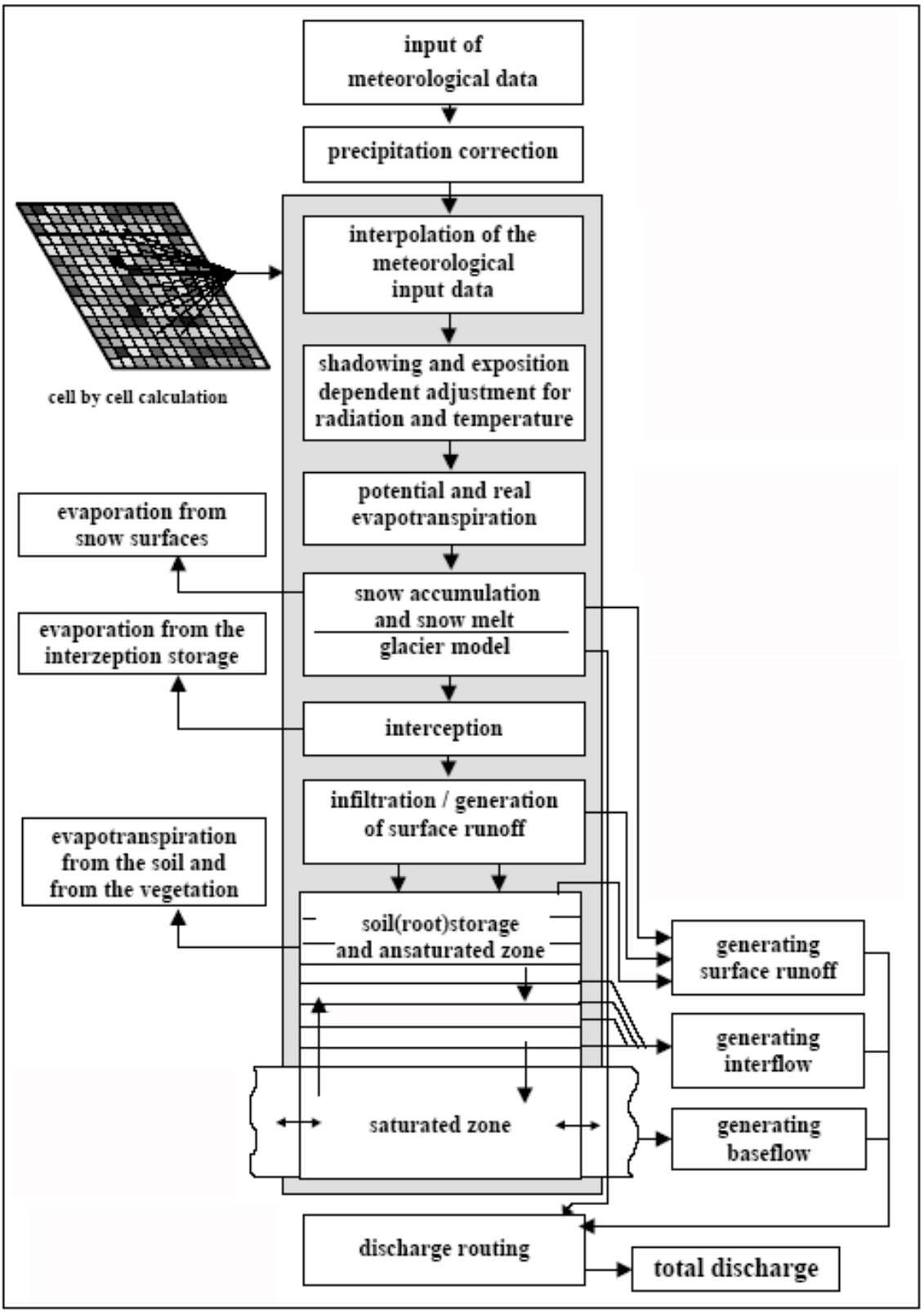

Figure 4.1: Model structure: WaSiM, modified after Schulla and Jasper (2002)

Radiation and Temperature Adjustment A topographically dependent correction for radiation is implemented to compensate for shading effects due to topography in mountainous regions. As sensible heat flux and therefore temperature depend on incoming radiation, an additional modification of temperature input is performed. The influence of topography on radiation and temperature is accounted for, following an approach of Oke (1987).

Potential and Real Evapotranspiration Potential evaporation is calculated using an approach of Penman-Monteith (Monteith, 1975; Brutsaert, 1982). In this approach, the most important plant properties are taken into consideration, e.g. stomata resistance, root density distribution and depth, LAI (*Leaf Area Index*), effective vegetation height, vegetation coverage degree and a critical soil water content below which transpiration starts to diminish. To determine real evapotranspiration, the first step is to reduce potential evaporation by the amount of water equal to interception storage. Then, considering soil and plant physiological properties, a further reduction of potential evaporation is performed dependent on the actual suction of the soil.

Interception A simple bucket approach is used to calculate interception storage dependent on LAI, vegetation coverage degree and the maximum height of the water layer on plants.

Snow Module WaSiM also includes a snow module, which simulates melting and accumulation of snow.

Infiltration The calculation of infiltration after Dyck and Peschke (1995) follows the approach of Green and Ampt (1911). When saturation is reached, or in case precipitation intensity exceeds infiltration capacity, the excess rainfall becomes direct runoff. Macro pore flux is not considered. It can be approximated by using a generally higher effective hydraulic conductivity of the soil matrix. This is a limitation to model performance for the Volta Basin. Another weakness, especially when simulations are performed in a coarse temporal resolution is, that rainfall intensity is assumed to be constant over the entire time step.

Unsaturated Zone For the calculation of vertical soil water movement in the unsaturated zone, the spatially and temporally discretized one-dimensional Richards equation is solved for each grid cell. This second order differential equation that is solved in WaSiM allows a modelling of vertical moisture profiles and flux profiles and the simulation of percolation, as well as capillary rise. Hydraulic head and hydraulic conductivities are dependent on soil moisture, and these relationships are parameterized through an approach after van Genuchten (1976). Through the introduction of a recession constant for vertical hydraulic conductivity, indicating a recession with depth, the generation of interflow is enabled. Groundwater recharge in WaSiM is defined as the remaining vertically percolating water. No heat balance is calculated in WaSiM. Therefore the soil heat flux is considered to be a fixed fraction of net incoming radiation. This fraction is constant for all months.

Groundwater Module A two-dimensional groundwater flow module is dynamically coupled to the unsaturated zone module. Figure 4.2 illustrates an example of simulated groundwater potential and subsequent flow directions. The simulation of lateral fluxes within the

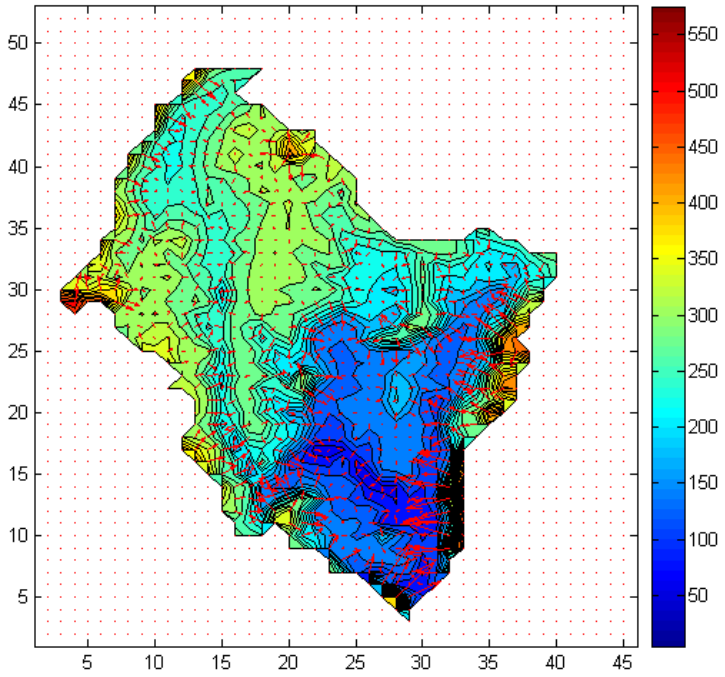

Figure 4.2: Simulated groundwater potential [m] (shaded) and flow directions (arrows), 1968

aquifers is based on the mass balance equation and Darcy's law. The model has the ability to simulate multiple aquifers. Connections between aquifers, as well as interactions between surface water and subsurface water are simulated with the leakage principle. Therefore baseflow, which is the groundwater derived part of river discharge, can only be generated when groundwater levels reach the river bed or lake bottom level. Re-infiltration of surface water into groundwater occurs, if groundwater drops below river water level. This is an advantage when simulating hydrology of semi-arid regions.

Discharge Routing Direct runoff and interflow are routed with respect to flow times that are calculated by the preprocessor TANALYS for the entire catchment and so reflect the distance to the outlet. These flow times are calculated following the Manning-Strickler equation (Maidment, 1993). The routing is done by a kinematic wave approach, using different flow velocities for different water levels in the channel. Retention is simulated with a simple linear storage approach for direct runoff, as well as for interflow.

Additional Capabilities It is also possible to simulate irrigation control techniques, regulated reservoirs, artificial abstractions, ponding of water, clay layers and tracer transport.

Chapter 5

Setup and Calibration of the Modelling System

The following sections describe the setup of the modelling system for the present study. First, the domain setup, the spatial and temporal discretization, and the input data of MM5 are described (section 5.1). Then, an overview of the setup of the hydrological model WaSiM for the specific requirements of the Volta Basin (section 5.2.1) and the calibration strategy (section 5.2.2) are given. Finally, in section 5.3.3 the technical realisation of the modelling, including the model coupling is briefly outlined.

5.1 MM5 - Setup

5.1.1 Domain Setup and Discretization

Domain Setting Some advantages and limitation of dynamical downscaling were mentioned in section 3.3.2.

In the tropics, where lateral boundary forcing in general is weak, and in large RCM (Regional Climate Model) domains, it is more likely that RCM simulations develop a circulation distinct from the pattern of the GCM. Whether or not this is an advantage for the credibility of regional climate simulations has been widely discussed. Some researchers claim that the circulation of the RCM should not differ extremely from that of the GCM (Jones et al., 1995), while others assume that large domains should be used in regional climate simulations, to allow for the atmospheric circulation to be modified by the RCM at spatial scales that are not well represented by the GCM (Wang et al., 2004). Nevertheless one has to address the limitations concerning lateral boundary conditions, in order to find the right domain choice for reliable regional climate simulations.

Within this study it was demanded for the first modelling domain, to be large enough to allow distinct circulations to develop. The third domain in particular was not only chosen to include the Volta Basin, but also to cover the whole of Benin, to allow collaboration with researchers of the IMPETUS project (*www.impetus.uni-koeln.de*), who are investigating the influence of a changing climate to the Ouémé catchment in Benin.

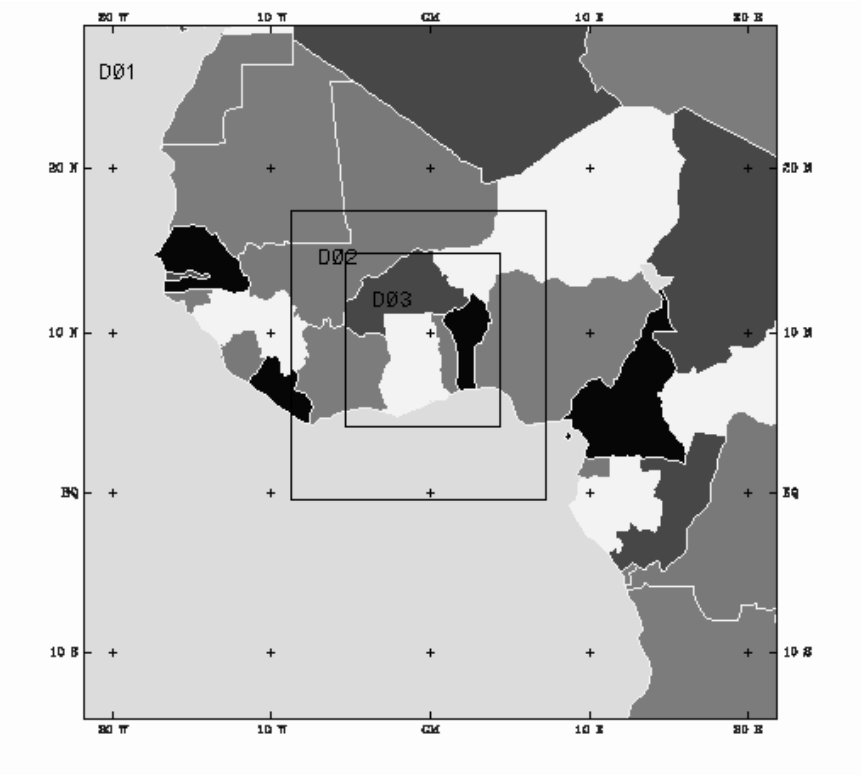

Figure 5.1: Domain setup: MM5

Lateral Boundaries It is advisable to avoid placing the RCM lateral boundaries over regions with known GCM biases (WANG et al., 2004) or erroneous moisture transport. Care was taken that the lateral boundaries over the ocean, where possibly errors in moisture transport can occur and boundary effects could be observed, are positioned far away from the area of interest, as advised, for example, by WARNER et al. (1997).

Nesting The MM5 simulations were performed using a 1-way nesting approach, involving the nesting of 3 model domains (figure 5.1).

Discretization The horizontal resolution of the 3 domains was 81 km for the largest domain (D1), covering entire West Africa, 27 km for the second (D2) and 9 km for the smallest domain (D3), covering the larger Volta region ($\sim$ 800000 km^2). This means a simulation of 4792 (D1), 3721 (D2), and 16456 (D3) gridpoints. For vertical discretization 25 layers were calculated. The model top level was set to 30 hPa instead of the standard value of 100 hPa to account for the higher tropopause level in the tropics. The time step ranged from 120 s for the largest model domain (D1) to 20 s in the highest resolution (D3).

Parameterizations The selection of the parameterization schemes was done by performing multiple model runs, and is described in KUNSTMANN and JUNG (2003). A short description of the parameterization schemes that were chosen is given in section 4.2.

5.1.2 Simulation Setup

Differences in the simulation setup of the regional climate simulations and the validation runs of MM5 lay only in lateral and lower boundary condition, due to different input data.

Validation Runs

For both validation runs, reanalysis data provided initial and boundary condition. These were obtained from NCEP (*National Centers for Environmental Prediction*) for the year 1997, and from ECMWF (*European Centre for Medium-Range Weather Forecast*) for 1968.

Regional Climate Simulations

GCM and Emission Scenario The initial and boundary fields of the climate runs were derived from a transient ECHAM4 global climate model run from 1860-2100.

To take into account the high degree of uncertainty in future climate change, it was recommended within the 1995 IPCC review (Houghton et al., 1995) to use the full range of emission scenarios. Due to the extensive demands on computational capacity (compare section 5.3.2), this advise could not be followed here. In the present study the scenario IS92a was used. Concerning CO_2 emissions, this scenario lies in a central position with respect to the new SRES scenarios (compare section 3.1). The underlying assumption of an annual increase in CO_2 of 1% per year leads to an effective CO_2 doubling time of about 90 years (May and Röckner, 2001).

The ECHAM4 run that was provided by the DKRZ and used for this study did not consider sulphur aerosols, because this was (as mentioned in section 3.1), the largest source of error within the IS92 scenarios. In addition, SO_2 emissions play a minor role in West Africa, and through the short life-time of sulphate aerosols that forestalls a transport from far into the region, this component is assumed to be negligible.

Although IS92a is an intermediate scenario, it is not necessarily the most likely one (Houghton et al., 1995). However, given the complexity of all factors influencing future conditions, choosing an intermediate emission scenario seems the best possible way to go, when ensemble runs are not feasible.

Time Slice Experiment Two 10 year time slices were chosen for downscaling, 1991-2000 for the reference state climate, representing present climate and 2030-2039 for the proposed future climate. The IS92a scenario increase of 1% of CO_2 per year means a CO_2 increase of almost 100 ppmv between 1990 and 2030.

Initial Soil Conditions Wang et al. (2004) concluded, that initial soil moisture conditions can have a significant effect on predictability, due to its long lasting influence. Therefore, as soil moisture fields were not available from the ECHAM4 output, the simulation was started in the dry season (January), where soil moisture differences between years are small. The initial state of soil moisture was derived from NCEP reanalysis data of January 1992.

5.2 WaSiM

5.2.1 Setup

The hydrological model WaSiM has not been used in a catchment of a comparable size, nor in a semi-arid environment before. It has been applied primarily in small, mid-latitude, largely mountainous catchments (Niehoff, 2001; Schulla and Jasper, 2002; Kleinn, 2002; Kunstmann and Stadler, 2003; Kunstmann et al., 2004). To account for the specific conditions in the large and extraordinarily flat Volta catchment located in a semi-arid to sub-tropical environment, certain adaptations to WaSiM and its preprocessor TANALYS had to be done. These adaptations, as well as the general setup will be described in the following section.

Resolution The resolution of WaSiM used in this study is 1x1 km^2 for the horizontal, and 24 hours for the temporal resolution. The temporal resolution was restricted by the availability of calibration data. No data below a resolution of 24 h was available. In the vertical the soil is represented by 20 layers of an equal thickness of 1 m each.

Subcatchments A subset of gauges was chosen to define the subcatchments to be simulated. These gauges were selected on the basis of data availability and data quality for the 1960s, which was chosen as the calibration period. For the demarcation of Lake Volta several other, 'artificial' gauges had to be set at the smaller tributaries to Lake Volta where no gauging stations for the chosen time period were available. Another surplus gauge had to be set, to define an 'artificial' subcatchment at Sourou due to the specific flow characteristics (see following paragraph), to allow a handling of river extractions within the model that will be described later in this section. The subcatchments and the respective area dimensions are illustrated in figure 5.2 and summarized in table 5.1.

Table 5.1: Gauge numbers, names, countries (BF: Burkina Faso, GH: Ghana) and subcatchment sizes

Gauge	Name	Country	Subcatchment Size [km^2]
4	Aframso	GH	1066
7	Akosombo	GH	30781
14	Bamboi	GH	38211
18	Boromo	BF	35723
27	Dapola	BF	33162
30	Ekumdipe	GH	5948
33	Hohoe	GH	703
54	Nawuni	GH	37280
63	Pruso	GH	1326
64	Pwalugu	GH	56760
67	Saboba	GH	55817
84	Yapei	GH	11087
102-116	artificial	GH	58631
202	Sourou	BF	36498

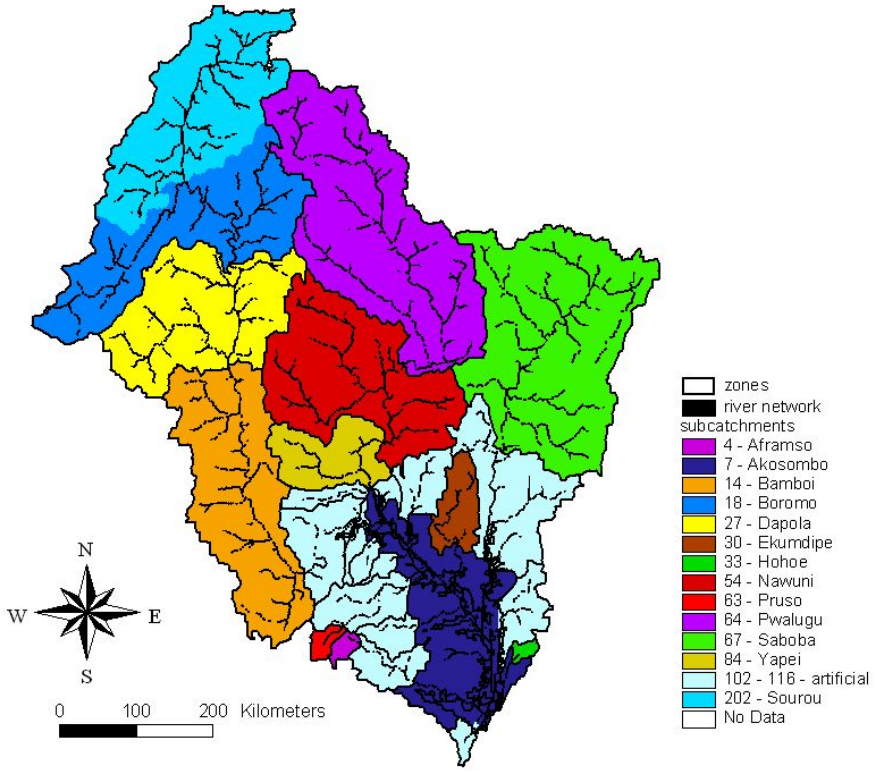

Figure 5.2: WaSiM setup: Subcatchments and flow net structure

Sourou Depression The Sourou depression is shown in figure 5.3. Within the depression, in times of flood, water from the Mohoun is 'captured' (section 2.2). Therefore, this area requires an unconventional specification.

Since TANALYS tries to fill small singularities in the DEM when the flow net structure is calculated, the water is not allowed to stay in the depression but will follow, even if slowly, the flow path south to join the Mohoun. The inflow from the Mohoun into the Sourou depression during periods of flooding is even more difficult to represent. The calculated flownet structure permits flow according to one direction only, at all times.

To deal with the problem, an additional 'artificial' gauge was defined to demarcate the area North from the Mohoun subcatchment. An extraction from the subcatchment of Boromo, which now includes the entire Mohoun down to Boromo but excluding the Sourou, was built to account for the outflow from the Mohoun to the Sourou depression during flooding. This was achieved by setting a minimum outflow value from the Mohoun to the Sourou, and additionally setting a percentage of the actual flow to be extracted, in case runoff exceeds the minimum outflow value.

To achieve a better representation of evapotranspiration from the depression, a pond grid was defined, which represents the area where storage of water occurs and ensures that evaporation is in the first instance taken from the pond grid cells. Additionally, because outflow from the Sourou depression was still too high, a no-flow condition was defined for river runoff from Sourou to the subcatchment of Boromo.

Geohydrology A hydro-geological map (figure 5.4) was derived from MARTIN and VAN DE GIESEN (2005). This map is based on various hydro-geological maps and sources of information from Ghana and Burkina Faso. No other countries' information was available, so for the hydrological model input, the hydro-geological units were extrapolated to the regions of the Volta Basin that lie outside of Ghana and Burkina Faso.

Information on horizontal hydraulic conductivities, storage coefficient and aquifer thickness were classified for each geohydrological unit. The values of hydraulic conductivities, as well as the aquifer thicknesses were provided by MARTIN and VAN DE GIESEN (2005), for storage coefficients these soil specific values were taken from general (not subcatchment specific) literature (MAIDMENT, 1993). These values were implemented into WaSiM grids, as spatially distributed parameters.

Land-use Land-use data (figure 5.5) was derived from project partners (VESCOVI, 2001). The land-use specific parameters were obtained from GRELL et al. (1995) and SCHULLA and JASPER (2002).

Soil Soil texture (figure 5.6) was derived from the global FAO (*United Nations Food and Agriculture Organization*) soil map (FAO, 1971-81). The van Genuchten parameters for tropical soils were derived from HODNET and TOMASELLA (2002). The remaining soil hydraulic properties were either derived from MAIDMENT (1993), or SCHULLA and JASPER (2002).

Model Parameters Table 5.2 summarizes the most important parameters needed for the various modules of WaSiM along with their respective sources.

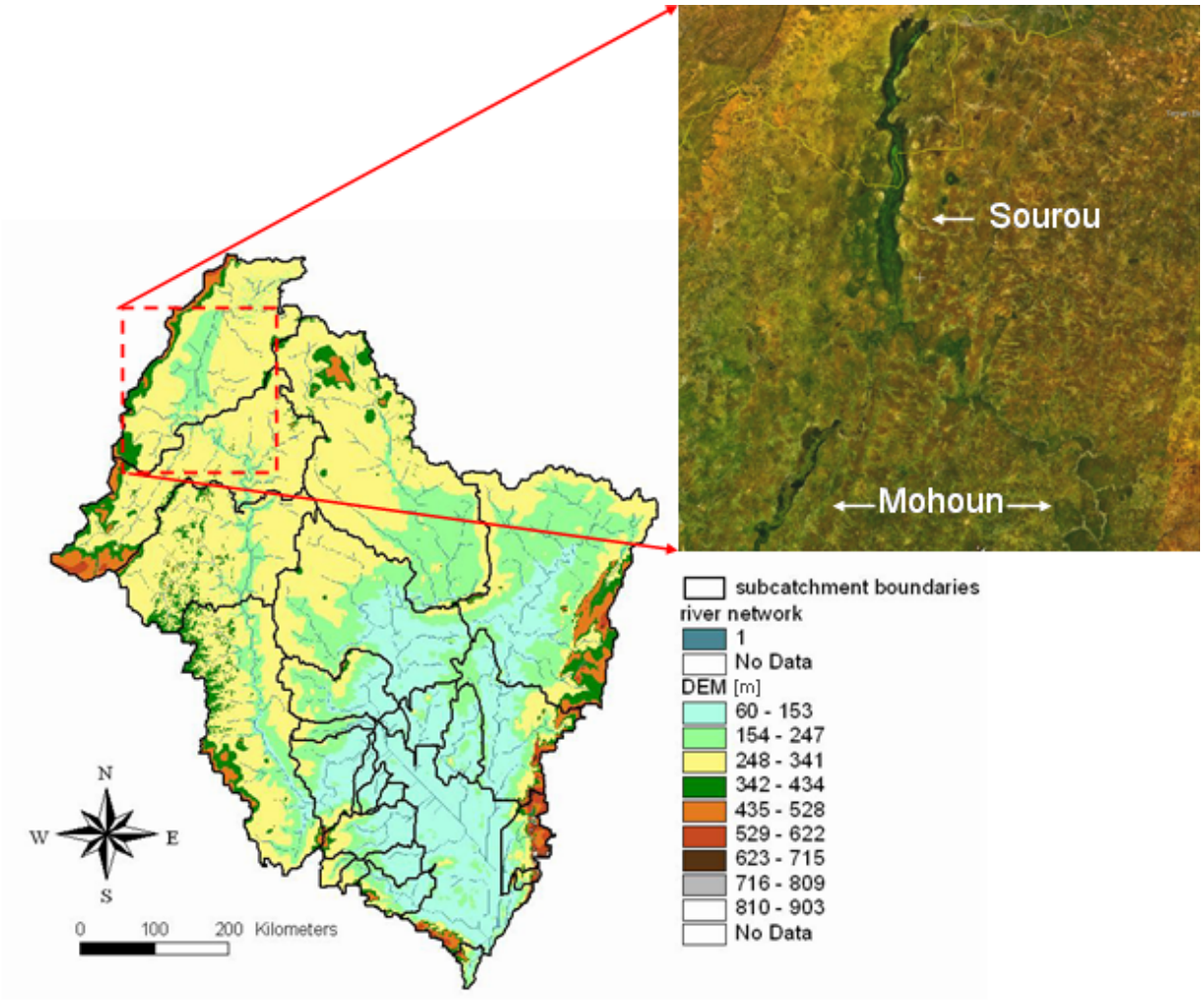

Figure 5.3: WaSiM setup: Digital elevation model (DEM) [m] and Sourou depression (*http: wordlwind.arc.nasa.gov)*

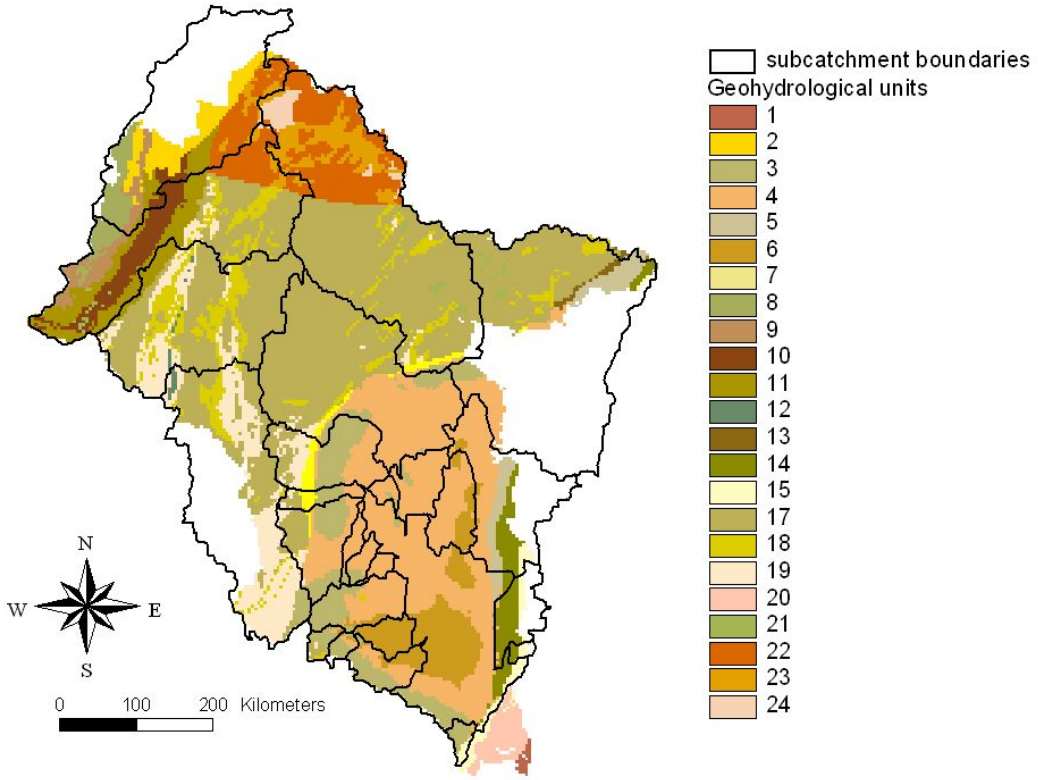

Geohydr. unit	Group	Lithology	Aquifer thickness [m]
1	Recent	Sandstone	30
2	Recent	Argillaceous sandstone	72.15
3	Sedimentary rocks / Voltaian	Argillaceous sandstone	39.21
4	Sedimentary rocks / Voltaian	Siltstone, shale, sandstone	38.55
5	Sedimentary rocks / Voltaian	Siltstone, shale, sandstone	24.4
6	Sedimentary rocks / Voltaian	Sandstone	32.43
7	Sedimentary rocks / Voltaian	Sandstone	30
8	Sedimentary rocks / Zone sedimentaire	Argillaceous sandstone	50.6
9	Sedimentary rocks / Zone sedimentaire	Sandstone, schist, conglomerate	48.17
10	Sedimentary rocks / Zone sedimentaire	Siltstone, sandstone, carbonate	61.08
11	Sedimentary rocks / Zone sedimentaire	Sandstone	53.38
12	Sedimentary rocks	Sandstone	29.55
13	Sedimentary rocks	Sandstone	33.35
14	Sedimentary rocks / Infracambrian	Sandstone, schist, conglomerate	30.12
15	Sedimentary rocks / Infracambrian	Sandstone, schist, conglomerate	39.02
17	Precambrian igneous and metamorphic rocks	Granite, granodiorite, migmatite, gneiss	25
18	Precambrian igneous and metamorphic rocks	Vulcanics and Metavolcanics (Tufs, lava, pyroclastics)	24
19	Precambrian igneous and metamorphic rocks	Metasediments (phyllite, tuff, greenstone, greywacke)	30
20	Precambrian igneous and metamorphic rocks	Gneiss	15.1
21	Precambrian igneous and metamorphic rocks	Basic Intrusives (amphibolites, dolerite)	29.46
22	Precambrian igneous and metamorphic rocks	Granite, granodiorite, migmatite, gneiss	30
23	Precambrian igneous and metamorphic rocks	Vulcanics and Metavolcanics (Tufs, lava, pyroclastics)	30
24	Precambrian igneous and metamorphic rocks	Metasediments (phyllite, tuff, greenstone, greywacke)	30

Figure 5.4: WaSiM setup: Geohydrological units and main characteristics (Martin and van de Giesen, 2005)

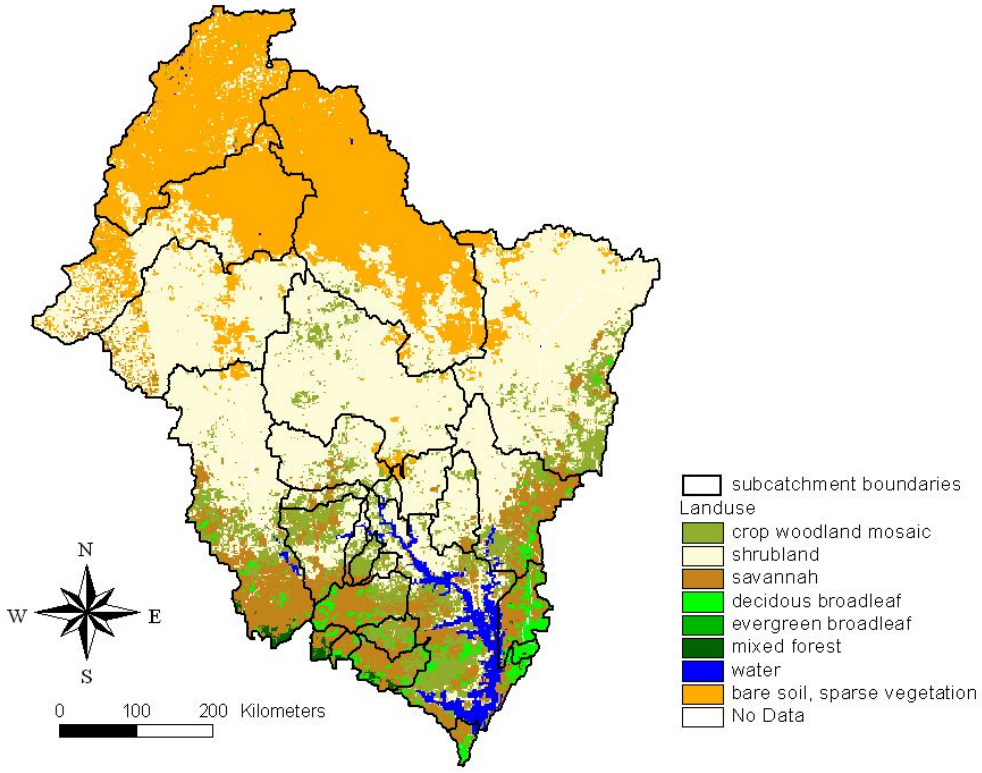

Figure 5.5: WaSiM setup: Land-use discretization (Vescovi, 2001)

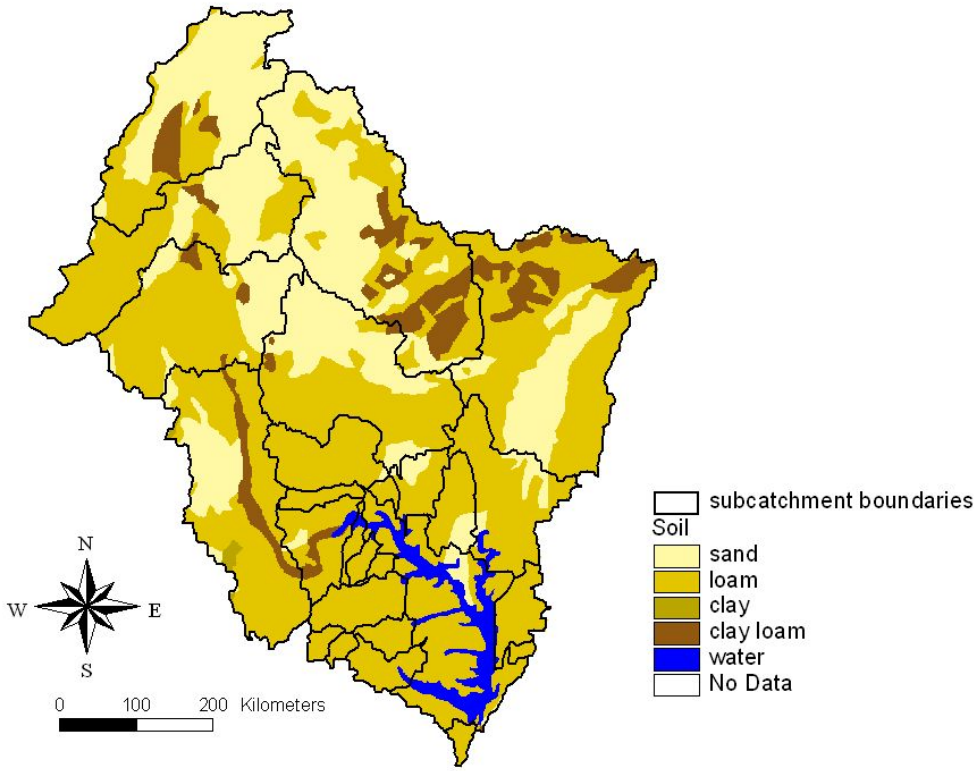

Figure 5.6: WaSiM setup: Soil texture (FAO, 1971-81)

Table 5.2: Parameters and source of parameter values for WaSiM (calc=calculation, lit=literature, calib=calibration, est=estimate)

	WaSiM parameter		source
Meteorological Input			
Precipitation			
	$Aniso$	anisotropy for precipitation interpolation	calc
Temperature			
	ΔT_{sea}	maximum daily ΔT at MSL	calc
	k_T	change in ΔT with height	calc
Evapotranspiration			
	cr_{0-3}	for global radiation calculation from SSD	calc
Soil Model			
	K_D	storage coefficient for surface runoff	calib
	K_I	storage coefficient for interflow	calib
	d_r	drainage density for interflow	calib
Groundwater Model			
	K_{sat}	saturated hydraulic conductivity	lit
Soil Table			
	Θ_{sat}	saturation soil moisture content	lit
	Θ_{wp}	wilting point soil moisture content	lit
	K_{sat}	saturated hydraulic conductivity	lit
	α	van Genuchten parameter	lit
	n	van Genuchten parameter	lit
	K_{rec}	recession constant for $K_{sat}(z)$, z: depth	calib
	c_k	limit of the K_{sat} relation between layers	calib
	m_{SB}	fillable porosity	lit
Land-use Table			
	r_{sc}	minimum surface resistance (monthly)	lit
	LAI	leaf area index	lit
	v	vegetation coverage degree	lit
	z_0	effective crop height	lit
	α	albedo	lit
	z_w	root depth	lit
	$d_1 - d_4$	julian days	est
	ρ	root density distribution	lit
	ϕ_g	minimum suction for reducing etr	lit

River Network Properties The calculation of flow times and flow time sums turned out to be particularly difficult in the extremely flat terrain of the Volta Basin. To avoid extremely small slopes, a minimum slope is set to 0.001 within TANALYS. With this original configuration of TANALYS, the minimum slope was reached for several subcatchments of the Volta Basin. This resulted in shorter flow times that lead to a time shift in the resulting discharge curve. The minimum slope was reset to 0.0001, and the flow times changed accordingly. In combination, the minimum flow velocity was reduced to 0.01 m s^{-1}, from 0.1 m s^{-1} in the standard version. Furthermore the constant Manning-roughness parameter of M=10 $m^{1/3}s^{-1}$ was changed to M=5 $m^{1/3}s^{-1}$ following MAIDMENT (1993). In addition WaSiM has a default ratio of channel width to channel depth of 1/10. As a result river depths turned out to show extreme values for the Volta Basin. Therefore this ratio was determined to be smaller. A value of 1/30 based on estimates from observations was chosen.

Seasons In the Volta Basin the mid-latitudal definition of seasons does not hold. Here two main seasons can be distinguished: The rainy season (approximately May-October) and the dry season (approximately November-April). As outlined in section 4.3, several parameters within the land-use table, that are necessary for evapotranspiration modelling correspond to 4 phenological points for the 4 seasons, respectively. Between these points, the values are linearly interpolated. For the application of WaSiM in the Volta Basin the number of phenological points was reduced to two. The two phenological points are defined at DOY (Day Of the Year) 120 for the beginning of the rainy season and 304 for the beginning of the dry season.

Height Dependence of Seasonality To account for the strong climatic height dependence in mid-latitude, mountainous regions, the length of the vegetation phase in WaSiM is shortened, dependent on terrain height. This means that with increasing height springtime and summer tend to start later and end earlier. For West Africa this does not hold true. Even if the amounts of rainfall during the rainy season are determined partly by the presence or absence of mountains, and therefore show a certain height dependence, the onset and secession of the rainy season, and therefore the vegetation development are definitely not. Consequently the terms controlling height dependence were removed.

Soil Heat Flux Soil heat flux within WaSiM is assumed to be 10% of net incoming radiation. On the basis of meteorological measurements that were performed in 2001 within the framework of the GLOWA-Volta project at three sites in Ghana (Tamale, Ejura and Navrongo), soil heat flux was determined to be approximately 20% of net incoming radiation (MARX, 2003). Subsequently, for this study the fraction of 0.2 was implemented in the WaSiM routine that calculates soil heat flux from net radiation.

Potential Evaporation Compared to observations, evapotranspiration as simulated by WaSiM was found to exhibit an inaccurate annual cycle. Within the simulations, a maximum rate of evapotranspiration was found to occur just at the end of the rainy season. Observations (OBENG-ASIEDU, 2004) indicated an annual cycle of evapotranspiration with a single maximum at the height of the rainy season.

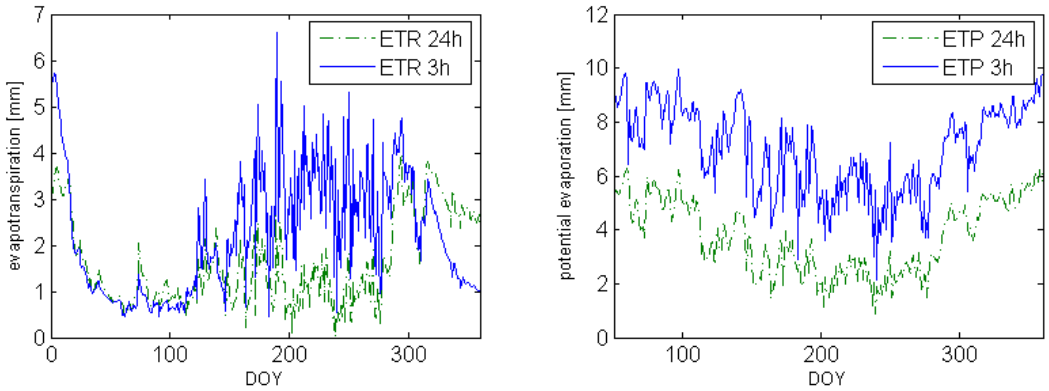

Figure 5.7: Left: Daily evapotranspiration [mm], right: Daily potential evaporation after Penman-Monteith [mm], simulated with 3 h and 24 h time steps

The faulty maximum in the simulations basically indicates soils that are too wet at the end of the rainy season. Subsequently in long-term model simulations an accumulation of soil moisture was observed. The surplus of soil moisture was found to result from comparably small evapotranspiration values during the rainy season.

To get some insight into this problem, two simulations (here in the coupled MM5-WaSiM version), one with a 3 h time step (further on referred to as WAS3) and the other with a 24 h time step (WAS24) were compared. First, the simulated evapotranspiration turned out to be more realistic in the 3 h resolution simulation (figure 5.7, left) in comparison to MARTIN (2005). She demonstrated potential evapotranspiration rates within the Volta Basin of 10 mm d^{-1} at the end of the dry season, and 4-5 mm d^{-1} in the rainy season. The reason for this more realistic WAS3 run was detected in the calculation of potential evaporation. As illustrated in figure 5.7 (right), potential evaporation is significantly higher in WAS3, than in WAS24. This results in higher real evaporation values during the rainy season, when water availability is high. As a consequence, the soil dries out faster, and the increase in real evapotranspiration due to an increase in potential evaporation at the beginning of the dry season vanishes in the WAS3 runs.

In the calculation of potential evaporation after Penman-Monteith in equations 5.1 and 5.2, WaSiM differentiates between day and night potential evaporation:

$$ETP_{day} = \frac{\Delta_{day}(R_{N,day} - G) + \rho_p c_p (e_{s,day} - \overline{e})}{\Delta_{day} + \gamma(1 + \frac{r_{s,day}}{r_a})} \tag{5.1}$$

$$ETP_{night} = \frac{\Delta_{night}(R_{N,night} - G) + \rho_p c_p (e_{s,night} - \overline{e})}{\Delta_{night} + \gamma(1 + \frac{r_{s,night}}{r_a})}(1 - d) \tag{5.2}$$

with Δ_{day} and Δ_{night} the slopes of the saturated vapor pressure curve for T_{day} and T_{night} respectively
$R_{N,day}$ and $R_{N,night}$ net radiation for day and night [Wh m^{-2}]
$e_{s,day}$ and $e_{s,night}$ saturation vapor pressure [hPa] as function of T_{day} and T_{night} respectively
$r_{s,day}$ and $r_{s,night}$ surface resistance of vegetation for the bright day
d relative duration of the bright day $(h_{ss} - h_{rs})/24$
G ground heat flux [Wh m^{-2}]

ρ_p density of dry air at MSLP and 0°C (1.29 [kg m^{-3}])
γ psychrometric constant [hPa K^{-1}]
$r_{s,day}$,$r_{s,night}$ bulk-surface resistance [s m^{-1}]
r_a bulk-aerodynamic resistance [s m^{-1}]
c_p specific heat capacity of dry air at constant pressure (1005 [J kg^{-1}K^{-1}])

This calculation is based on a differentiation of mean day temperature between a mean temperature of the bright day, and a mean night temperature. These temperature values are determined from mean day temperatures, with the use of empirical values for the monthly mean maximum daily temperature amplitudes, and the mean length of the bright day. Through temperature dependence saturation vapour pressure and saturation deficit $e_{s,day} - \overline{e}$ subsequently show a day-night contrast, whereas wind velocity does not.

In an idealized form (setting all constant values to 1), the Penman equation as it is used in WaSiM was programmed and used for a sensitivity study to investigate the influence of the certain meteorological input variables. First, this idealized representation of potential evaporation ETP_{id} was calculated with the input variables in a 3 h time step and summed up for daily values. Alternatively the input variables were aggregated to 24 h sums (e.g. radiation and precipitation) or averaged over a day (temperature, wind velocity and relative humidity). Then, the sensitivity of the formulation to the different temporal resolutions was analyzed separately for wind, relative humidity, temperature and global radiation.

The results showed a minor influence of temperature, relative humidity and global radiation, but a large influence of the averaging of wind speed on the model solution. According to Schulla (2005), a consideration of daily varying wind velocities would be an advantage in regions where strong differences between day and night are observed in wind speed.

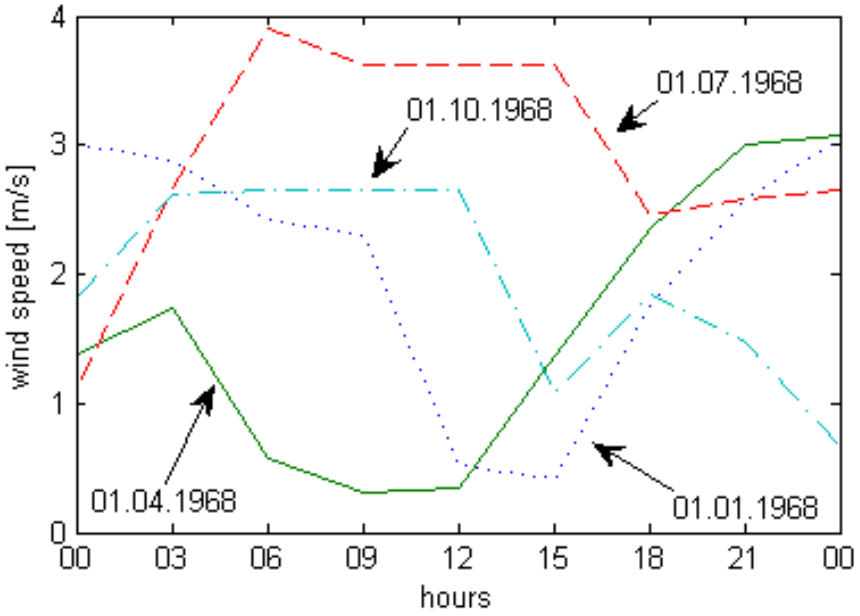

Figure 5.8: Day-night differences in wind speed [ms^{-1}] in the Volta Basin for selected days

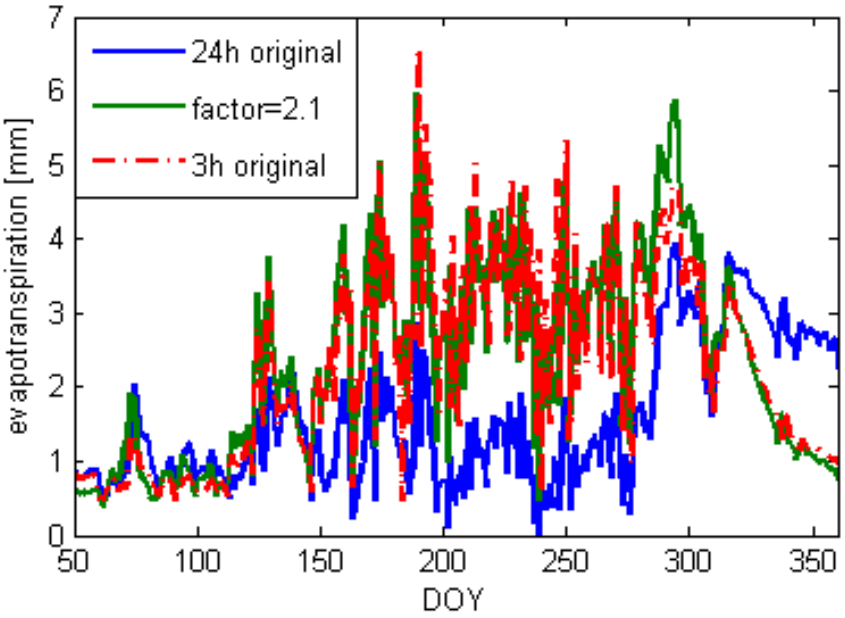

Figure 5.9: Evapotranspiration [mm] calculated with 3 h time step, 24 h time step and with 24 h time step adjusted by an empirical factor of 2.1

Figure 5.8 shows a sequence of daily cycles of wind speed, averaged over the region of the Volta Basin. A large diurnal variation is obvious. These characteristic diurnal cycles are representative for the respective seasons, what means the diurnal cycle of wind speed is temporally relatively stable. Because in mid-latitudes day-night differences are not always that strong (SCHULLA, 1997), and vary much more intra-seasonally, a partition of wind speed into day and night values was not yet implemented in WaSiM. Another reason for that was to restrict the number of parameters (SCHULLA, 1997).

In the present study it was found that the ratio of potential evaporation between the WAS3 run and the WAS24 run varies between 1.1 in the dry season and 2.4 in the rainy season, with an annual mean of 1.7. Thus, for the application within the Volta Basin, the Penman formula was multiplied by an empirical constant. From WAS24 runs with different empirical constants (1.7, 1.9 .2.1, 2.3, and 2.5), the best factor with respect to real evapotranspiration was chosen to be 2.1. It is necessarily larger than the annual mean value of 1.7, to account for the stronger and more important influence of potential evaporation on the resulting real evapotranspiration during the rainy season. The results of the original WAS24 run, the WAS3 run and the WAS24 run, that was calculated with the correction factor of 2.1 are illustrated in figure 5.9.

Daily Temperature Amplitude As already mentioned, the calculation of daily potential evapotranspiration is partitioned between a day and a night value, including a partitioning of the mean daily temperature amplitude into mean day temperature and mean night temperature. Within the equations of Penman and Monteith (equation 5.1 and 5.2), net incoming radiation is defined as

$$R_{N,day} = (1 - \alpha)RG - R_L \tag{5.3}$$

for the day and

$$R_{N,night} = -R_L \tag{5.4}$$

for the night, α being albedo, R_L outgoing long-wave radiation, and RG incoming short-wave global radiation. Long-wave outgoing radiation is thereby calculated as:

$$R_L = \Delta t \sigma T^4 (0.48 - 0.065\sqrt{e})(cr_0 + (1 - cr_0)SSD) \tag{5.5}$$

on the basis of mean day and night temperatures T_{day} and T_{night} respectively. The variable e is vapour pressure, and cr_0 is the diffuse part of incoming radiation. SSD is the relative daily sunshine duration and σ the Boltzmann-constant.

The following approach is used in WaSiM to calculate mean day and night temperatures from a mean daily temperature:

Mean day temperature and mean night temperature are defined as:

$$T_{day} = T_{24h} + c_{T,day}\Delta T \tag{5.6}$$

$$T_{night} = T_{24h} + c_{T,night}\Delta T \tag{5.7}$$

with $c_{T,day}$ and $c_{T,night}$ as the part of the monthly mean temperature amplitude ΔT, that is added to, or subtracted from the 24 hours' mean temperature T_{24h} to get T_{day} and T_{night}, and

$$c_{T,night} = 1 - c_{T,day} \tag{5.8}$$

For the calibration period only minimum and maximum daily temperatures were available from several stations. Therefore mean day and night temperatures could not be easily derived.

From field measurements that were performed within the GLOWA-Volta project, temperature data at 10 minute resolution was available for the year 2001 for three stations in Ghana (Ejura, Tamale and Navrongo). From these data, mean day and mean night temperatures were calculated under consideration of the length of the bright day.

Additionally, daily minimum and maximum temperatures were determined from the dataset. These data were then used to derive a simple relationship between monthly mean temperature amplitude

$$\Delta T_m = \overline{T_{day} - T_{night}} \tag{5.9}$$

and the respective monthly mean maximum temperature amplitude

$$\Delta T_{max,m} = \overline{T_{max} - T_{min}} \tag{5.10}$$

A mean factor

$$T_{fact,m} = \frac{\Delta T_m}{\Delta T_{max,m}} \tag{5.11}$$

was then calculated for each month.

The monthly mean $\Delta T_{max,m}$ values were calculated for all stations available over the calibration period and following equation 5.11, multiplied by the respective monthly factor to derive values of the mean daily temperature amplitude ΔT_m.

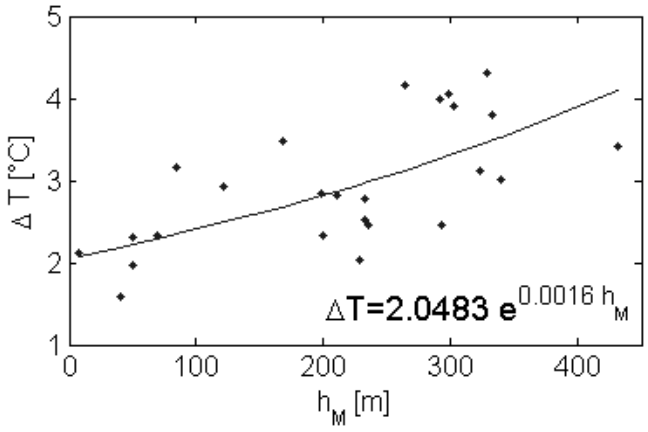

Figure 5.10: Empirical estimation of the parameter k_T

Then, ΔT_{sea} had to be defined for each month. This was done by plotting all available stations' ΔT_m values against height and extrapolating it to mean sea level using an exponential regression equation, in which the height dependence of the temperature amplitude is assumed to follow

$$\Delta T = \Delta T_{sea} e^{-\frac{h_M}{k_T}} SSD \tag{5.12}$$

with h_M the elevation of a respective station, and SSD the relative sunshine duration [-] (Schulla and Jasper, 2002).

The resulting mean monthly ΔT_{sea} values are:

Table 5.3: Determined monthly values of ΔT_{sea}

Jan	Feb	Mar	Apr	May	Jun	Jul	Aug	Sep	Oct	Nov	Dec
3.98	3.77	3.57	3.21	2.43	1.99	1.60	3.10	2.84	2.30	2.57	3.51

Subsequently the parameter k_T indicating the height dependence had to be determined. This was done as illustrated in figure 5.10. Here, the annual mean ΔT values of each station were plotted against height.

Equation 5.12 was again applied. On the basis of the exponent on the right hand side, the value for the parameter k_T was found to equal -625 m for the Volta Basin.

Sunshine Duration and Global Radiation In WaSiM, if daily values of sunshine duration are given as input but no global radiation measurements are available, global radiation (RG_{rel}) is calculated from sunshine duration according to the third order polinomial

$$RG_{rel} = cr_0 + cr_1 SSD + cr_2 SSD^2 + cr_3 SSD^3 \tag{5.13}$$

where SSD is the relative sunshine duration [-].

The polynomial coefficients cr_0 to cr_3 were calculated from observational data from 8 stations in Burkina Faso that delivered both, global radiation and sunshine duration data. The first coefficient cr_0 is the diffuse part of the incoming radiation and was set to 0.3 under consideration of the frequent impact of Saharan dust on radiation, especially in the dry

season. According to Schulla and Jasper (2002) the sum of all parameters should equal 1. Given these restrictions, the overdetermined system of linear equations was solved by the least squares method, incorporating a singular value decomposition (SVD) approach.

The resulting coefficients were:

cr_0	cr_1	cr_2	cr_3
0.3	0.43	6.96	-6.69

Anisotropy in Precipitation Interpolation In case IDW (Inverse Distance Weighting) is used for the interpolation of meteorological input data, a maximum search radius must be determined for stations to be interpolated.

Apart from the radius of influence an anisotropy, defined as the ratio of the main axis to the short axis of an ellipsoid may also be regarded. The main axis is defined in the North-South direction in WaSiM, so the anisotropy can be described as:

$$Aniso = \frac{\Delta lat}{\Delta lon} \tag{5.14}$$

with Δlat, the latitudinal increment (main axis) and Δlon, the longitudinal increment (short axis).

For application in the Volta Basin, the definition of an anisotrphy is useful because precipitation distribution shows a strong latitudinal dependence, as shown in section 2.1. This anisotropy can be a larger source of uncertainty if data is sparse, and consequently the distances between stations are large. If the influence of observational stations in the rainfall intense South reaches too far to the dry North serious inaccuracies might result. A factor of anisotropy was determined by considering the dependence of precipitation P on latitude $\frac{\Delta P}{\Delta lat}$ for all stations within a range of 1° longitude, and the dependence of precipitation P from longitude $\frac{\Delta P}{\Delta lon}$ for all stations within a range of 1° latitude. From these terms, the value for the anisotropy was calculated to be

$$Aniso = \frac{\overline{\frac{\Delta P}{\Delta lon}}}{\overline{\frac{\Delta P}{\Delta lat}}} \approx \frac{\Delta lat}{\Delta lon} = 0.35 \tag{5.15}$$

.

Soil and Groundwater Initialisation The initialisation of groundwater and soil storage within WaSiM was not possible due to the lack of observational data. Initialisation values were obtained from a prerun of the model. Figure 5.11 demonstrates the results of WaSiM runs for the simulation year 1968, for 4 iterations. It is apparent, that an entire annual cycle is needed to get a good estimate of groundwater and soil storage, and no major differences occur within the subsequent simulations. For the calibration runs, the prerun was 1.5 years, and for the climate simulations WaSiM was run for the entire time period twice, resulting in a prerun of 10 years.

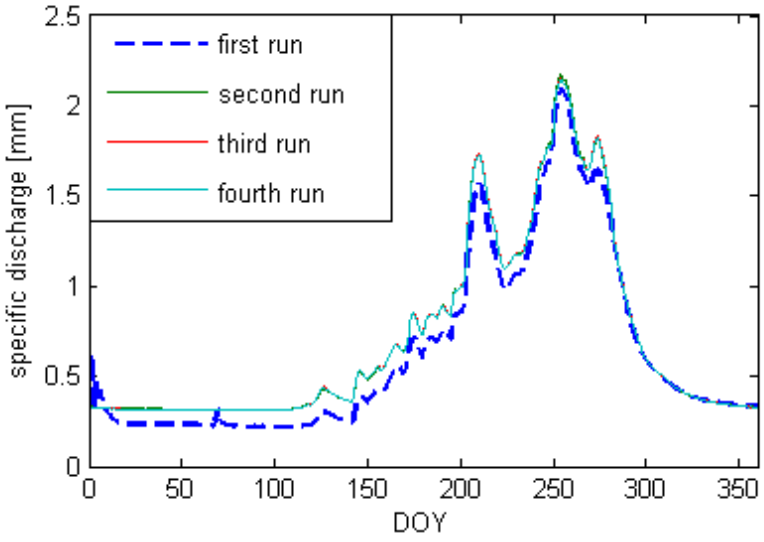

Figure 5.11: Iterative WaSiM runs: Simulated discharge [mm], demonstrating the filling of groundwater and soil moisture storage

5.2.2 Calibration

Parameter Estimation Techniques The more complex hydrological models get, the more sophisticated parameter estimation techniques are required. In the past it was believed, that one perfect parameter set exists, that can be determined by calibrating a hydrological model. According to Bastidas et al. (2002), this can only happen, if the model is assumed to be perfect and the measured data free of systematic biases. In general the optimal parameter space will always remain of finite size. Therefore several 'best-fit' parameter sets may exist, each of which leads to similar results. This is called the problem of 'equifinality' (Beven, 1989). The determination of the 'best fit', or at least one of the 'best fit' parameter sets of hydrological models can generally follow two different approaches, the trial-and-error approach and automatic calibration.

The trial-and-error approach encompasses all methods that manipulate parameter values manually and compare the results of model simulations to observations, directly or with reference to defined performance criteria and via iterative attempts try to identify the optimal parameter set.

For an automated optimization of the parameter estimation process, different methods of automatic parameter estimation have been tested for the use with hydrological models. The most prominent ones include the Shuffled Complex Evolution algorithm (SCE-UA), the Shuffled Complex Evolution Metropolis method (SCEM-UA), the Bayesian Recursive Estimation (BaRE), the multi-objective optimization algorithm MOCOM, the Generalized Likelihood Uncertainty Estimation (GLUE) method and the Markov Chain Monte Carlo (MCMC) method. A comprehensive overview of the parameter estimation problem can be found in Singh and Frevert (2002).

For this study the nonlinear Parameter ESTimation tool PEST was applied. PEST uses a gradient-based nonlinear parameter estimation algorithm following Gauss-Marquardt-Levenberg, which is a least squares fit method. This method requires fewer model runs

than any other parameter estimation method for nonlinear models. Another advantage of PEST is its easy implementation for different kinds of script-based models. An application of PEST for parameter estimation of WaSiM, is discussed in KUNSTMANN et al. (2005).

Calibration Period The calibration period for this study covers the years 1962-69, but daily observational discharge data was available only for the hydrological year 1968/69 (in West Africa: March 1968 - February 1969). 120 stations with rainfall data were available, 20 stations for temperature, 18 for relative humidity, 19 for wind velocity and 12 for sunshine duration.

Calibrated Parameters Subcatchment specific parameters were calibrated for all subcatchments that are named in figure 5.2. The parameter values for the additional subcatchments that border Lake Volta were estimated from similar, neighboring subcatchments. Furthermore some soil-type specific, hydrogeology and land-use specific parameters were calibrated. Within the calibration procedure WaSiM allows the input of observed runoff at the outlet of a subcatchment to prevent the transmission of errors from an upstream catchment to the downstream catchment, thus decoupling calibration of connected subcatchments. Without this feature, calibration of the downstream subcatchment would be rather arbitrary.

The following primary parameters were calibrated using an iterative process including manual parameter optimization of daily and monthly discharge values in combination with automatised parameter estimation with PEST:

Table 5.4: Most important calibrated parameters

K_{rec}	Recession constant for saturated hydraulic conductivity with depth
K_{sat}	Saturated hydraulic conductivity
K_D	Recession constant for direct runoff
K_I	Recession constant for interflow
d_r	Drainage density

The more physically determined parameters like K_{sat} and K_{rec} were optimized within a value range dependent on soil types, as is described in literature (MAIDMENT, 1993). Saturated hydraulic conductivity $K_{sat,z}$ at a particular depth z, is calculated with respect to the recession constant K_{rec} after:

$$K_{sat,z} = K_{sat} K_{rec}^{z} \tag{5.16}$$

The recession of direct runoff and interflow both follow a simple linear storage concept of the form

$$Q_t = Q_0 e^{-\frac{\Delta t}{K}} \tag{5.17}$$

with Q_t the discharge at time t, Q_0, the runoff at time $t = t_0$, the time step $\Delta t = t - t_0$ and K the recession constant (K_D for direct runoff and K_I for interflow).

The drainage density d_r is an empirical parameter that determines the magnitude of interflow Q_{ifl}, following

$$Q_{ifl} = K_{sat}(\Theta_m) \Delta z d_r tan\beta \tag{5.18}$$

with K_{sat}, the saturated hydraulic conductivity [m s^{-1}], the water content of the respective soil layer Θ_m [-], and the slope angle β.

Calibration on Basis of Daily Observational Data: 1968/69 Within this study a first calibration was performed by trial-and-error, manually manipulating the most important parameters and comparing the results with observed discharge. In addition to visual comparison of the runoff hydrographs, several performance criteria were utilized. These criteria are the Nash-Sutcliffe Efficiency NSE (Nash and Sutcliff, 1970) defined as:

$$NSE = 1 - \frac{\sum_i (x_{i,sim} - x_{i,obs})^2}{\sum_i (x_{i,obs} - \overline{x}_{obs})^2} \tag{5.19}$$

and the explained variance,

$$EV = 1 - \frac{\sum_i (x_{i,sim} - x_{i,obs} - \mu)^2}{\sum_i (x_{i,obs} - \overline{x}_{obs})^2} \tag{5.20}$$

where μ denotes the mean deviation of the modelled from the observed values, $x_{i,sim}$ the simulated discharge, and $x_{i,obs}$ the observed discharge at a specific time step i. $\overline{x}_{obs}$ is the mean observed discharge value over the entire simulation period. A perfect agreement of simulation and observation corresponds to a value of $NSE = 1$. In combination with NSE, the EV helps to identify systematic model biases. If runoff is overestimated in general, but the runoff response to rainfall is met sufficiently, a high EV value will be observed, even if the NSE is very low. The assumption underlying the application of NSE and EV is a normal distribution of both runoff data, the simulated and the observed. This leads to an overestimation of the impact of flood events, as it is generally not the case for runoff curves.

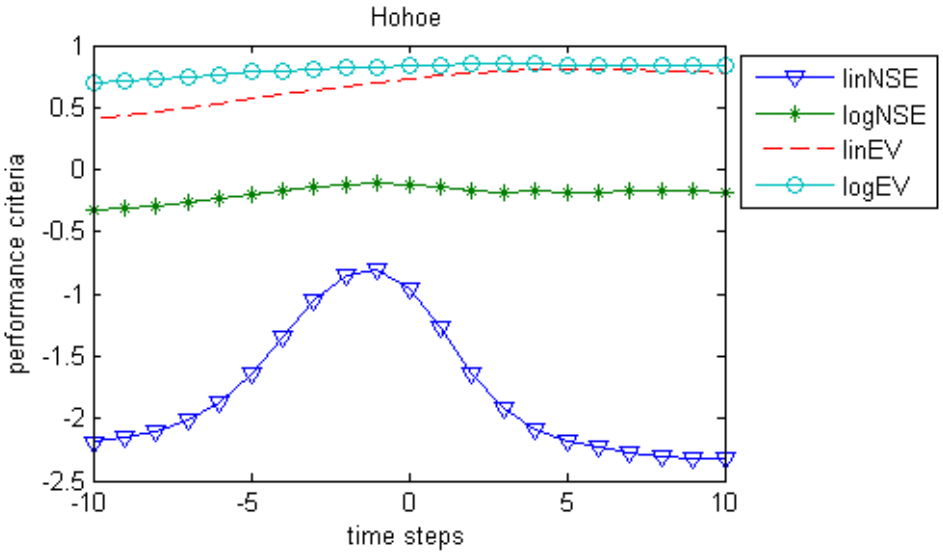

Figure 5.12: Performance criteria for $t_{sim} \pm 10\Delta t$ at gauge Hohoe

Therefore both performance criteria were additionally calculated for the logarithms of the runoff values, which gives more emphasis to average discharge heights than to extreme

events. Consequently the resulting four performance criteria are denoted as linear and logarithmic NSE ($linNSE$, $logNSE$), and linear and logarithmic EV ($linEV$, $logEV$). These criteria are calculated not only for the simulated runoff value at time t_{sim} with respect to the observational value at t_{obs}, but also for the simulated values shifted $t_{sim} \pm 10\Delta t$, with respect to t_{obs} to detect a possible temporal shift in the runoff curve. These four diagnostic statistics are demonstrated in figure 5.12 over the range of $t_{sim} \pm 10\Delta t$. As an example, for the gauge Hohoe, a systematic shift in the runoff amount can be detected clearly from $linEV > linNSE$ and $logEV > logNSE$, but also a temporal shift can be observed. This information in turn helps to set the focus in the calibration process.

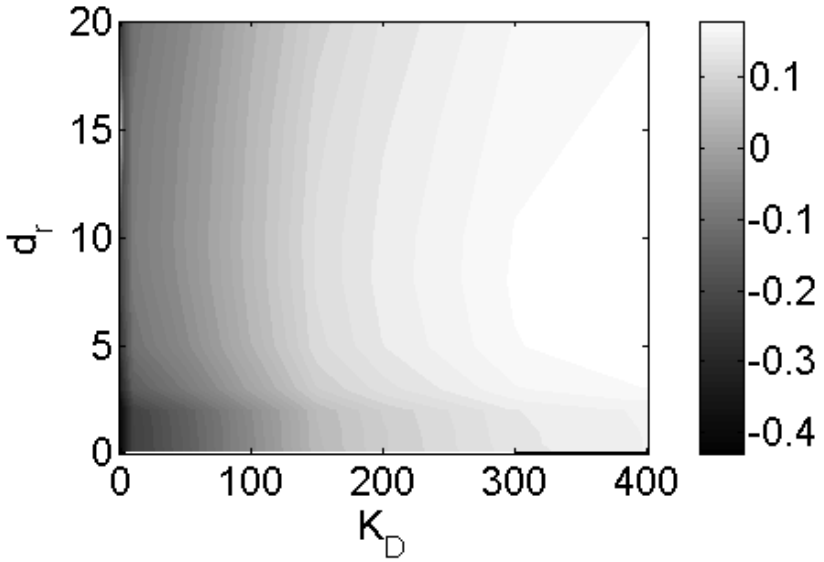

Figure 5.13: Optimization of NSE of discharge with respect to d_r and k_D

Another calibration tactics was to perform a large number of model simulations for the most sensitive parameters, while systematically varying them over a 2 dimensional parameter space, to find the best possible combination of parameters (figure 5.13 shows the NSE values for 100 model runs for variations of the parameters K_D and d_r). This procedure was also performed for K_D in combination with K_I and for K_{rec} in combination with d_r.

Automatic Parameter Estimation: PEST In a next phase of calibration, the model independent parameter estimation tool PEST (Doherty, 2002) was utilized. Within the scope of this study a shell scripting environment was developed to run a pseudo parallel version of PEST on multiple processors of a LINUX-cluster, using the PBS resource management system. PEST was only used for the fine tuning of the model parameters, as the optimization algorithm can easily be trapped in a local minimum. Numerous runs would be required to ensure that the global minimum was located if PEST was used without a first guess through a preliminary manual parameter estimation.

The resulting NSE values for the different gauges are summarized in table 5.5.

Calibration on Basis of Monthly Observational Data: 1962-68 Following HARTMANN and BÁRDOSSY (2005), the transferability of a hydrological model is strongly improved if the calibration is performed on a monthly or annual time scale in addition to the daily timescale. The influence of calibrating on different time scales was demonstrated for a conceptual hydrological model, based on the HBV (BERGSTROEM and FORSMAN, 1973) concept.

Transferability is of major importance for the simulation of future climate scenarios' impact on hydrology, when conditions will likely differ from those for which the model was calibrated. Therefore a similar approach was applied within the present study, extending the calibration period to the years 1962-69. Nevertheless, as daily data was scarce and only available for the hydrological year 1968/69. The model could only be calibrated on a monthly basis for the rest of the calibration period.

Therefore, a combined Nash-Sutcliffe criteria (NSM) from both, the daily calibration (NSM_{day}) and the monthly calibration (NSM_{month}) were calculated, and weighted with a factor α, dependent on the importance to be given to the respective criteria (equation 5.21). Within the present study more weight was assigned to the monthly calibration, because the hydrologic cycle and changes in hydrological variables are typically analyzed on a monthly basis. Therefore α was set to a value of 0.8.

$$NSM = 1 - \alpha \underbrace{\left(\frac{\sum_i (x_{i,sim}(d) - x_{i,obs}(d))^2}{\sum_i (x_{i,obs}(d) - \overline{x}_{obs}(m))^2}\right)}_{NSM_{day}} + (1-\alpha) \underbrace{\left(\frac{\sum_i (x_{i,sim}(m) - x_{i,obs}(m))^2}{\sum_i (x_{i,obs}(m) - \overline{x}_{obs}(m))^2}\right)}_{NSM_{month}} \quad (5.21)$$

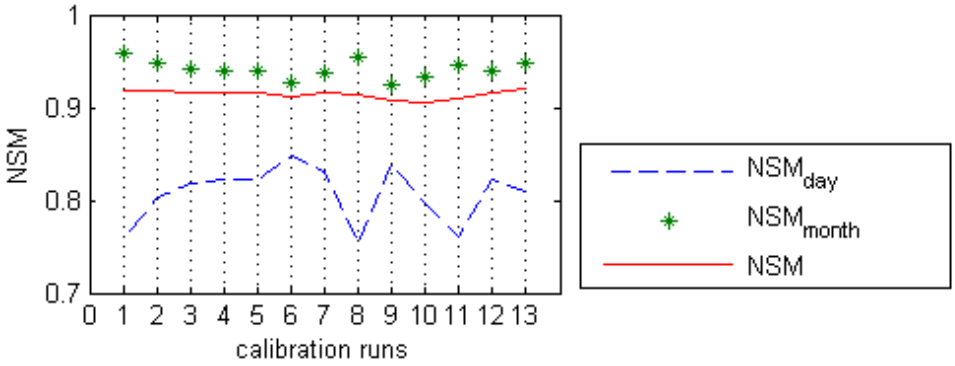

Figure 5.14: Optimization of NSM of discharge for daily, monthly and combined NSM criteria, Bamboi

An example of different calibration runs (denoted with numbers from 1 to 13) is demonstrated in figure 5.14. Here some contradictory behaviour of the runoff curve between monthly and daily calibration can be clearly observed. In the first instance this is due to

Table 5.5: Nash-Sutcliffe efficiencies for calibrated gauges

gauge	Bamboi	Boromo	Dapola	Ekumdipe	Hohoe	Nawuni	Pruso	Pwalugu	Saboba
NSE	0.95	0.31	0.82	-0.12	-0.23	0.84	-5.08	0.3	0.85

the high inter-annual discharge variability, so that a best fit for one year might not be a best fit for the other years. Furthermore, an improvement in the simulated monthly mean runoff does not necessarily mean an improvement of daily runoff, for example, when daily flood peaks are not captured, but low-flow periods indicate good fit.

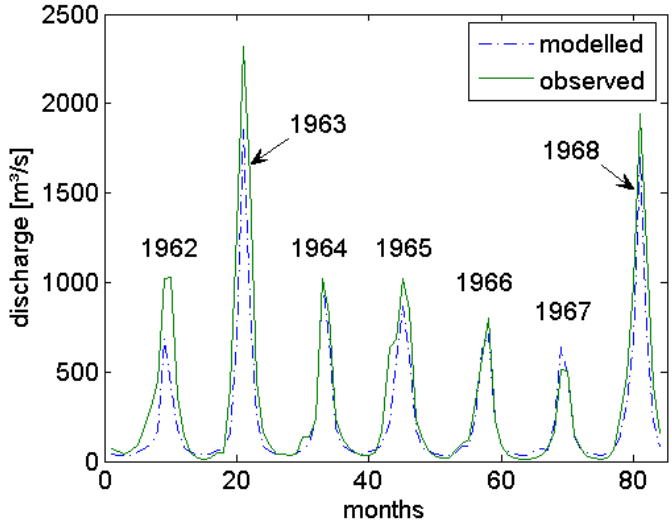

Figure 5.15: Monthly values of observed and simulated discharge [m^3s^{-1}] for the years 1962-1969, Bamboi

Figure 5.15 demonstrates a good performance for WaSiM over the period of monthly calibration for the gauge Bamboi, except for the year 1962.

Table 5.6: Nash-Sutcliffe efficiencies for monthly and daily calibration

gauge	Bamboi	Boromo	Dapola	Nawuni	Pwalugu
NSM_{day}	0.95	0.31	0.82	0.84	0.3
NSM_{month}	0.84	0.74	0.85	0.79	0.33

The NSM values for the calibrated gauges of the hydrological year 1968/69 and the monthly values for the time period of 1962-1969 are summarized in table 5.6.

5.2.3 Parameter Sensitivity

To obtain insight into the sensitivity of the hydrological simulations with respect to parameter choice, stochastical-hydrological simulations were performed. These simulations utilized the Monte-Carlo method and were performed using the modelling environment of Neumann (2005). The simulation of random numbers was done under the assumption of a normal distribution in a range of ±30% of the calibrated 'best fit' parameter value. The parameters that were tested for sensitivity are drainage density d_r, the recession constant for direct runoff K_D, and the recession constant for interflow K_I.

Results indicate a low sensitivity of runoff with respect to K_D and K_I. A strong influence of K_D on direct runoff is found only at the gauge Boromo. K_I is found to have a relatively

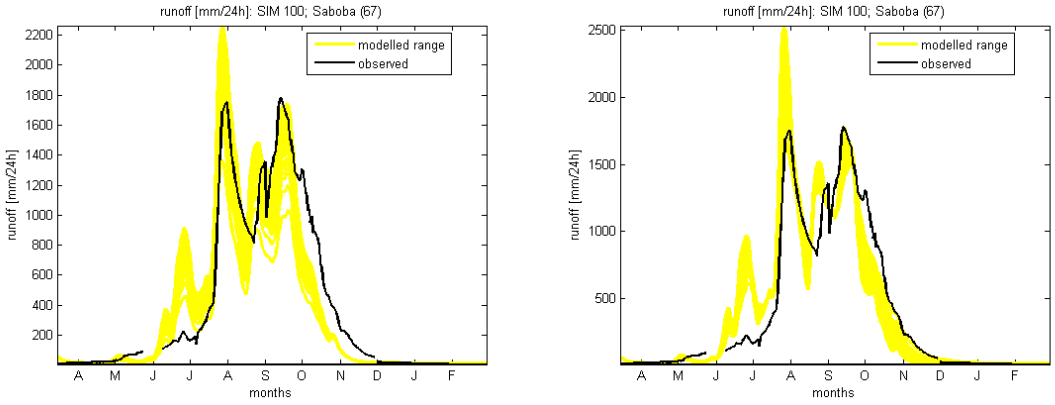

(a) d_r (b) K_I

Figure 5.16: Observed discharge and simulated discharge (using Monte-Carlo approach) within a range of 30% of the calibrated best fit value for the gauge Saboba, 100 simulations

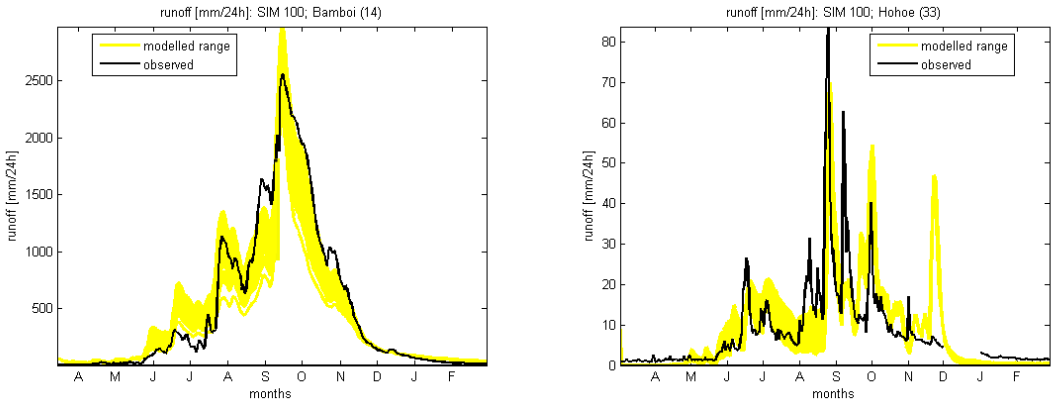

(a) Bamboi (b) Hohoe

Figure 5.17: Observed discharge and simulated discharge (using Monte Carlo approach) within a range of 30% of the calibrated best fit value, 100 simulations, sensitivity with respect to d_r

weak influence on interflow, and therefore on total runoff. For the gauge Saboba, total runoff shows a higher sensitivity to K_I (figure 5.16), than at the other gauges, due to the stronger contribution of interflow in this subcatchment.

Furthermore, runoff at Saboba shows an obvious time lag, with simulated runoff peaks occurring earlier than observed ones from the beginning of the rainy season to the month of September. At the conclusion of the rainy season in September/October, the simulated runoff peak is properly timed, but recession occurs too quickly. This indicates that either flow times are still too long, or the radius of influence for interpolation of precipitation is too large. Saboba is a large (55817 km^2) and data sparse subbasin and only 6 rainfall stations contribute to the interpolation result.

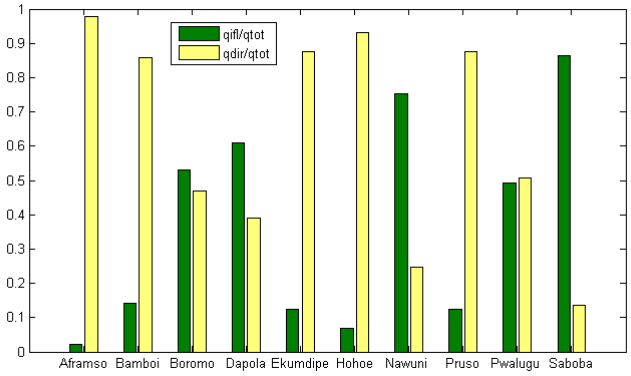

Figure 5.18: Direct runoff and interflow with respect to total runoff [-]

The parameter that evokes the strongest sensitivity on interflow is the drainage density d_r. The drainage density is an empirical parameter that determines the amount of interflow after equation 5.18. However a high sensitivity to d_r was also found for gauges that are not characterized by a large amount of runoff resulting from interflow (compare figure 5.18). The high sensitivity to d_r is illustrated in figure 5.17 for the gauges Bamboi and Hohoe.

5.3 Technical Realisation of the Simulations

The technical realization of the model runs (MM5 and WaSiM) was done on UNIX workstations, as well as on LINUX clusters. To simplify the continuous performance of the climate simulations, batch jobs on bash- and c-shell scripting basis were written and applied.

5.3.1 Computer Architecture

Three different computer architectures were available for the computation of the regional climate simulations and the hydrological simulations:

- Linux Cluster (CL1): 12 dual AMD Athlon MP nodes
- Linux Cluster (CL2): 48 dual Intel Xeon 36 Hz nodes

- Linux Cluster (CL3): 48 dual Intel Xeon EMT64 36 Hz nodes

  all three working with distributed memory.
  The parallelization of the nodes of the LINUX clusters is MPI standard (MPI-CH and LAM-MPI). For the distribution of the jobs to the cluster, the PBS resource management system is used.

- SGI: Origin 200 with 8 R12000 processors, working with shared memory

The regional climate simulations were performed in running parallel on either the SGI workstation or the LINUX-cluster (CL1-CL3). The hydrological simulations (WaSiM) were performed on a single processor on CL2-CL3, because WaSiM is not optimized for running in parallel mode. The pseudo-parallel version of the parameter estimation tool PEST (Doherty, 2002) used for model calibration was run on the LINUX-clusters as well. Within the scope of this research a batch system was developed for the use of MPI for the distribution of the single model runs, that are started synchronously by parallel PEST to the processors of the cluster.

5.3.2 Regional Climate Simulations

Preprocessing Figure 5.19 depicts the preprocessing chain of MM5 as it was used for the regional climate simulations, which differs slightly from the original MM5 procedure. The first step in the chain is the same as in a typical MM5 application.

The preprocessor TERRAIN fixes domain location and size, interpolates terrain elevation and land use onto the domain grid and generates LSM (*Land Surface Model*) related fields (e.g. soil type, vegetation fraction, deep soil temperature) (Dudhia et al., 2003). To read the input data, in this case ECHAM4 (GCM) output, the program ECGEN developed at IMK-IFU replaces the MM5 routine PREGRID. The remaining tools in the preprocessing chain are original MM5 modules. The further interpolation of the data to the MM5 grid is done with the preprocessing module REGRIDDER. Finally this data is interpolated to the MM5 layers with INTERPF. In addition to initial conditions (MMINPUT), INTERPF also calculates lower (LOWBDY) and lateral (BDYOUT) boundary fields. These three input files are calculated on a monthly basis and then serve as input for the first domain of the regional climate simulations. The preprocessor NESTDOWN interpolates the data from coarser grid output to input data on a finer grid and also produces the three afore mentioned MM5 input files. Within the regional climate simulations the outer boundary condition, as well as the initial condition for the smaller domains, were derived from the larger domain via NESTDOWN, but the lower boundary conditions were derived directly from the ECHAM4 output via the preprocessing chain (ECGEN - REGRIDDER - INTERPF) to get access to variable SST conditions. This option is not implemented within NESTDOWN.

MM5 modelling procedure Within MM5 a simulation year consists of 365 (366 for leap-years) days, as it originally is a meteorological model. The GCM simulation consists of 12 equal months of 30 days, resulting in a uniform length of 360 days for all years. To avoid losing a period of 5 (6) consecutive days in either month of the year, 5 (6) days were

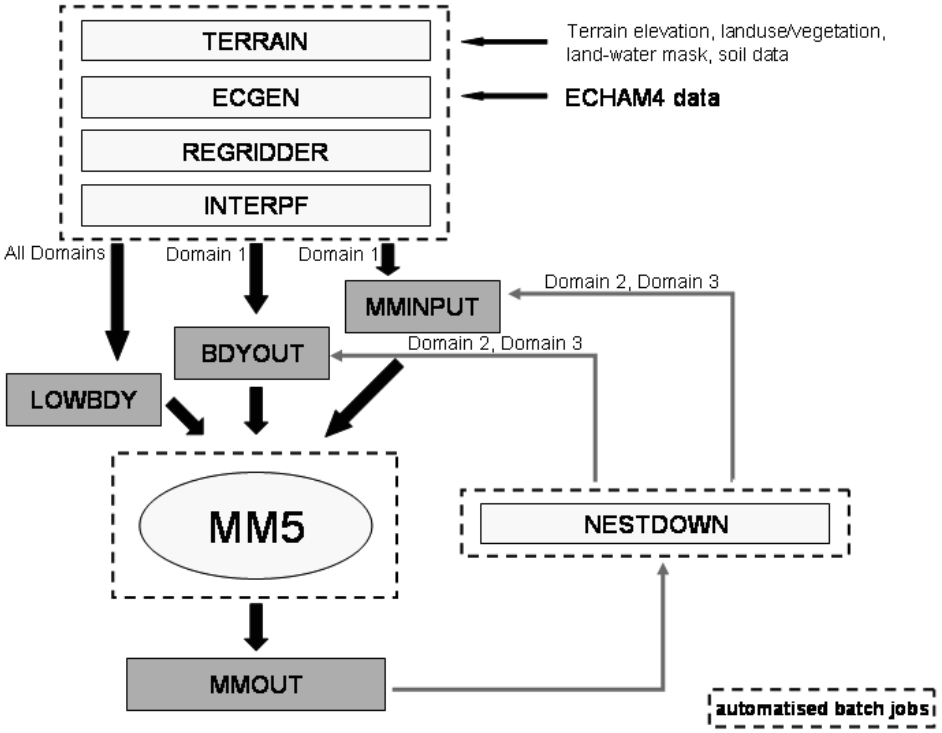

Figure 5.19: MM5: Preprocessing chain

cut out, uniformly distributed over the year. These days were December 31st, March 1st (for leap years), May 1st, July 1st, August 31st and October 31st.

The MM5 simulation was performed on a monthly basis. To simulate the most important variables continuously, these were passed from one month to the other within the model simulation via modification of the MMINPUT file (figure 5.20). The variables that were passed for all domain runs are soil moisture and soil temperature in all 4 soil layers. This is essential for long-term runs, to allow feedbacks between atmosphere and soil to develop. Additionally temperature, horizontal and vertical wind components, pressure tendency, ground temperature, mixing ratio, cloud water, rain water, cloud ice, and graupel were passed in the D1 run. For the two smaller domains a short spin up time for the atmospheric variables and a stronger dependence on the larger model domain dynamics can be assumed, which made it unnecessary to pass the atmospheric variables.

5.3.3 Model Coupling

The coupling of MM5 and WaSiM was accomplished using a one-way approach. The overview in figure 5.21 shows the schematic procedure of the model coupling.

The meteorological input data that are needed by WaSiM (compare section 4.3) are derived from MM5 model outputs.

An existing coupling routine already in use within a study on coupling regional climate simulations to hydrological simulations for the Ammer catchment by Schneider (2004) and Kunstmann et al. (2004) and for meteorology-hydrology simulations for the Mangfall catchment (Kunstmann and Stadler, 2003), both located in southern Germany, was

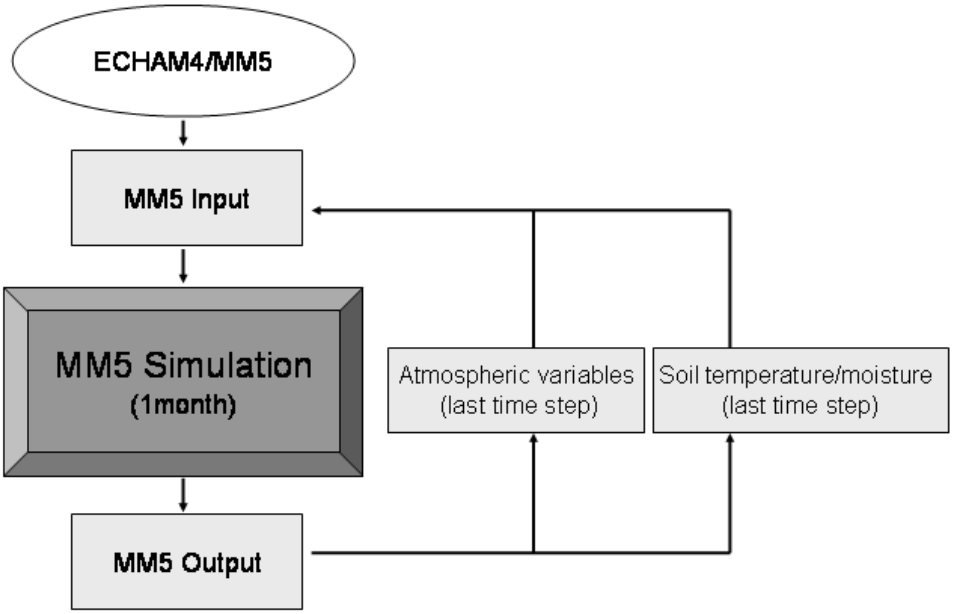

Figure 5.20: MM5: Modelling procedure for regional climate simulations

generalized to make it applicable to any domain size and resolution and any input and output time step.

Within the routine, convective and non-convective precipitation, 2 meters temperature and mixing ratio, horizontal wind components u and v in 10 meters and global radiation are extracted from the MM5 output files. From these variables, relative humidity and total precipitation are calculated and all variables are averaged (summed in the case of rainfall) over the number of MM5 output time steps that make up one WaSiM input timestep. Each grid point of the MM5 model grid represents one WaSiM input station. Within the processing of WaSiM these values are then interpolated to the WaSiM grid performing a bilinear interpolation.

In cases where both models, MM5 and WaSiM needed the same input data (e.g. land-use and soil properties) the same data sets were used for both, as far as possible. This included land-use parameters like LAI, albedo, etc., as well as soil characteristics like wilting point and saturated soil moisture content. These were taken from the MM5 land-use and soil table whenever possible. In case WaSiM needed supplementary parameter inputs, these were derived from the literature. Land-use data and classification (Vescovi, 2001) were also the same in WaSiM and MM5.

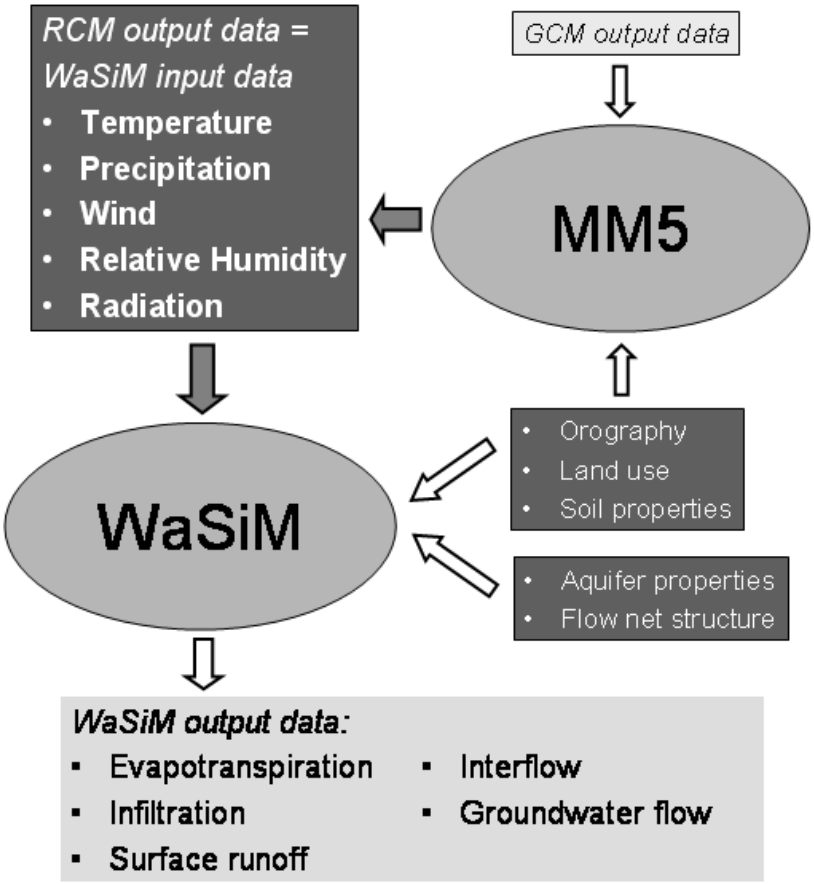

Figure 5.21: Coupling of MM5 and WaSiM

Chapter 6

Validation

Four steps of validation were performed. In a first step, the GCM output (1961-1990) is compared to gridded observational data (section 6.1). This is followed by an analysis of the reliability of the RCM downscaling reanalysis data in section 6.2. In section 6.3 the performance of the RCM for the 10 year time slice of the defined reference state climate (1991-2000) is compared to the GCM simulation of the same time episode, as well as to the longterm climate mean of the region. Finally discharge, simulated with the coupled hydrological-meteorological modelling system, is validated for a one-year simulation, also based on reanalysis input data (section 6.4).

6.1 ECHAM4 Output Analysis

The first question of interest concerning model reliability is whether recent climate can be simulated with sufficient accuracy by the GCM, because confidence in a models' performance in generating future climate scenario runs is higher when it is capable of reproducing observed present-day climate. Within this study, a comparison of the ECHAM4 simulation to present day climate conditions is particularly important, as the time span of the regional climate simulations (10 years) is too short to be considered as representative for the longterm mean present climate conditions. For the GCM comparison to reference state present-day climate, temperature and precipitation output fields of ECHAM4 (resolution: 2.81°) are compared to gridded observational data of the Climate Research Unit (CRU). This dataset includes all available observational data of the 20th century, interpolated to a regular grid (resolution: 0.5°, *www.cru.uea.ac.uk*).

Temperature A comparison of mean annual, monthly and seasonal temperature values as illustrated in figure 6.1 demonstrates good agreement between the results of ECHAM4 and CRU data. A slight overestimation of temperature can be observed in the ECHAM4 simulations for the Saharan region during the rainy season and during the dry season in southern West Africa.

Precipitation Figures 6.2 and 6.3 show precipitation output fields of ECHAM4, in comparison with CRU data for the time period of 1961-1990. Precipitation amounts, simulated with ECHAM4 are on first inspection comparable to the CRU data, but maximum values

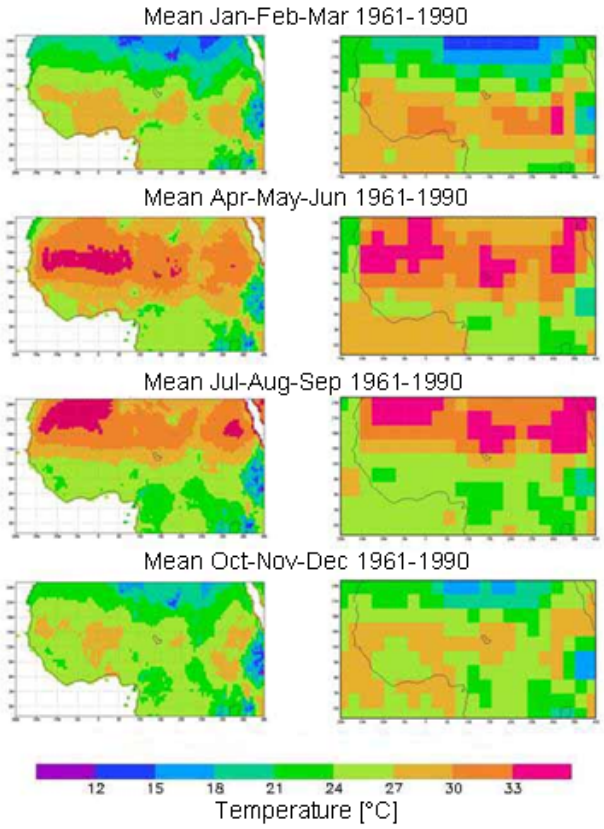

Figure 6.1: Comparison of CRU gridded observation (left) and ECHAM4 output (right), mean temperature [°C]

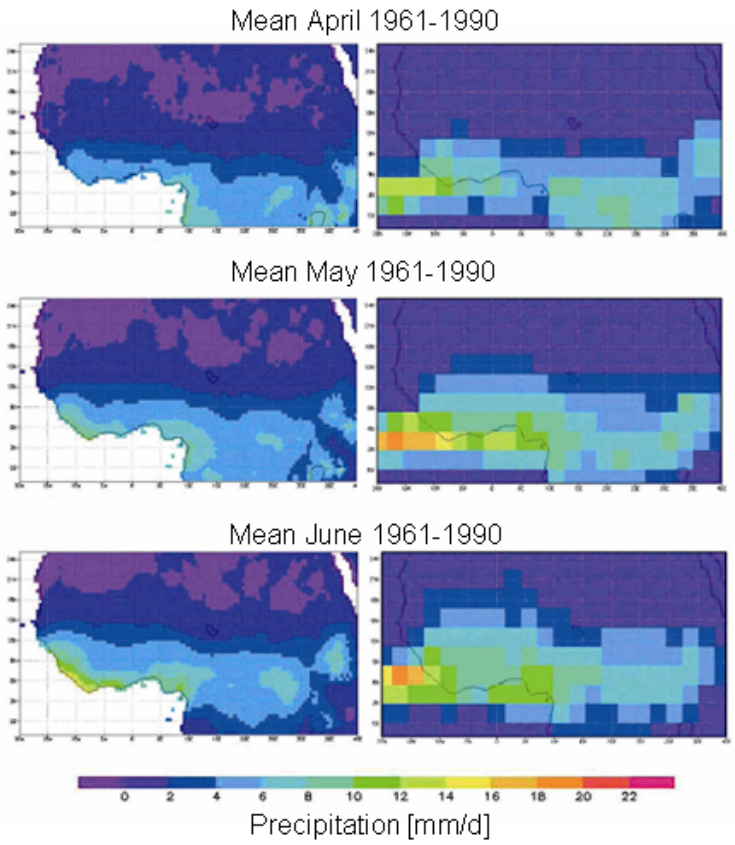

Figure 6.2: Comparison of CRU gridded observation (left) and ECHAM4 output (right), precipitation [mm d^{-1}], April-June

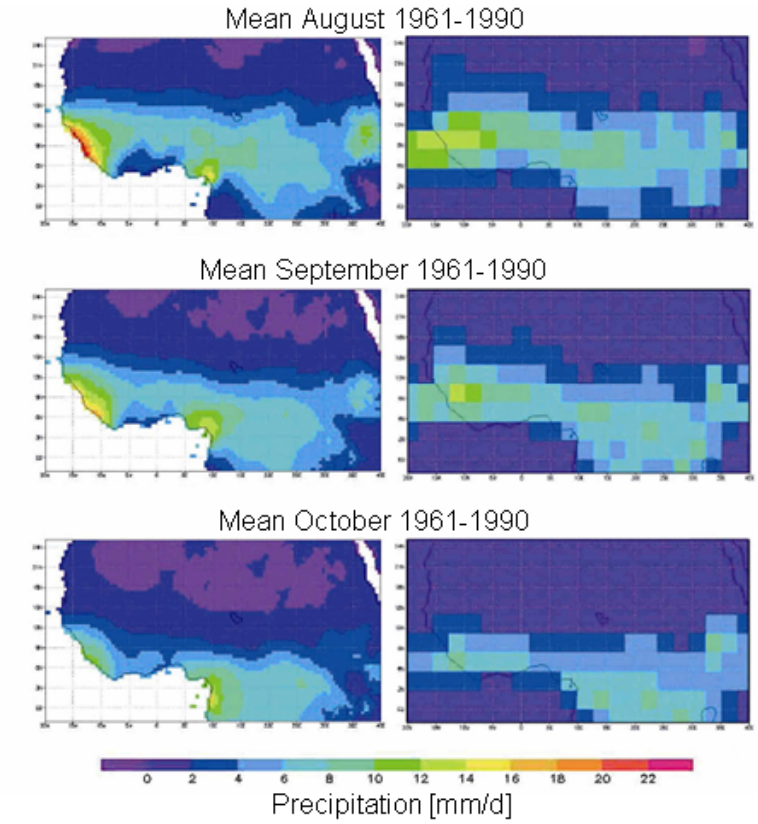

Figure 6.3: Comparison of CRU gridded observation (left) and ECHAM4 output (right), precipitation [mm d^{-1}], August-October

are in general too low. In addition precipitation zones, as well as the region of maximum rainfall, are shifted slightly to the North. The largest difference occurs in the northern Sahel and the Sahara, where precipitation zones widen and reach out some degrees further north than observed. VIZY and COOK (2002) stated that GCMs in general tend to produce wetter conditions than are observed over the Sahara during the rainy season, which also holds true for the prescribed ECHAM4 simulation. This was found to be connected with a wet bias over the Saharan boundary layer (VIZY and COOK, 2001), while the reasons are not yet understood.

Summary - GCM Output Analysis Temperature is represented with sufficient accuracy in the GCM simulation. On the basis of precipitation comparison it can be concluded that model physics shows some weaknesses in the GCM simulations. Nevertheless no quality assumption concerning the amount of precipitation can be transferred from the GCM to RCM as precipitation is connected with a high level of uncertainty and is strongly dependent on the parameterization scheme used within the simulations (which also differs between the regional and the global model) and the model resolution.

6.2 Downscaled Reanalysis

After evaluating the consistency of the GCM run with observed mean present climate conditions, the RCM performance under real meteorological conditions is tested. Therefore a set of short term (4 week) validation runs for the rainy season were performed to select the best possible set of parameterization schemes (KUNSTMANN and JUNG, 2003).

Two additional simulations of one year length each were performed within this study and validated. These simulations were run with the afore mentioned configuration, using NCEP (1997) and ECMWF (1968) (GIBSON et al., 1997) reanalysis data as inputs. Under the assumption that the reanalysis data used provides perfect boundary and initial conditions, the errors that are found can be attributed to the regional model. The validation included temperature and rainfall. These are the most important parameters for the present study and additional data for the Volta region is extraordinarily sparse.

The years that were chosen for the validation were an extremely wet year, 1968, and a comparably dry year, 1997, representative of the climate of the 1990s. These two years allowed an evaluation of MM5 for different climate conditions.

As a means of quantifying the modelling error, the RMSE (*Root Mean Square Error*), defined as:

$$RMSE = \sqrt{\frac{\sum_{i=1}^{N} (x_{mod} - x_{stat})^2}{N}} \tag{6.1}$$

was calculated for the modelled monthly mean value (in case of temperature) or the monthly sum (in case of precipitation) at the nearest grid-point x_{mod}, compared to the respective station value x_{stat}. N denotes the number of x_{mod} and x_{stat}, respectively.

In case of precipitation a normalized RMSE

$$RMSE_{norm} = \frac{\sqrt{\frac{\sum_{i=1}^{N} (x_{mod} - x_{stat})^2}{N}}}{\overline{x_{stat}}} \tag{6.2}$$

was defined, to account for the strong latitudinal and inter-annual dependence of absolute rainfall amounts in West Africa.

Temperature Considering the scatterplot with observed monthly mean temperatures, plotted against modelled values at the station's nearest grid point (figure 6.4) highlights a good agreement, with a uniform scattering around the regression line that almost coincides with the line of perfect agreement. Though the scattering around the mean value is not

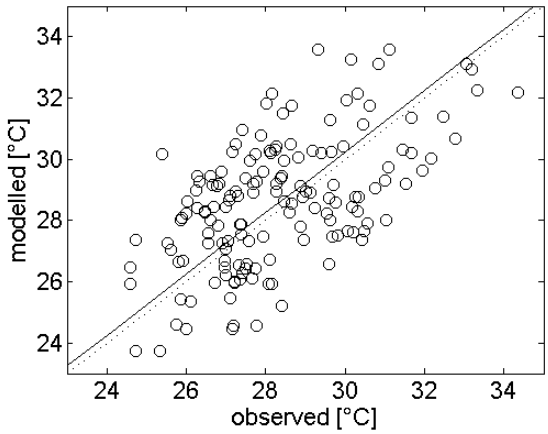

Figure 6.4: Temperature [°C] modelled vs. observed, all months and stations, 1997 (modelled: nearest gridpoint to station value), dashed line: Linear regression, dotted line: Line of perfect agreement

negligible, the linear regression intercept reveals just a small overestimation of temperature.

In Figure 6.5 the RMSE was calculated for all available stations over $N = 12$ months each, and plotted against latitude, as well as longitude. No strong dependence on longitude could be observed, but a latitudinal dependence of the RMSE was found. Therefore zonal mean values of the bias $b = x_{mod} - x_{stat}$ for stations belonging to each zone of 1° latitude were calculated for each month and for all zones between 5°N and 14°N and subsequently plotted against latitude. This is demonstrated in figure 6.6.

For the dry season, an underestimation of temperature is evident for almost all latitudes. Along the coast, this underestimation persists over the entire year. The more Northerly the stations are situated, the stronger is the annual cycle of the bias. A negative bias is observed in the dry season and a positive bias in the rainy season. This positive bias is also stronger the further North the station is situated. It even reaches a value of 2°C in approximately 13°N in September. The underestimation of temperature along the coast is most likely due to an underestimation of sea surface temperatures in the Gulf of Guinea. For an explanation of the overestimation in the Sahel region a further examination is needed on the reliability of simulated rainfall. Temperature always shows a strong connection between soil moisture and the subsequent partitioning between latent and sensible heat fluxes. Because soil moisture is strongly dependent on the rainfall amounts of the past, a bias in precipitation can have a strong influence on near surface air temperature and lead to a subsequent bias in temperature. In a time series analysis for different regional climate models Evans et al. (2005) demonstrated that MM5/OSU-LSM, as in the present study,

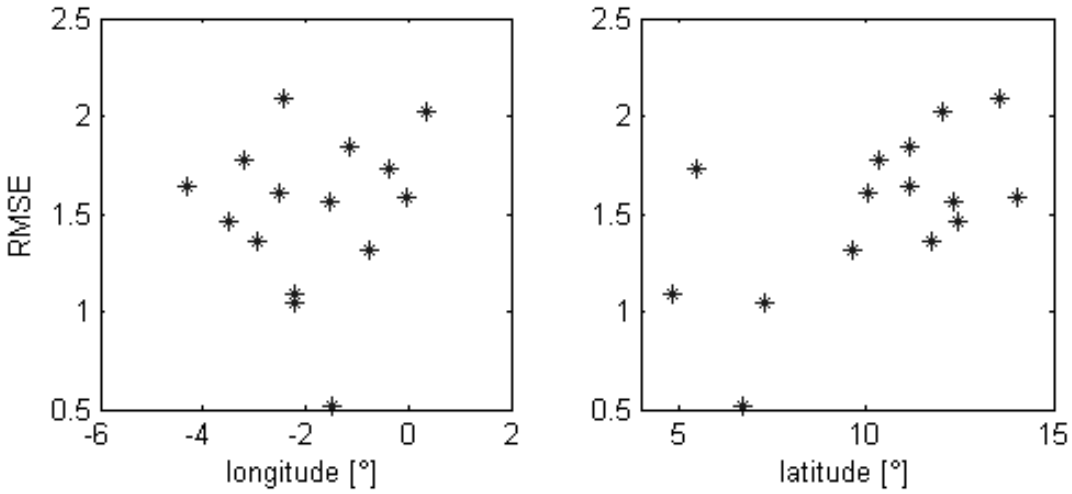

Figure 6.5: RMSE of mean monthly temperatures, 1997, left: stations plotted against longitude, right: stations plotted against latitude

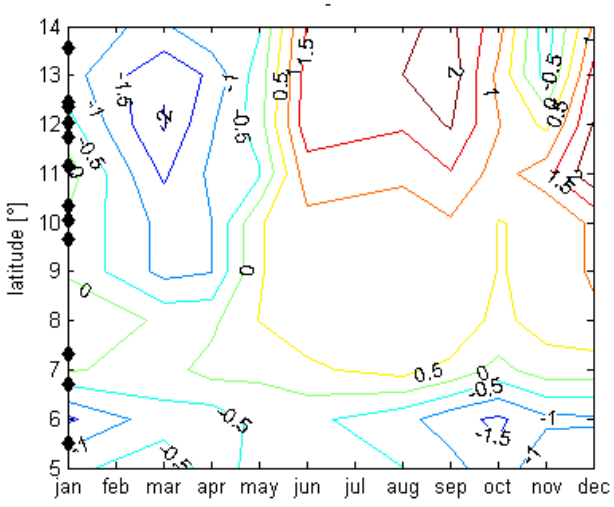

Figure 6.6: Temperature bias (modelled - observed) [°C] with respect to latitude and month, 1997, black rhombs indicate the latitudinal station location

showed a positive bias. Their findings indicated that this temperature bias was due to an underestimation of soil moisture. The $RMSE$ for temperature over all stations and months is 1.5 °C.

Precipitation Figure 6.7 shows a direct comparison of precipitation amounts between monthly mean station values and simulated values at the nearest grid point. This gives clear evidence of a much weaker coherence in modelled and observed rainfall values than for temperature (figure 6.4). For precipitation 108 observational stations were available for the year 1968, whereas for 1997 only data from 59 stations could be used.

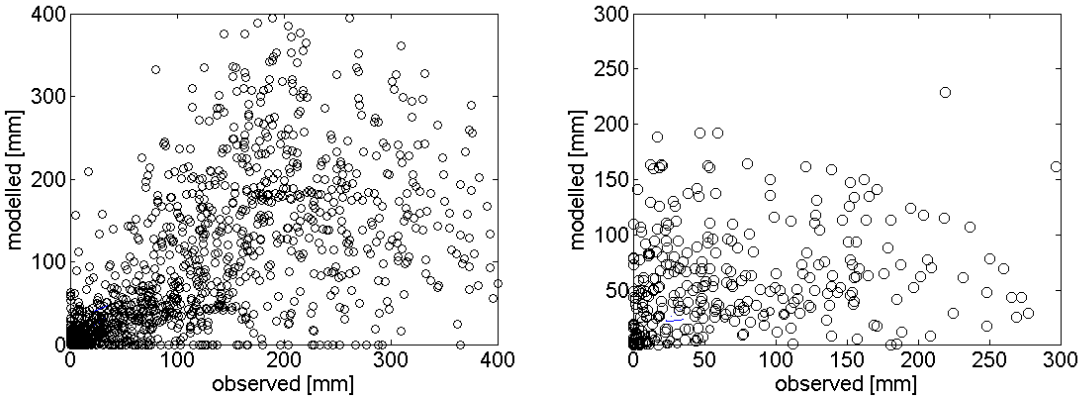

(a) 1968 (b) 1997

Figure 6.7: Precipitation [mm], modelled vs. observed, all months and stations (modelled: nearest gridpoint to station value)

Figure 6.8 shows neither a longitudinal nor a latitudinal dependence of the $RMSE_{norm}$ for precipitation. For 1997 the biases in the North are quite weak, but large underestimations in absolute rainfall amounts, especially in the early rainy season can be found along the coast.

Comparing the precipitation bias of both years 1997 and 1968 highlights the major differences between the wet (1968) and the dry year (1997) (figures 6.9 and 6.10). In 1968 a negative bias is found over almost the entire area and the entire annual cycle.

Even if the absolute bias is large in 1968, exceeding 200 mm in June and August near the coast, the relative bias is small compared to 1997, because annual rainfall amounts in the southernmost regions reach 3000 mm. In 1997 the absolute bias even exceeds 250 mm in June, but the annual sum only exceeds 2000 mm along the coast. In the northern regions of D3, 1997 yields better results, with only small overestimations of 50 mm in the very North in April and June. For 1968, an underestimation can also be observed in the northern and central parts of the basin, but compared to rainfall amounts in that year the deficit is still small. What both years have in common is the strong bias in rainfall along the coast.

The $RMSE_{norm}$ and the $RMSE$ values for precipitation, for the nearest and, to account for the spatially highly heterogeneous nature of precipitation also for the mean over the four nearest gridpoints are summarized in table 6.1. This indicates a relatively high RMSE of precipitation of over 83% for both years.

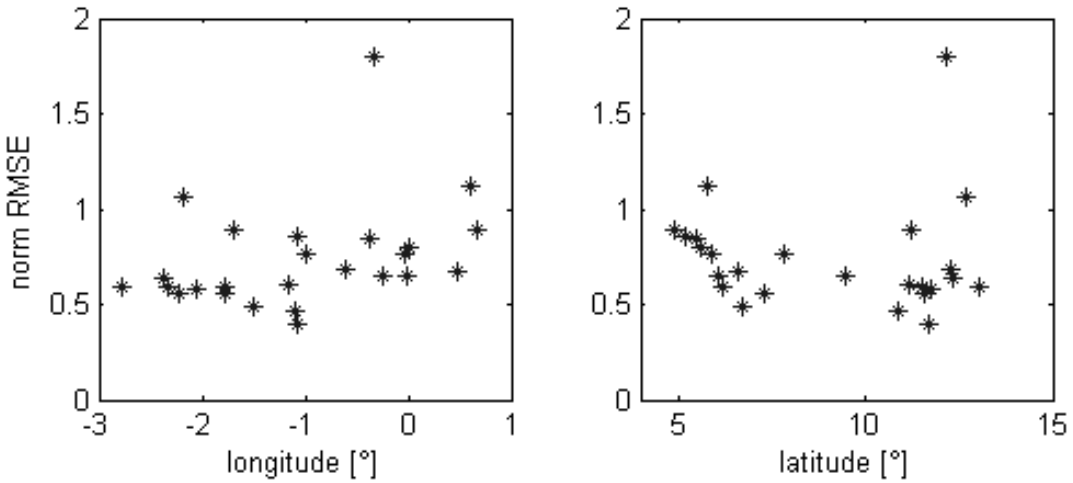

Figure 6.8: Normalized RMSE of monthly precipitation, 1997, left: stations plotted against longitude, right: stations plotted against latitude

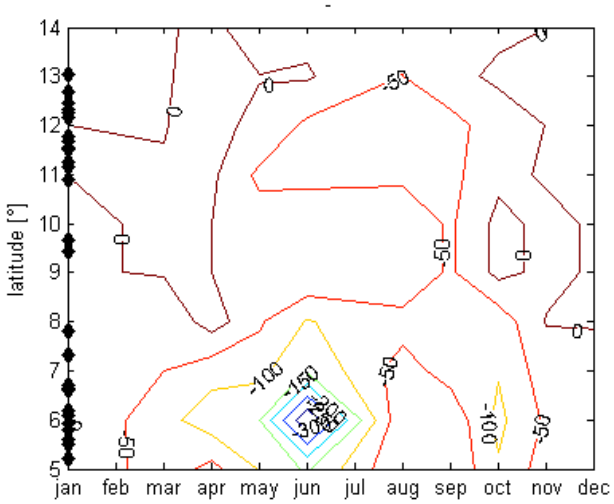

Figure 6.9: Precipitation bias (modelled - observed) [mm] with respect to latitude and month, 1997, black rhombs indicate the latitudinal station location

Table 6.1: $RMSE$ and $RMSE_{norm}$ for precipitation

	1968		1997	
	1 GP	4 GP	1 GP	4 GP
$RMSE$ [mm]	98.67	106.11	11.29	106.86
$RMSE_{norm}$ [-]	0.84	0.8992	1.22	1.24

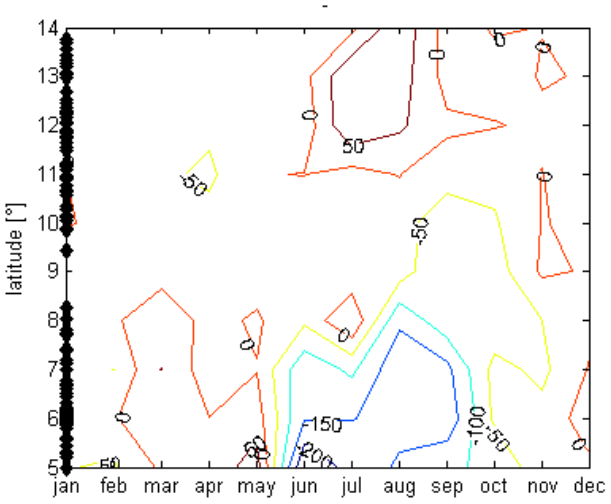

Figure 6.10: Precipitation bias (modelled - observed) [mm] with respect to latitude and month, 1968, black rhombs indicate the latitudinal station location

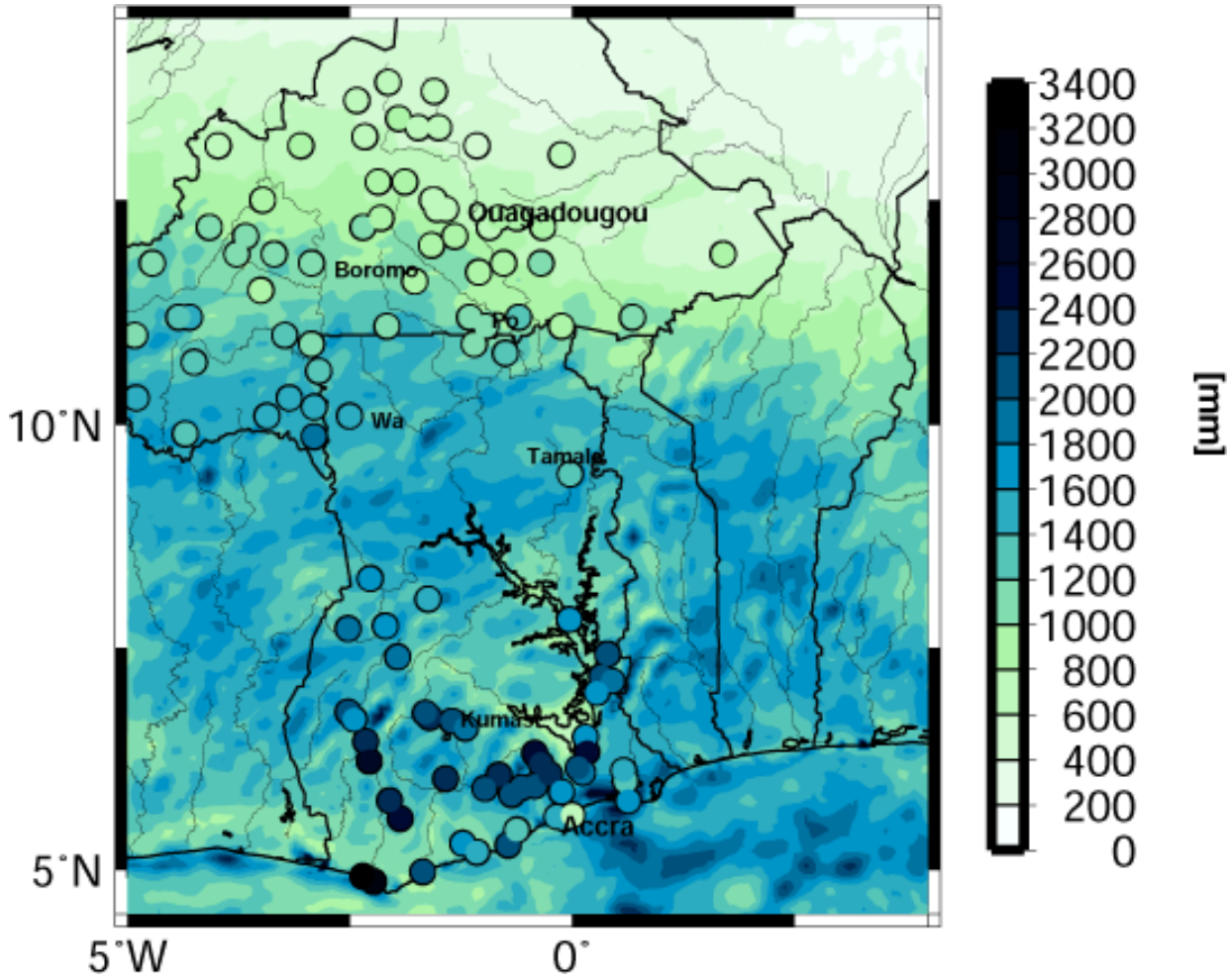

Figure 6.11: Simulated annual rainfall [mm] and observations [mm] (indicated by the colour within the circles), 1968

Pielke (1984) has already stated that there is a major problem in point-to-point validation of rainfall, as it can lead to poor verification results even when the magnitude of the simulated pattern was almost exact. Therefore the underestimation of rainfall amounts as evaluated with the $RMSE_{norm}$ and the absolute and relative error values are at least except of the coastal region to some degree due to the high probability of a spatial and/or temporal displacement in rainfall predictions.

The validation results are strongly limited by the general low predictability of precipitation, especially in case of convective precipitation which accounts for around 80% of annual precipitation amounts in the Volta Basin (section 2.1). To demonstrate this, figure 6.11 shows the modelled annual precipitation distribution for the year 1968 and all available station values, where the colour in the circles indicates the annual precipitation amount at the respective station. The underestimation of coastal rainfall is obvious, whereas in the northern part of the basin modelled annual rainfall amounts lie within the observed range, even if the exact location is not always matched.

Summary - Validation of Downscaled Reanalysis A similar pattern of bias, spatially as well as temporally, was found for both years. This indicates a systematic error, because strong differences in the rainfall regimes of both years are apparent. A strong positive bias in temperature can be found in the North of the Volta Basin during the rainy season. Over the entire annual cycle a rainfall deficit is observed and temperature shows a permanent negative bias along the coast. The main error is a significant underestimation of rainfall along the coast in the rainy season of about 50-200 mm per month, which can not be explained so far. The reason for the temperature, as well as for the precipitation bias along the coast might lie in a negative bias of SST. This can lead to lower air temperatures along the coast on one hand, and to less strong convective activity (due to a weaker sensible heat flux) accompanied with lower rainfall amounts on the other hand. Nevertheless, also model deficits of the parameterization schemes (e.g. convective and boundary layer parameterization) within MM5 cannot be excluded. Furthermore, the regions of low precipitation denoted as Togo Gap and Dahomey Gap can not be re-created from the model runs. The reasons for this probably include the low resolved SST field in the reanalysis data (2.5°). No coastal Kelvin waves, nor a coastal upwelling due to Ekman transport can be expected in this data (compare section 2.1). It can be concluded, that rainfall simulations are sufficiently accurate within the Volta Basin.

6.3 Downscaled Global Climate Simulation

6.3.1 Comparison to GCM Simulation Outputs

In addition to the evaluation of the GCM output with respect to observations for a longer (30 years) time slice (section 6.1), the GCM simulated 10 year time slice (1991-2000) was compared to the respective MM5 simulation (D1). Because regional climate simulations can be understood as a magnifying-glass for the GCM signal, the results for MM5 simulated atmospheric variables should be in the range of the GCM simulations, but revealing smaller scale patterns when higher resolution land use, topography and land - sea mask effects are included. Given the amount of precipitation this need not be true, as it is highly dependent on the convective parameterization scheme used. Nevertheless the distribution of precipitation should be similar, as it is, to a major extent, determined by large-scale dynamics and moisture transport.

Temperature Despite the fact that the spatial configuration of both runs is similar, temperature shows a pronounced positive deviation in the MM5 simulation with respect to the ECHAM4 run (figure 6.12). The region that shows the strongest deviation is the Saharan region. But northern Ghana and south-eastern Nigeria also show pronounced positive deviations. This is most likely due to a lack of soil moisture as a consequence of the negative bias in precipitation (following paragraph). For the Nigerian region a positive deviation is found on the north-western side of the mountains along the border to Cameroon, and an underestimation of temperature can be found on the other side of the mountains. This is linked to differences in rainfall amounts on either side of the mountains, and is a good example for the finer structure that is introduced in the meteorological variables through higher resolution topography information.

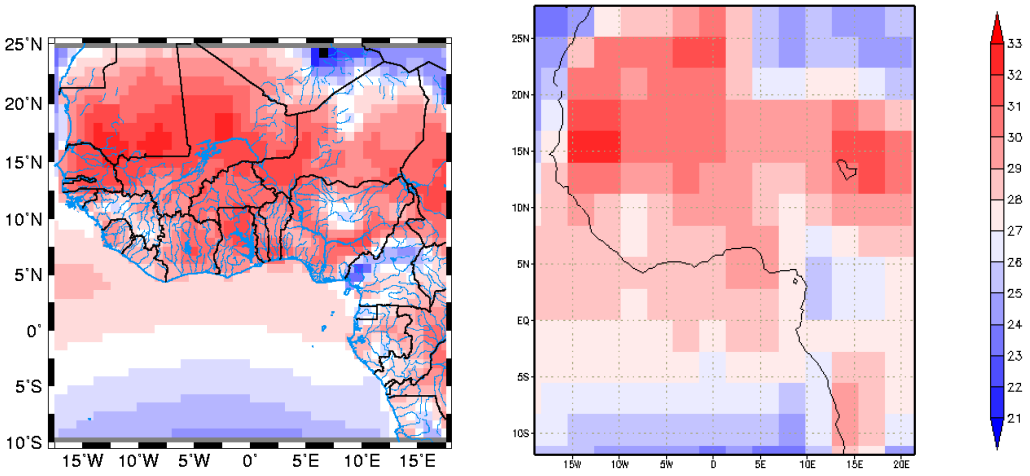

(a) MM5 (b) ECHAM4

Figure 6.12: Mean annual temperature [°C] (1991-2000)

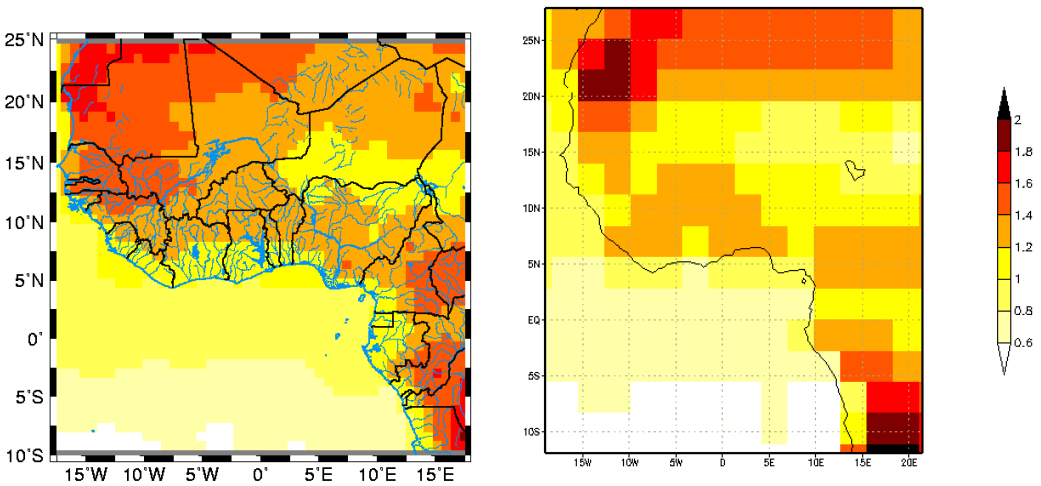

(a) MM5 (b) ECHAM4

Figure 6.13: Mean annual temperature change (2030-2039 vs. 1991-2000) [°C]

Temperature change shown in figure 6.13, shows a very good agreement between GCM and RCM simulations. The largest differences lie in a 0.2°C higher increase signal over the western Sahel and the central Sahara.

Precipitation Precipitation, as illustrated in figures 6.14, is lower in the MM5 simulations for Domain 1 than in the ECHAM simulations. Nevertheless an improvement in the

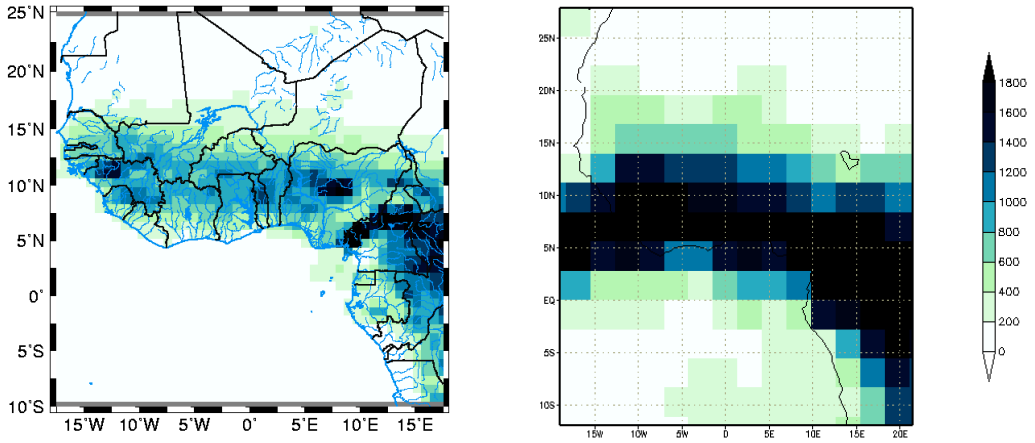

(a) MM5 (81 km resolution) (b) ECHAM4 (2.5° resolution)

Figure 6.14: Mean annual precipitation [mm] (1991-2000)

spatial representation of rainfall can be observed. One example is found in the mountain range along the border of Cameroon and Nigeria, where the highest peak reaches 4380 m. Here, the maximum in observed rainfall is also found. This rainfall maximum is not represented within the global simulation at coarse resolution, but appears in the regional simulations of D1.

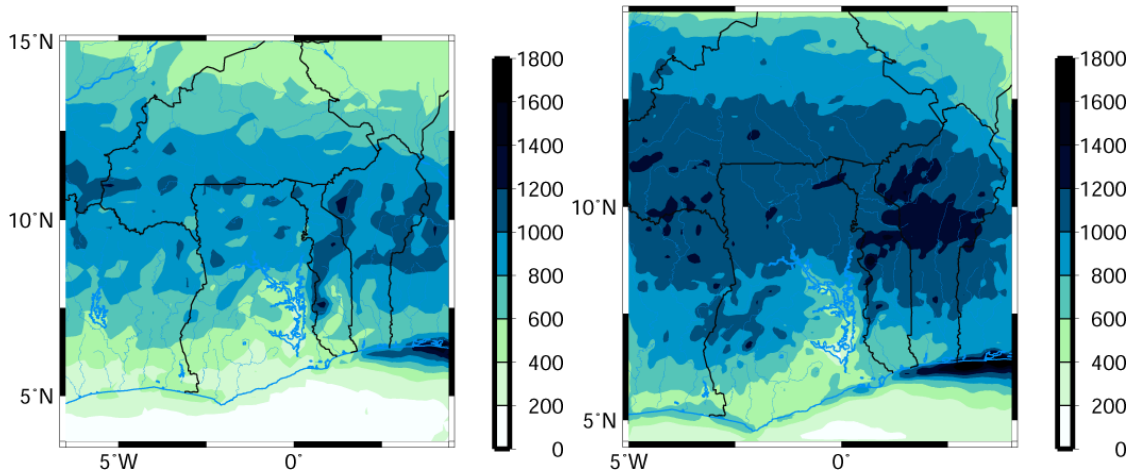

(a) MM5 (27 km resolution) (b) MM5 (9 km resolution)

Figure 6.15: Mean annual precipitation [mm], MM5 (RCM)

A comparison of the three MM5 model domains (figure 6.14, left: D1 and figure 6.15: D2 and D3) demonstrates the improvement in rainfall amounts that accompany an increase in model resolution. The cause might be that the convective parameterization scheme works better at the finer resolution. It is also likely that the higher resolution in topography contributes to improved results, such as the increase in precipitation amounts in the mountainous region of central Benin. Nevertheless the precipitation change signal within the

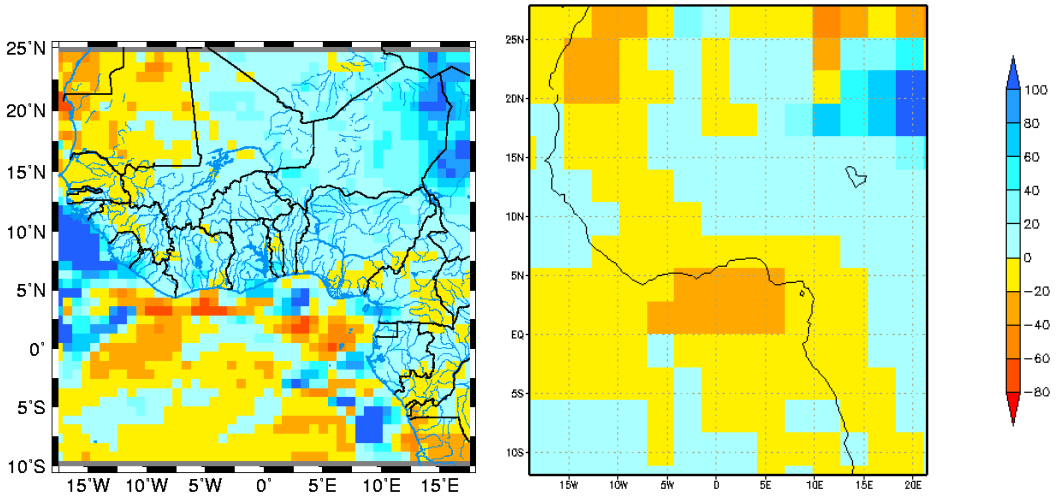

(a) MM5 (b) ECHAM4

Figure 6.16: Mean annual precipitation change [%] (2030-2039 vs. 1991-2000)

simulations is similar (figure 6.16). There is a precipitation increase over most of the continental part of West Africa, with a maximum along the mountain range along the border between Nigeria and Cameroon. The strongest precipitation reduction signal in both simulations can be found in the Gulf of Guinea region and along the southern coastline, as well as in the region of Senegal, Mauritania and West Sahara. A difference occurs along the southern West African coastline; where there is a precipitation decrease simulated in the ECHAM4 run, but an increase with MM5.

6.3.2 Comparison to Observed Climate

Because precipitation in both GCM and RCM simulations is strongly dependent on the sub-gridscale parameterization scheme used, it is also necessary to compare the downscaled precipitation to observed data. However single years of a climate simulation can not be compared to single years of observation. Within this study, a comparison of the 10-year model time slice to a time slice of the same length of observed climate is not feasible, especially in West Africa, given the regions' strong decadal variability. Acknowledging that averaging over a longer time span removes part of the low frequency variability, the comparison was performed with respect to long term climate mean conditions. Therefore all observed time series of 30 years that were available for Ghana and Burkina Faso were spatially interpolated to the model grid of D3[1] and compared to the MM5 (downscaled ECHAM4) climate run for 1991-2000. Even though the informative value is smaller because of the short time slice, the comparison is justified to achieve an approximation of model performance.

Liu and Moncrieff (2004) demonstrated that the position of the Inter Tropical Discontinuity (ITD) is dependent on the convective parameterization scheme used in a GCM and therefore it can be expected that the position of the ITD is modified within the RCM simulation. For this reason, the same argumentation as for rainfall is addressed for the ITD position. Subsequently the position of the ITD is also compared between RCM simulations and long term means later in this chapter.

Precipitation The spatial representation of annual rainfall deviations (modelled - observed) (figure 6.17), demonstrates a strong underestimation of rainfall along the coast, (up to 80%) similar to what was found for the MM5 reanalysis runs, but only a small overestimation of rainfall in the Sahel (10-30%), which is most likely introduced to the regional climate simulations through the wet bias of ECHAM4, described in section 6.1.

The spatially and monthly averaged values of precipitation for the long term mean of observed climate and the MM5 run in figure 6.18 indicate reasonable accuracy in the representation of the annual cycle of precipitation, and in the spatial means of precipitation sums.

Inter Tropical Discontinuity (ITD) One very important characteristic that influences the climate in West Africa is the annual movement of the ITD. The meridional wind direction was chosen as a measure for the position of the ITD in the MM5 simulations, because along the ITD (as it is a convergence zone) the meridional wind component changes its algebraic sign. Figure 6.19 shows the months January, June and September to provide insight into the mean displacement of the ITD for the ECHAM4-MM5 simulated years 1991-2000 and the long term mean position for the respective months (Leroux, 2001).

The southernmost position of the ITD within the year (December/January) is captured well. The movement of the ITD to the North appears to happen too rapidly, showing a larger deviation of the simulated from the climate mean position from April to June. In the simulations, it already reaches its northernmost position in June, whereas for the long term

[1]Spatially interpolated station data: the data consists of 95 stations' time series with a length of 30 years. The spatial interpolation was done with a combination of inverse distance weighting (IDW) and multiple linear regression (MLR), weighting IDW with 60%. For the MLR, latitude, longitude, height, slope, curvature and aspect were considered

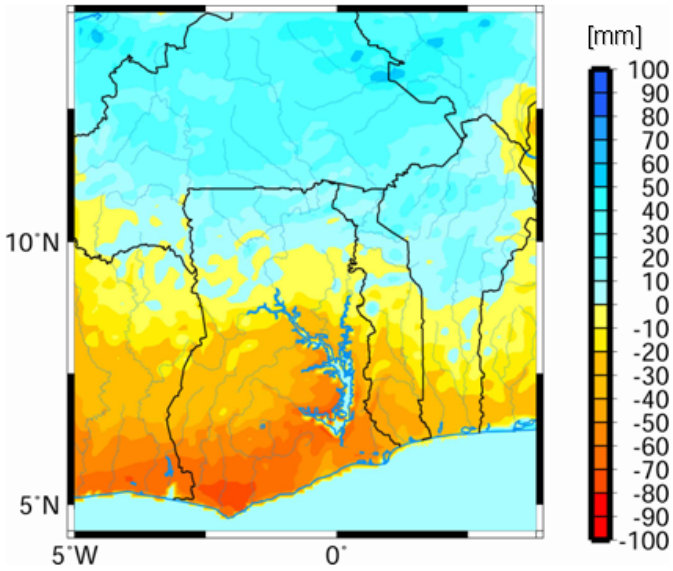

Figure 6.17: Simulated mean annual precipitation (1991-2000) versus observed long term mean [mm], D3

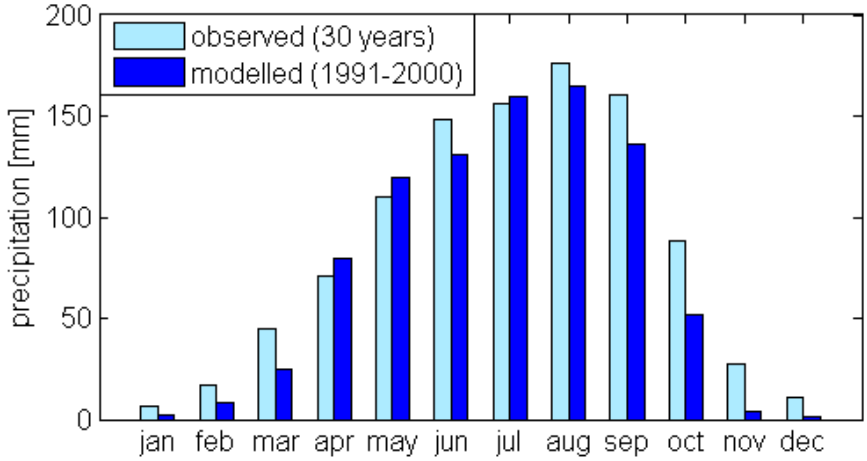

Figure 6.18: Spatially averaged, simulated mean monthly precipitation (1991-2000) versus observed long term mean [mm], D3 land area

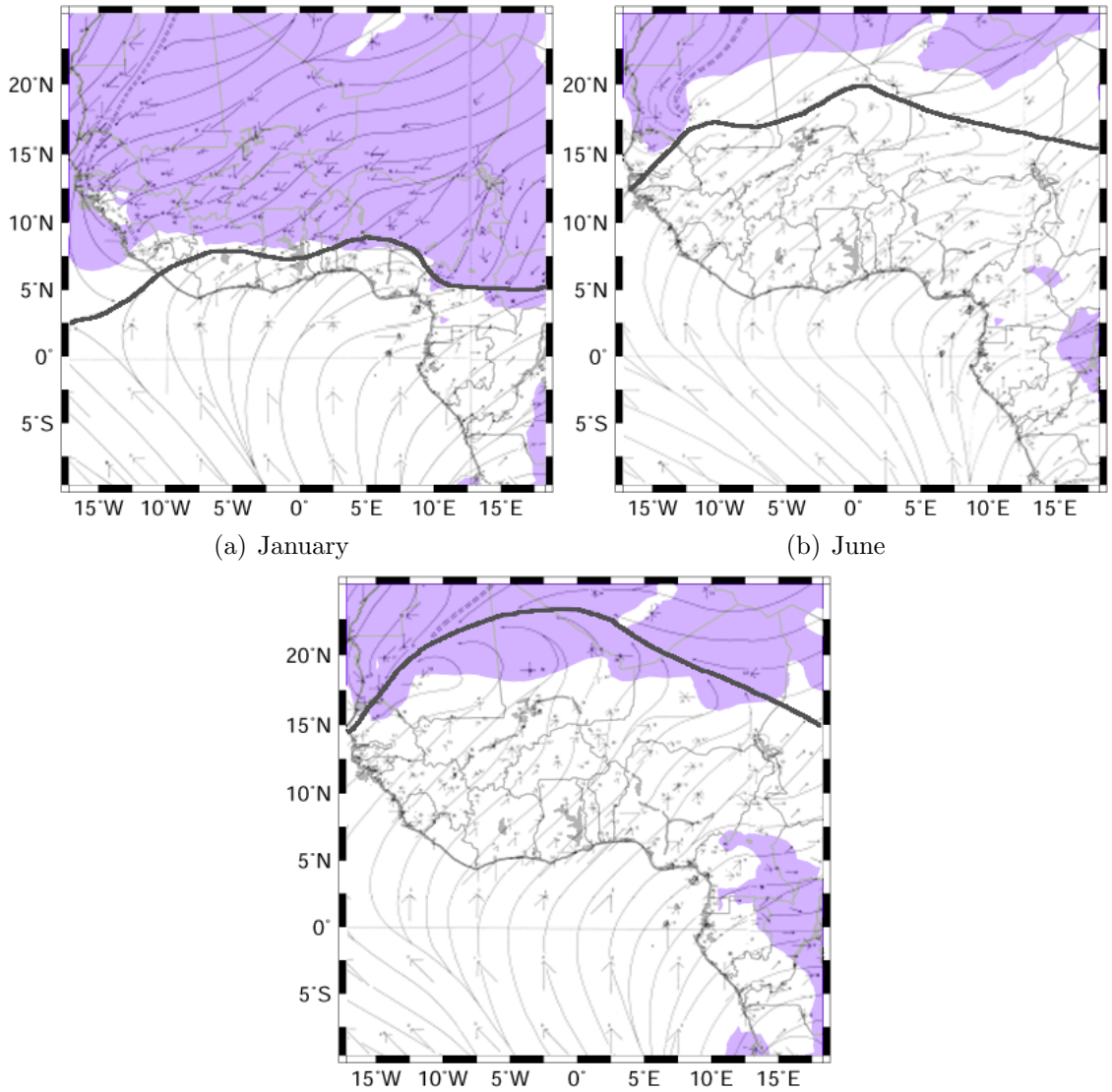

(a) January (b) June

(c) September

Figure 6.19: Mean position of the ITD (D1), shaded: modelled 1991-2000, dashed line: observed long term mean (Leroux, 2001)

mean it is reached one month later, in July. The ITD stays more or less in this northern position for 2 months (3 months) for the mean observed climate (RCM simulations). The northernmost position of the RCM simulations is again in good agreement with observations in July and August. At the end of the rainy season, a deviation of the position of the ITD from the long term mean can again be observed. The displacement of the ITD to the South in September and October occurs too rapidly as well in the model results. Nevertheless a good agreement with observations can be achieved for the latitudinal position of the ITD from December to February and in July/August.

Summary - Validation Downscaled GCM Runs Temperature shows a small positive deviation between the RCM simulations and the GCM results for most regions. The representation of rainfall amounts is rather weak in the RCM simulations for the largest model domain, but improves significantly with increasing resolution. Topographic influences are clearly resolved more adequately for both temperature and precipitation (even in D1). Consequently an improvement in the spatial representation can be achieved. The spatial mean annual cycle of rainfall shows a good agreement between the RCM results of D3, and long term mean observations. The spatial representation shows a large negative bias in the South, and a small positive bias in the North. Regional climate simulations and long-term mean observed state are in good agreement concerning the northernmost and southernmost position of the ITD. Nevertheless, the movement of the ITD to the North, as well as the displacement back South at the end of the rainy season, occur too rapidly. Because the onset and the secession of the rainy season are strongly triggered by the position of the ITD, this has a possible influence on the start of the rainy season and the length of the rainy season.

6.4 Coupled Modelling System

A validation of the coupled modelling system was performed for the year 1968.

River Discharge The Nash-Sutcliffe Efficiency (NSE) values are summarized in table 6.2 for all subcatchments where observational data was available, for the calibration run,

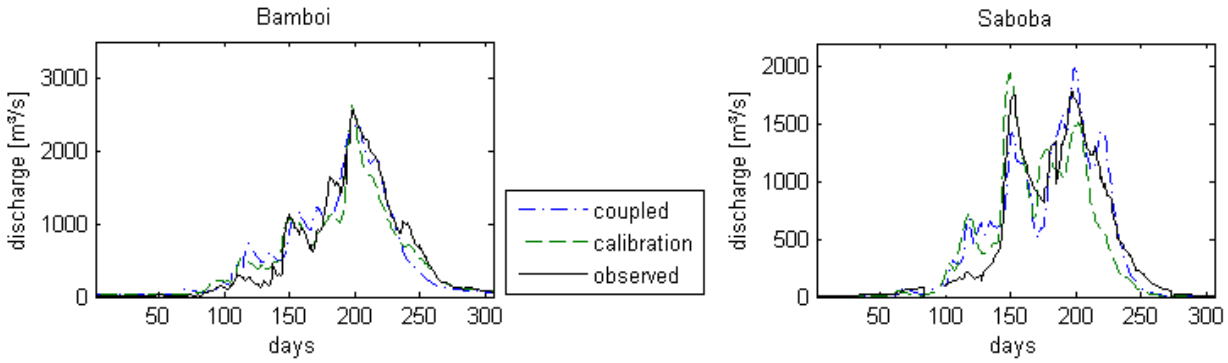

Figure 6.20: Observed and simulated runoff [m^3s^{-1}] (calibration run and coupled MM5-WaSiM run), left: Bamboi, right: Saboba, 1968

as well as for the coupled model simulation.

Table 6.2: Nash-Sutcliffe Efficiencies for calibration and coupled model simulation

gauge	Bamboi	Boromo	Dapola	Ekumdipe	Hohoe	Nawuni	Pruso	Pwalugu	Saboba
calib	0.95	0.31	0.82	-0.12	-0.23	0.84	-5.08	0.3	0.85
coup	0.92	-0.73	-0.48	-0.06	-0.75	0.79	-0.13	0.26	0.9

For most gauges the coupled run performance is poorer, except for Saboba. This better performance for Saboba can also be evaluated, with a direct comparison of runoff curves (figure 6.20). Mainly, this is due to the better representation of spatial rainfall distribution within the coupled simulation. As mentioned earlier, WaSiM, when run with observational data, produces interpolation errors, especially in the subcatchment Saboba due to the sparseness of rainfall gauges. Saboba is the second largest subcatchment (55817 km^2), but has only 6 observational stations contributing to rainfall interpolation within the subcatchment.

One bias that is obviously not due to the driving meteorological input fields, because it is found in both the calibration and the coupled run for both gauges, Saboba, and Hohoe, is the strong overestimation of runoff at the onset of the rainy season. This is probably due to an insufficient representation of the soil moisture dependence of the saturated hydraulic conductivity, or due to an underestimation of soil moisture.

The rainfall deficit along the coast that was found within the MM5 simulations has also got an influence on discharge simulation of the subcatchments in the South. Of these only Aframso and Pruso can be validated, as the other catchments that border Lake Volta are 'artificial' ones, for which no observational data is available. Comparing these gauges to the calibration runs of the same period shows a discharge deficit in the coupled simulations.

6.5 Discussion of Uncertainties

Within the present coupled modelling approach there is a great variety of uncertainties.

Observations One uncertainty that is always apparent in data sparse regions like West Africa is the uncertainty that is caused by measurement errors and the sparseness of station data (Giorgi et al., 2001; Washington et al., 2004). In particular, if data is spatially interpolated, strong errors can be introduced when only few stations are available. The problem is not as serious for temperature, as for precipitation within the region, because temperature has a better spatial representativeness, especially in the absence of high mountains. In the case of precipitation, the number of stations was larger. Nevertheless, due to the spatially extremely heterogeneous distribution of convective rainfall events, a spatial interpolation is questionable, though indispensable to obtain hydrological model input.

These measurement and interpolation uncertainties contribute to the uncertainty in the validation results of the global and regional climate models, as well as the hydrological model. In addition, the calibration of WaSiM is limited by the accuracy of the observational data and the interpolation method.

Emission Scenarios A first uncertainty in climate projections is the uncertainty that lies within the assumptions that were made for the chosen emission scenario. This simply is due to the uncertain development of socio-economies and technologies and the subsequent emissions of greenhouse gases, globally as well as locally. Another source of uncertainty lies within the conversion of these scenarios' assumptions to atmospheric concentrations and radiative effects (Giorgi et al., 2001).

Global Climate Model The next source of uncertainty can be traced to the internal model uncertainties of the GCM. One key question addressed by Bengtsson (2003) in this context is, to what extent the same modelling approach as applied in numerical weather prediction might be equally successful for climate modelling and prediction. He mentioned the difficulties that lie in the chaotic nature of atmospheric processes, the variety of processes that are involved in long term simulations (atmospheric, oceanic, land surface related, chemical and biogeochemical processes) and the natural and anthropogenic external influences. A striking observation of Giorgi and Francisco (2000), considering GCMs on a regional scale for selected regions of the world, was that the dominant source of uncertainty lies more in inter-model variability and less in inter-scenario or internal model variability. Within the CLIVAR project (*www.clivar.org*) a series of simulations was performed that showed that inter-decadal variability due to El Nino and La Nina events as well as the atmospheric response to the accompanied SST anomalies can be reproduced by GCMs. The correct representation of SST variability is essential for climate impact studies in West Africa.

In the ECHAM4 simulations of the transient IS92a run, from which a time slice was selected for this study, mean annual temperature did not show strong biases. A bias that is observed within the ECHAM4 simulations, is a shift in rainfall to the North. Subsequently rainfall amounts along the southern coast of West Africa are underestimated, and precipitation in the Sahara is overestimated.

Regional Climate Model There is also the uncertainty in the regional climate model MM5. First of all there is a model intrinsic uncertainty that is due to imperfect knowledge or representation of physical processes, limitations due to numerical approximations of the physical equations and assumptions or simplifications that have to be included in the physics parameterization schemes. The domain choice, as well as the spatial resolution are other sources of uncertainty in limited area modelling (Kotlarski et al., 2005).

In this study it was demonstrated that MM5, when downscaling reanalysis data, has a bias in temperature that is dependent on latitude and season. The largest positive bias was found during the rainy season in the North of the basin. In the dry season the bias was negative in almost all regions, whereas along the coast, a negative bias was found all year. Precipitation shows a strong negative bias along the coast, but comparably good results for the Volta region. It is most likely that both the bias of temperature and the bias of precipitation along the coast are caused by an underestimation of sea surface temperature. However, also incorrect representation of boundary layer and convective processes within the parameterizations cannot be excluded.

In addition, inter-model and inter-method differences in the response to a given forcing have to be mentioned as source of uncertainty. For the region of West Africa and the impact

analysis in the Volta Basin, rainfall is of major importance. Nevertheless, this also turns out to be the variable with the highest degree of uncertainty within the climate simulations. A comparison of the 10-year time slice for the reference state, present-day climate, with the observed long-term mean was performed in the present study. This validation has a limited informative value due to the short time span of the simulation results. However it is assumed, that averaging over a longer observed time span, reduces the signal of variability, and the possibility of complementary decadal variability signals of observed and simulated time slice. Therefore, this analysis was chosen for an estimation of the performance of the regional climate simulations, with respect to observations. The results indicated a sufficient accuracy of the annual cycle of mean basin wide rainfall and the respective monthly amounts. The spatial consideration showed an underestimation of rainfall along the coast that is already introduced to the model runs by the ECHAM4 input data, and most probably intensified by the MM5 weakness to reproduce coastal rainfall. For the northern part of the Volta Basin a small overestimation of temperature was found. Furthermore inter-annual variability was found to be overestimated within the model simulations.

To overcome, or at least evaluate the high degree of uncertainties in climate simulations, recently ensemble predictions are favoured not only on the global, but also on the regional scale, as e.g. in the QUIRCS project (*www.tu-cottbus.de/meteo/Quircs/home.html*), the PRUDENCE project (*http://prudence.dmi.dk)*, or the ENSEMBLES project (*www.ensembles-eu.org*). Ensemble runs mean using either different models or different parameterization schemes, initial conditions, lateral and lower boundary conditions, resolutions etc. For the detection of a reliable climate change signal, an averaging of ensemble runs is for sure feasible. Nevertheless as Giorgi (2005) states, ensemble averaging alone might not be sufficient to provide optimal information, as inter-decadal variability, in particular sudden changes, that can have a significant impact are not captured. He proposed to add some measures of inter-decadal variability to the ensemble averaged climate change signal.

Ensemble runs using several models with a variety of emission scenarios are very important to quantify uncertainties caused by emission scenarios and differing modelling architectures. Due to the high resolution of the simulations within this study and the subsequent time consuming runs, no ensemble approach could be performed. Therefore, the chosen experiment consists of the central emission scenario IS92a, simulated with the GCM ECHAM4.

Lower Boundary Conditions While in meteorological forecasts the lower boundary conditions play a minor role and the right initialization is the more important factor determining predictability, in climate runs surface characteristics need to change with the season and the developing dynamics is more dependent on the lower boundary conditions and less on initial conditions in the long run. This was already shown to be true for 2 weeks simulations by Shukla (1998).

These lower boundary conditions are not only important for long simulation periods. They are even more important in West Africa due to the less chaotic dynamics of the tropical atmosphere. Shukla (1998) showed that even under initial conditions that were disturbed as much as the largest observed differences in the last 50 years, the simulation results for certain tropical regions converged towards nearly identical results. This is in sharp contrast to the dynamics of mid latitudes where the results for simulations with

differently disturbed initial fields would diverge, as can be verified from ensemble predictions of the weather services. However, according to SHUKLA (1998), no proper explanation for this property of the tropical atmosphere is known and 'accurate or useful forecasts for tropical circulation and rainfall can be made only if the tropical SST itself is accurately predicted'.

Therefore, in GCM, as well as RCM simulations, an important source of uncertainty for West Africa lies in the representation of SST. In the global-scale simulation, there is the uncertainty of the global ocean model OPYC. For the regional climate model MM5, like in general nowadays, no mesoscale ocean model is coupled. Subsequently, the information of SST always stays in the coarse resolution of the GCM. This neglects mesoscale impacts of the atmosphere on the sea surface and mesoscale structures in ocean dynamics. Within meteorological forecasting and hindcasting this problem can be diminished through the inclusion of high resolution satellite derived SST data in the meteorological model (PHADNIS et al., 2003). In regions like West Africa, that are highly sensitive to SST variability, one option is to run coupled ocean-atmosphere regional climate models. Ensemble runs, with disturbed sea surface temperatures are also a possibility to evaluate the impact of uncertain SSTs on climate simulation results.

Hydrological Model Like for the RCM, there is additionally some uncertainty lying in the hydrological model itself, dependent on the physics description and the numerics. The data transmission from the regional climate model to the hydrological model also is a source of uncertainty in the interpolation of the meteorological data from the MM5 output grid to the finer WaSiM input grid. Additional to the model uncertainty due to insufficient representation or knowledge of the physics, the uncertainty dependent on parameter choice has to be mentioned. This source of uncertainty is the easiest to evaluate in hydrological modeling, through sensitivity studies. An approach of stochastic hydrological modeling, using the Monte-Carlo method was therefore chosen within this study. The subsequent parameter uncertainty of WaSiM is demonstrated for some selected, sensitive parameters, in section 5.2.3. This analysis indicated that the largest range of uncertainty was found for the empirical model parameter d_r (drainage density) and therefore, the physically based model demonstrates its strong empirical determination of runoff generation. Another uncertainty in WaSiM within this study is due to the assumption of constant rainfall intensity for the entire time step. Due to the fact that in West Africa rainfall is mostly of convective origin and rainfall events are strongly limited in time, an underestimation of infiltration excess is probable, when the model is run with a daily time step.

Neglected Impacts to Regional Climate What is lacking both the regional, as well as the global climate simulations is a proper representation of dynamic land cover-atmosphere interactions, as well as dust and biomass aerosols. Such interactions were determined as important for African climate variability during the Holocene (HULME et al., 2001). They may not be negligible for future projections as well. Another source of uncertainty in the present study lies in the fact that no land-use change is considered. For West Africa, land-use change may be influencing climate change and the subsequent impact on hydrology, besides an increase in greenhouse gases. First, land-use change has a high level of impact on the atmosphere through feedback mechanisms (sections 2.1 and 2.3) and is therefore a source of

uncertainty for the regional climate simulations. Furthermore, land use change can directly influence the runoff response of a region, through an influence on infiltration properties of the soil (Mbagwu, 1997; Giertz and Diekkrueger, 2003). This, in addition, leads to an uncertainty in hydrological modelling if the impact of land-use change is neglected.

Chapter 7

Impact of Global Climate Change

In this chapter the sensitivity to climate change on the regional scale is investigated. Therefore, the two simulated time slices: present (1991-2000) and future (2030-2039) are compared and analyzed. As a start of the analysis, the MM5 output for the largest domain (D1) is used to analyze the large scale patterns of the climate change signal (section 7.1.1). In the next section (7.1.2) the influence of the global climate change signal on the regional scale is investigated for the region of the Volta Basin (D3). Finally the translation of the atmospheric climate change signal to the hydrology of the Volta Basin are analyzed in section 7.2

As important part of the analysis that was applied to atmospheric, as well as hydrologic output variables is the signal to noise ratio (SN), defined as

$$SN = \frac{\mid \overline{X_{fut}} - \overline{X_{pres}} \mid}{\sigma} \tag{7.1}$$

with $\overline{X_{fut}}$ and $\overline{X_{pres}}$, the mean monthly or annual value of a given variable for the future and the present time slice respectively. σ is the standard deviation of this variable for the present time slice. A value of $SN > 1$ indicates a detected change signal, that lies outside the simulated inter-annual variability (noise) of the present-day time slice.

Another variable that is central to the analysis within all three sections, is the inter-annual variability [%] of a certain meteorological or hydrological variable. This is described via the coefficient of variation (also referred to as *variations coefficient*)

$$varc = \frac{\sigma}{\overline{X}} 100 \tag{7.2}$$

with standard deviation σ and mean value of a certain variable $\overline{X}$.

7.1 Regional Climate Simulations

7.1.1 Large Scale Patterns

The analysis of the large scale patterns (in D1) considers temperature and precipitation means and annual cycles, the position of the ITD, the strengths of TEJ and AEJ, as well as moisture in the monsoonal layer and changes in SST.

Temperature The climate change signal for temperature (figure 6.13 in section 6.3) shows a clear increase all over the model domain. The increase in temperature ranges from 0.5°C in the maritime South of the region up to 2°C in the Sahara. A look at the spatially averaged annual cycle of temperature (table 7.1) shows a uniform temperature increase for the entire year.

Table 7.1: Mean monthly and annual temperatures (1991-2000 and 2030-2039) [°C], and temperature changes [°C], D1

	$\overline{1991-2000}$ [°C]	$\overline{2030-2039}$ [°C]	ΔT [°C]
January	27.6	28.3	0.7
February	29.7	30.8	1.1
March	32.2	33.3	1.1
April	32.4	34.3	1.9
May	31.0	32.8	1.8
June	29.8	31.0	1.2
July	29.3	30.4	1.1
August	29.1	30.2	1.0
September	30.1	30.7	0.6
October	31.4	32.3	1.0
November	30.1	31.5	1.5
December	27.4	28.9	1.5
year	30.0	31.2	1.2

Mean temperature change is large, compared to the standard deviation σ of both time slices. The standard deviation for mean annual temperature of the present-day time slice is 0.3°C, σ of the future time slice is a bit larger with 0.4°C. Mean temperature change between the two time slices (averaged over space and time) is calculated to be 1.2°C. This leads to a high value for the signal to noise ration of 3.9. Therefore a clear signal of change can be observed for the two 10-year time slices that were simulated within the present study.

SST The analysis of SST revealed an overall increase for the tropical Atlantic, between 0.4 and 1°C (figure 7.1). The increase in latent heat fluxes due to higher SSTs and higher air temperatures leads to a higher moisture content over the ocean, that is transported inland with the monsoonal flow.

Precipitation Annual precipitation change, as depicted in figure 6.16 (section 6.3), shows a slight increase over most of the region (entire D1). The strongest increase occurs in the region of Guinea-Bissau, Guinea and in eastern Niger/western Tschad. Regions of decreasing precipitation can be detected in the West of West Africa, in the countries of Senegal, Mauritania and Western Sahara.

Figure 7.2 shows this annual cycle of the spatially averaged precipitation of the first MM5 model domain. Averaged over the entire D1 region, a shift from a unimodal annual

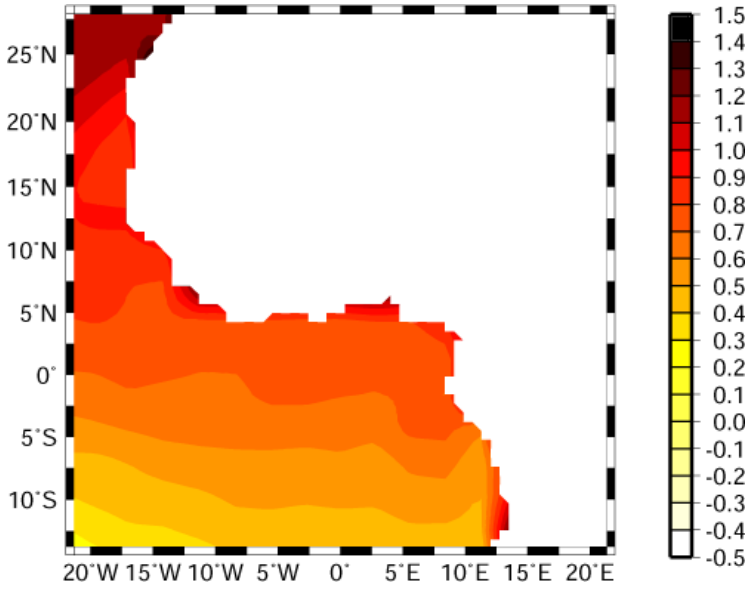

Figure 7.1: Change in mean annual sea surface temperature [°C] (2030-2039 vs. 1991-2000), D1

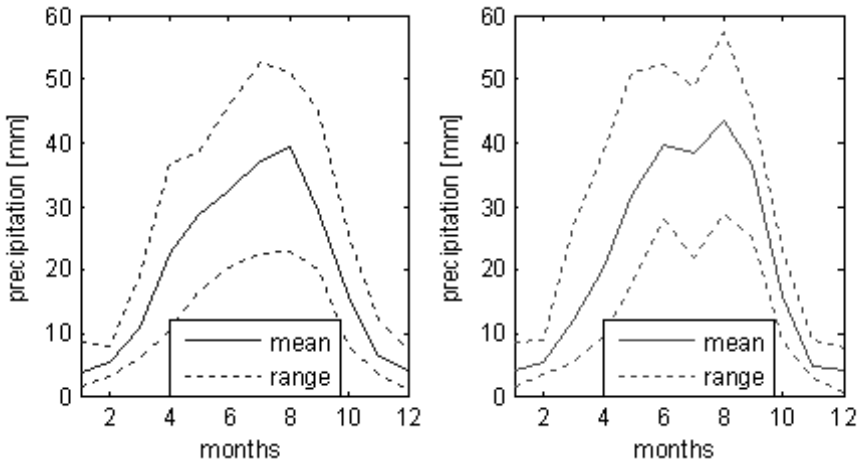

Figure 7.2: Mean, mimum and maximum monthly values of spatial mean rainfall [mm] (D1 total), left: 1991-2000, right: 2030-2039

cycle of rainfall, with a maximum in August to a bimodal one with a first maximum in June and a second in August can be detected. This figure also indicates the relatively small change compared to inter-annual variability. This is illustrated by the large range of monthly precipitation sums within the respective 10 years of each time-slice. Mean annual precipitation sum is 626.1 mm for the 1991-2000 time slice, the mean for the 2030-2039 simulation is 706.8 mm. This means that on average, annual rainfall increases by 80.7 mm in West Africa, within the future simulation with respect to the reference simulation. However, the standard deviation is 147.7 mm in the reference state and 142.9 mm in the future simulation. This results in a signal to noise ratio of 0.55. Therefore no significant signal of change can be observed for spatial and annual mean precipitation over the entire model domain D1.

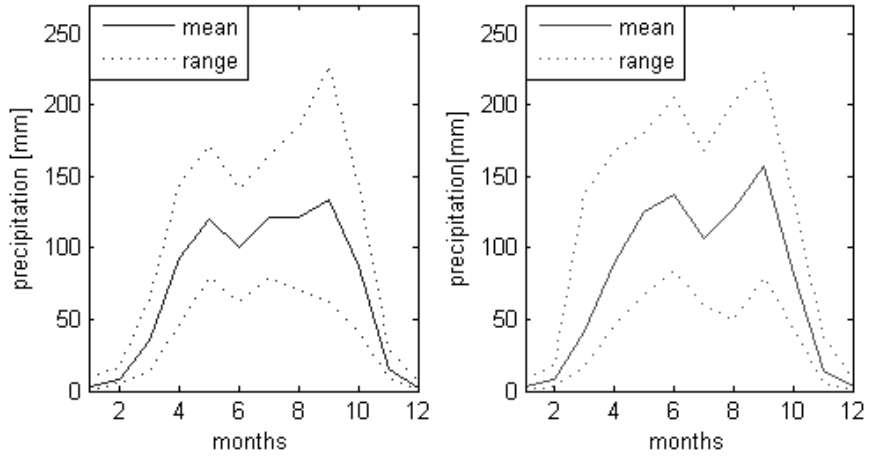

Figure 7.3: Mean, minimum and maximum monthly values of spatial mean rainfall [mm], for the Guinea Coast region, left: 1991-2000, right: 2030-2039

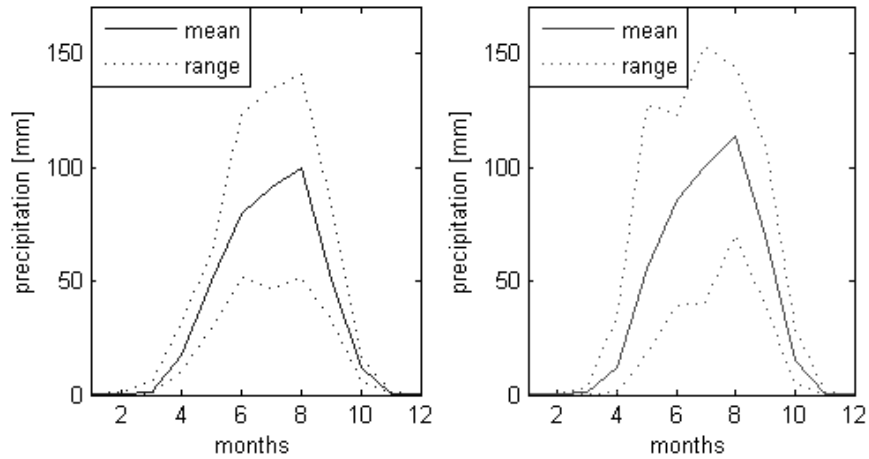

Figure 7.4: Mean, minimum and maximum monthly values of spatial mean rainfall [mm], for the Sahel region, left: 1991-2000, right: 2030-2039

The more interesting climate change signal does not lie in a pure annual quantity signal,

Table 7.2: Mean monthly and annual precipitation sums (1991-2000 and 2030-2039) [mm], standard deviation [mm], absolute [mm] and relative [%] changes, Guinea Coast region

Coast	$\overline{1991-2000}$	$\overline{2030-2039}$	$\sigma(1991-2000)$	ΔP [mm]	ΔP [%]
January	2.9	2.8	2.4	-0.1	-2.4
February	7.8	8.2	3.8	0.5	6.0
March	34.6	41.0	15.1	6.4	18.5
April	93.5	88.9	34.7	-4.5	-4.8
May	119.8	124.8	28.5	5.0	4.2
June	100.3	138.0	24.4	37.7	37.6
July	121.3	106.6	29.7	-14.7	-12.1
August	121.2	127.3	39.7	6.1	5.1
September	134.1	156.7	48.3	22.7	16.9
October	87.5	82.2	35.7	-5.3	-6.0
November	15.2	13.9	6.1	-1.3	-8.7
December	2.5	3.4	1.7	0.9	36.8
year	840.6	894.0	80.6	53.4	6.4

but in a spatial and temporal distributed change signal, which will be investigated more closely in the following. Furthermore, a differentiation between the two differing climatic regions, the Sahel, and the Guinea Coast region was done. Within the present study the division of Nicholson and Grist (2001) with the borderline between the Sahel and the Guinea Coast region drawn at 10°N was selected. Therefore the Sahel region spans the latitudes 10-20°N. In the South, the Guinea Coast region is limited by the 2°N parallel. Furthermore, only the land surface was taken into consideration for averaging both regions.

Looking at figures 7.3 and 7.4 highlights the different precipitation change signals of these two regions. The Sahel region, with its unimodal annual cycle shows a rather uniform increase in precipitation for the height of the rainy season and a pronounced decrease in precipitation at the beginning of the rainy season in April. This signal is small in absolute values, as precipitation amounts are still low in April, but it is large, considering the percentage precipitation change signals.

The corresponding values are summarized in tables 7.3 and 7.2. The values indicate that the annual SN rate is 1.2 for the Sahel region, but only 0.7 for the Guinea coast area, indicating a slightly higher reliability of the change signal for the Sahel region. For the majority of the monthly values the standard deviation is higher than the signal of change. An exception is the month of June in the Guinea Coast region, where a SN value of 1.5 is obtained.

For the Sahel region, the only month with a SN value slightly exceeding 1 is September with $SN = 1.1$. In April and October, the change signal is almost as large, as the standard deviation in the Sahel. In all remaining months, the change signal is much smaller than inter-annual rainfall variability.

Rainfall in the Guinea coast region does not show a significant change in the early rainy season, but it shows a pronounced change of the bimodal cycle, with a shift from an intra-seasonal rainfall minimum in June for the 1991-2000 time slice to July for the 2030-2039 time-slice. This signal includes a decrease in July precipitation and a strong increase in

Table 7.3: Mean monthly and annual precipitation sums (1991-2000 and 2030-2039) [mm], standard deviation [mm], absolute [mm] and relative [%] changes, Sahel region

Sahel	$\overline{1991-2000}$	$\overline{2030-2039}$	$\sigma(1991-2000)$	ΔP [mm]	ΔP [%]
January	0.1	0.1	0.2	-0.01	-15.1
February	0.3	0.2	0.3	-0.1	-47.2
March	1.4	1.4	1.6	0.0	1.2
April	17.8	12.2	7.2	-5.6	-31.5
May	50.3	55.2	13.4	4.9	9.8
June	79.8	85.6	20.2	5.8	7.3
July	91.3	100.7	29.9	9.4	10.3
August	99.6	113.8	27.3	14.2	14.3
September	51.0	69.9	17.0	18.9	37.1
October	11.7	15.0	3.4	3.3	28.2
November	0.4	0.4	0.5	-0.1	-17.3
December	0.1	0.0	0.1	-0.1	-92.0
year	403.7	454.4	43.8	50.7	12.6

precipitation in June, not only along the coast, but also in the southern Sahel.

Through the change in bimodality along the coast the slight bimodal signal is introduced to the whole regions' future annual cycle of rainfall, which has already been described. Figure 7.5 illustrates the spatial distribution of the percentage rainfall change from present to future time slice simulations for the months of April, July, and September. This shows a rather uniform decrease in precipitation for the months of April at the onset of the rainy season. September demonstrates the increase in rainfall over the entire West African continent, which is most pronounced south of the Sahara and in the Sahel region. The sensitivity of rainfall in July, in contrast, reveals a dipole character, with a decrease in rainfall in coastal regions, and an increase in the Sahel and the Sahara, the largest increase being in the southern Sahel region.

Inter Tropical Discontinuity (ITD) Within the present study, the meridional wind component was used to analyze the position of the ITD. The investigation of the mean monthly latitudinal position of the ITD (figure 7.6) shows only a small range for the present-day climate, compared to the future scenario, especially in the months of the rainy season. This indicates that the inter-annual variability of the ITD position is larger in the future time slice.

In figure 7.7 the mean change in the ITD position in degrees latitude was analysed. Here two larger signals can be extracted. In April a negative displacement of almost 1.5°, indicating a more southerly mean position in the future scenario, can be observed. In September the mean ITD position lies further north in the future simulation than in the present, reference state simulation.

An illustration of the longitudinal dependency of the ITD position can be found in figure 7.8. This shows that, for example, the northernmost position of the ITD is in any month detected in central West Africa between 0 and 5°E. In most months this longitudinal pattern persists, even if the latitudinal position is changed. An exception is May, where

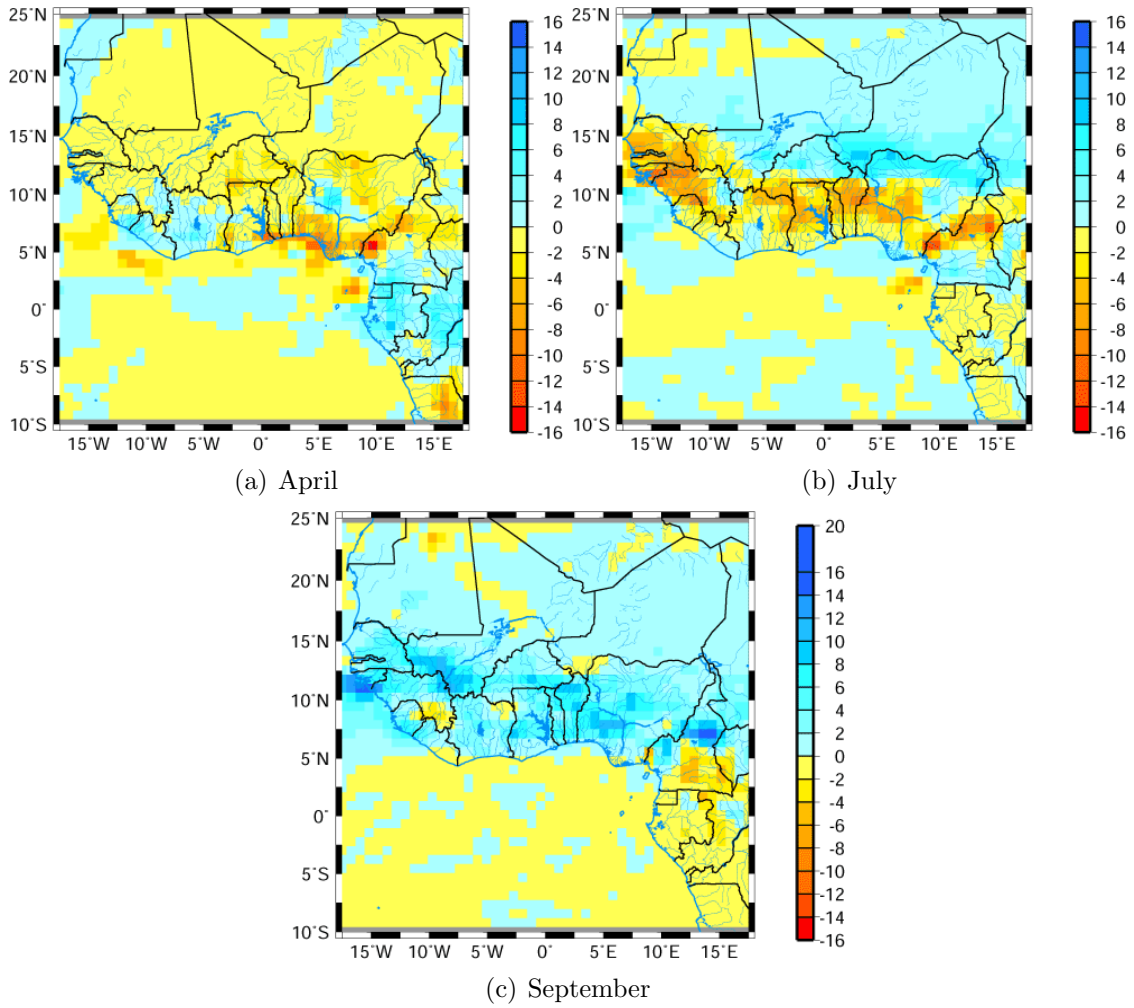

(a) April (b) July

(c) September

Figure 7.5: Mean precipitation change [mm] (1991-2000 vs. 2030-2039)

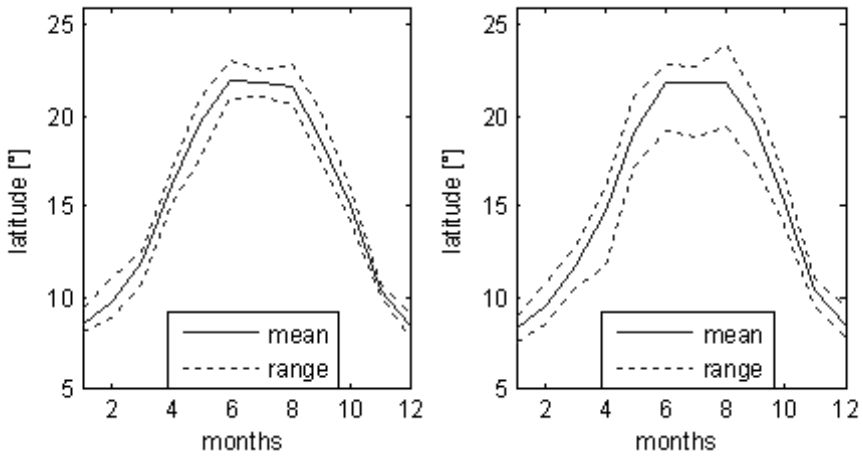

Figure 7.6: Mean, minimum and maximum monthly ITD position, left: 1991-2000, right: 2030-2039

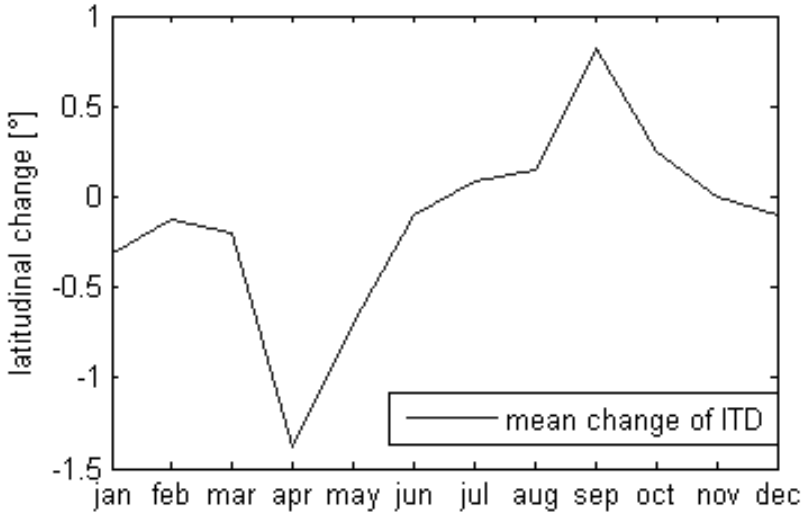

Figure 7.7: Mean monthly ITD position change (1991-2000 vs. 2030-2039)

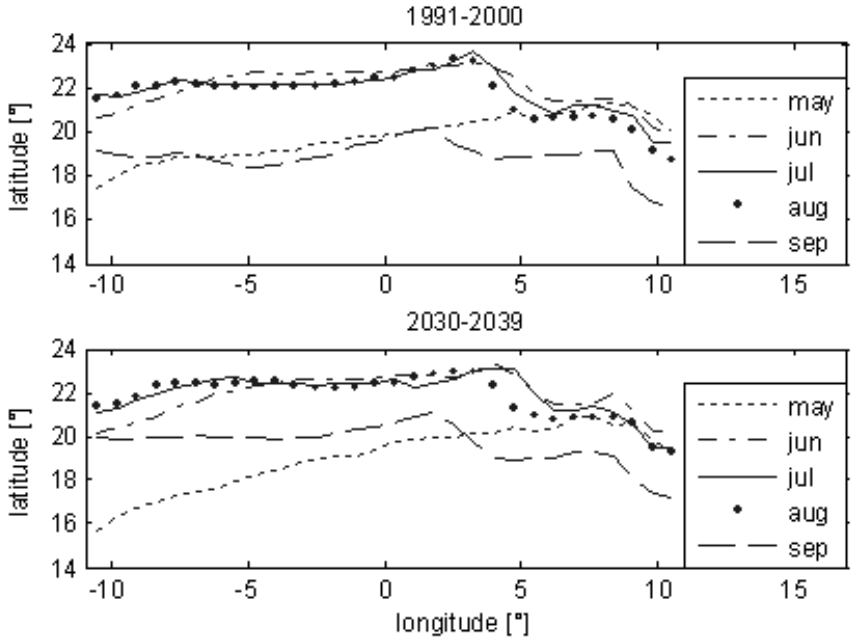

Figure 7.8: Mean latitudinal and longitudinal ITD position for months of the rainy season above: 1991-2000, down: 2030-2039

a pronounced displacement of the ITD occurs west of 7°W, and in the remaining area no obvious changes occur. The two signals of change in the latitudinal position of the ITD in April and September are accompanied by a decrease in precipitation in April, which was already mentioned in the previous paragraph, and an increase in precipitation in September (figure 7.5). For the signal in the change of bimodality in June and July no coherence with the ITD could be detected.

Tropical Easterly Jet (TEJ) An analysis of the TEJ was performed by considering the wind in the σ -level in approximately 200 hPa.

The TEJ only shows pronounced differences in strength for the month of July and June, which is shown in figures 7.9 and 7.12. A weaker TEJ for future climate conditions in June, and a stronger TEJ in July is found. Nevertheless the TEJ does not change its mean monthly position in future climate simulations significantly, compared to the modelled present climate conditions.

African Easterly Jet (AEJ) The AEJ was examined via the wind in approximately 600 hPa. The largest difference between future and present climate simulations is found in the months of April and July. Whereas in April a stronger AEJ is observed (figure 7.10) in the future simulations, in July it is weaker (figure 7.11). In June (figure 7.12), the winds in the low level jet are weaker in the area of the jet maximum, but stronger at its southern edge over coastal regions[1].

Moist Monsoon Layer Rainfall intensity can not be solely dependent on the dynamics described by jet streams and the position of the ITD in the rainy season. Additionally, the moisture that is available in the monsoonal layer and above is important in the production of intense rainfall events and the limitation of the intensity of convectious rainfall events. Especially in the case of higher temperatures in the future climate simulation, a higher moisture availability due to an enhanced latent heat flux to the atmospheric boundary layer can be expected. Therefore, the mixing ratio in approximately 700 hPa was analysed. In agreement with the Clausius-Clapeyron equation, in almost all months an increase in mixing ratio over the West of the African continent was found, whereas over the ocean and near the coast over land in some months a decrease was simulated.

Figure 7.13 demonstrates a decrease in moisture of the mid-troposphere in April, which can serve as part of the explanation for the deficit in rainfall at the beginning of the rainy season.

Interaction of Large Scale Patterns According to Janicot (1992) there are two causes for the variability of rainfall in West Africa. One is a variability of rainfall amounts due to a change in the strength of moisture convergence in the monsoonal flow that is linked to a decrease in the intensity of the Hadley circulation. The other cause is a displacement of the ITD. As the moist monsoonal layer is located south of the ITD, a southward displacement of the ITD prevents the moist monsoonal layer from penetrating deep into the continent.

[1]positive (negative) values indicate a reduction (increase) in wind speed, according to the definition of the zonal wind component

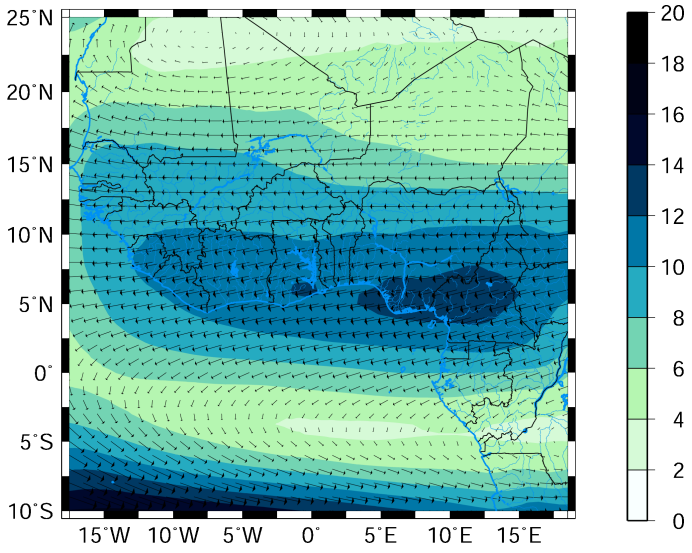

(a) 1991-2000

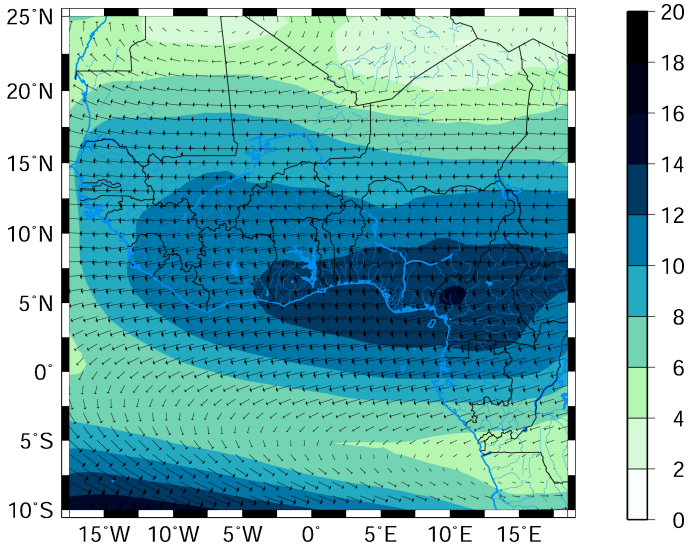

(b) 2030-2039

Figure 7.9: Mean TEJ (shaded: wind velocity [m s^{-1}]; arrows: wind direction in ca. 200 hPa), July

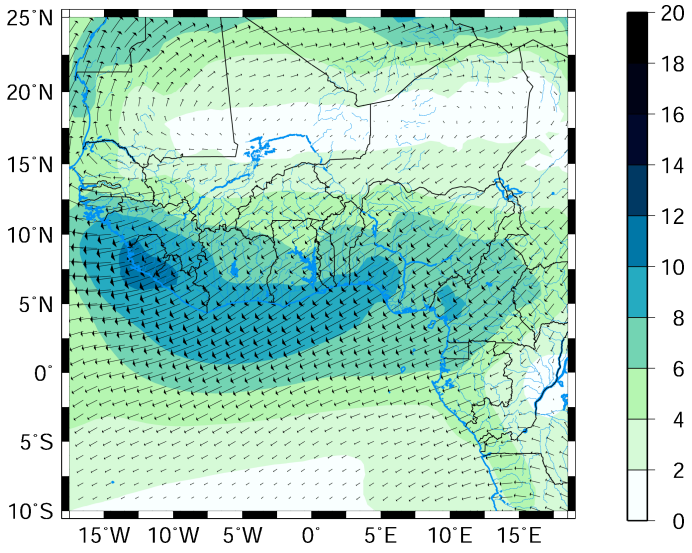

(a) 1991-2000

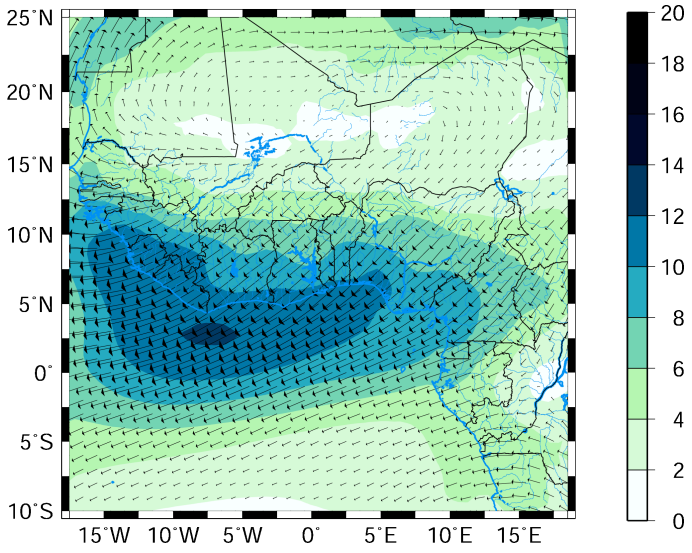

(b) 2030-2039

Figure 7.10: Mean AEJ (shaded: wind velocity [m s^{-1}]; arrows: wind direction in ca. 600 hPa), April

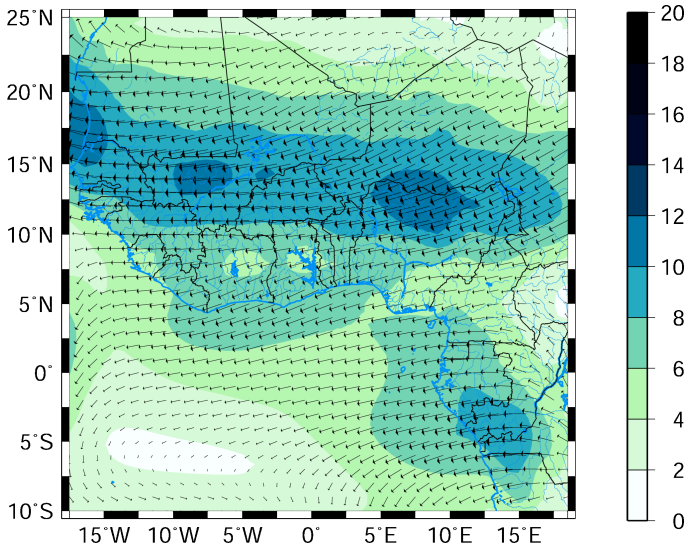

(a) 1991-2000

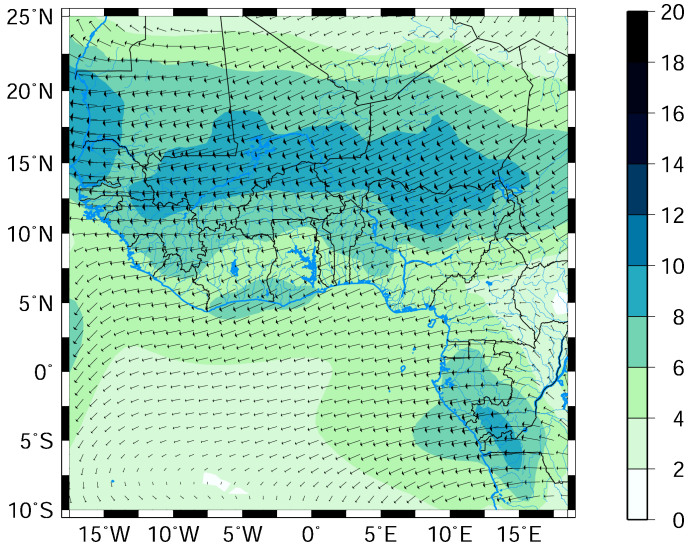

(b) 2030-2039

Figure 7.11: Mean AEJ (shaded: wind velocity [m s^{-1}]; arrows: wind direction in ca. 600 hPa), July

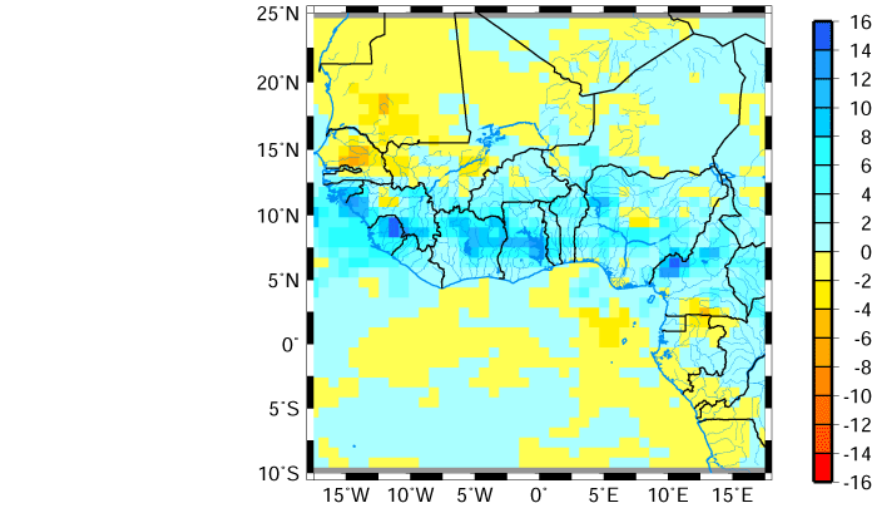

(a) Precipitation change

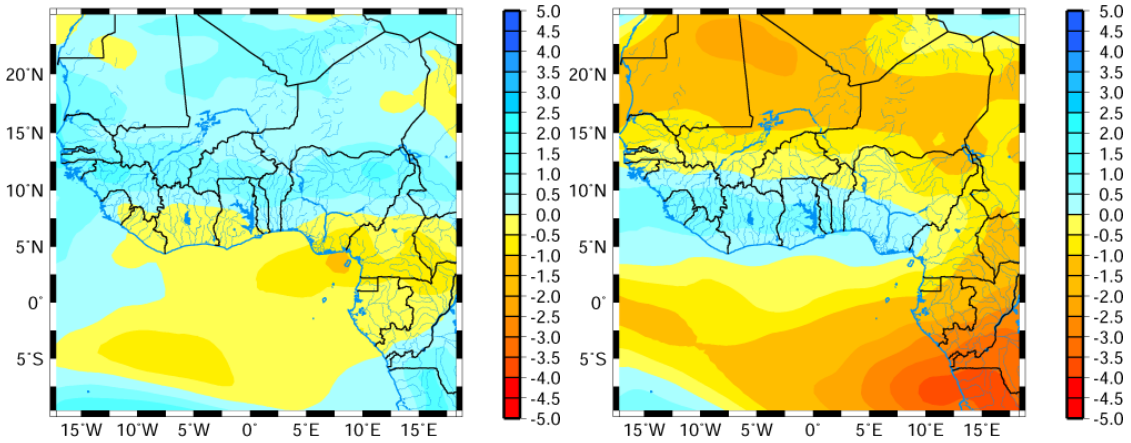

(b) AEJ change

(c) TEJ change

Figure 7.12: Precipitation change [%], change in AEJ (wind velocity [m s^{-1}] and direction in ca. 600 hPa), and change in TEJ (wind velocity [m s^{-1}] and direction in ca. 200 hPa), (2030-2039 vs. 1991-2000), June

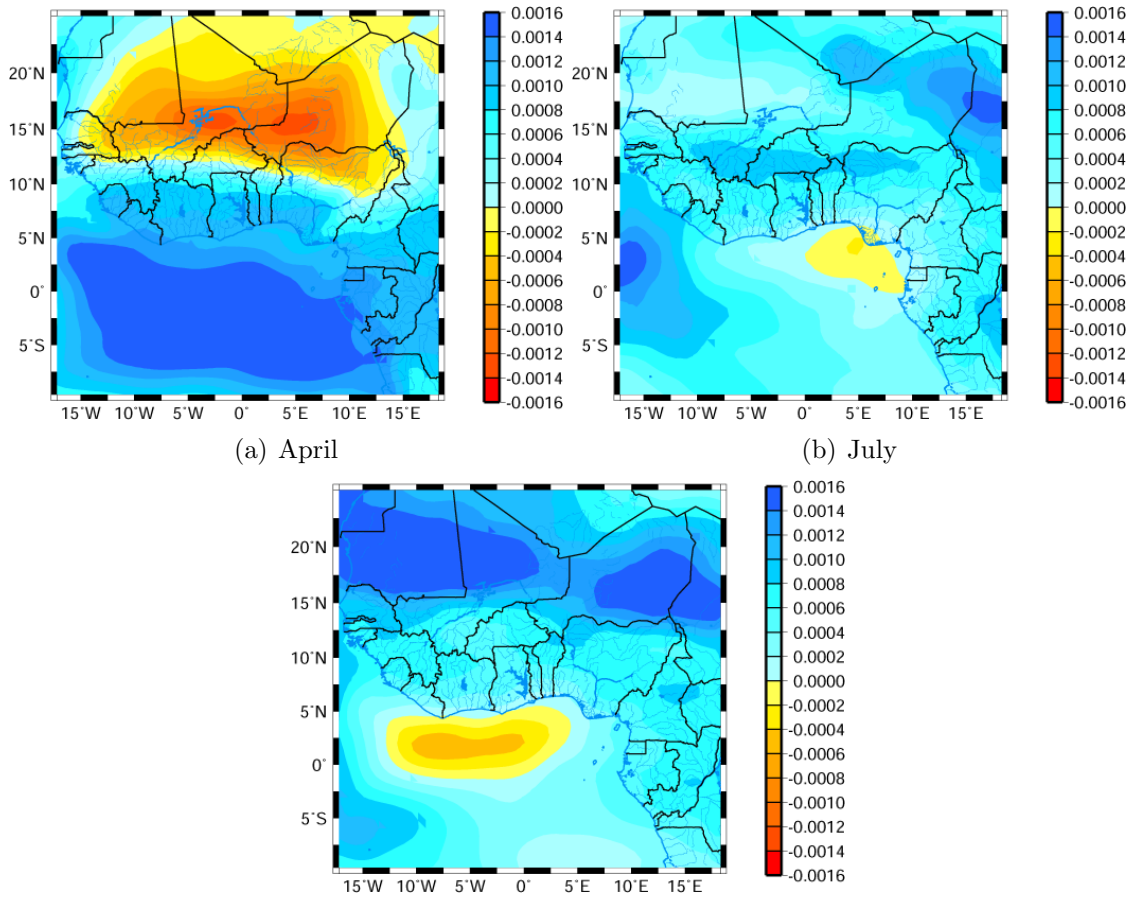

(a) April (b) July

(c) September

Figure 7.13: Moisture mixing ratio change in ca. 700 hPa [1/1] (2030-2039 vs. 1991 -2000)

Some observational studies, like LAMB (1978a) and LAMB (1978b) showed that dry conditions in the Sahel are likely to be associated with a southward displacement of the ITD. For wet conditions no clear northward shift could be delineated.

Nevertheless, within the present study there seems to be a precipitation increase that is connected to the position of the ITD in September. For the strong signal of a rainfall decrease in April a displacement of the ITD to the South could be delineated. For the months of June and July no connection with the mean ITD position was found.

The weakening of the AEJ in July, together with the strengthening of the TEJ can provide an explanation for the dipole signal that is observed, with an increase in precipitation in the Sahel and a decrease along the Guinea Coast. In general, as it has also been described in other studies (compare section 2.1), wet (dry) conditions in the Sahel region of West Africa were found to be connected with a strong (weak) TEJ and a weak (strong) AEJ. Because no significant change in the moisture of the monsoonal layer, nor in the position of the ITD could be found, the causes of the rainfall deficit in July are more likely connected to a change in the strengths of the AEJ and the TEJ. This implies a change of the large scale dynamics that can impact on the formation of *African Easterly Waves* (AEWs) and squall lines (compare section 2.1). For June, a decrease in rainfall amounts was found in the Sahel and an increase along the coast, revealing once more the dipole structure of West

African rainfall variability. In June a strengthening of the TEJ along its southern edge can be observed, with only a weak signal of change in the strength of the AEJ. A higher amount of available moisture could be delineated for June that, in combination with a strengthening of the southern TEJ, can lead to an enhancement of precipitation along the coast.

The signal in the TEJ is weak in April, but the AEJ is much stronger in the future climate scenario run. Therefore no dipole structure can be found in the jet stream dynamics for this month. Nevertheless NICHOLSON (2000) also proposed that there might rather be a stronger (weaker) AEJ due to lower (higher) rainfall amounts than vice versa. This could serve as an explanation for the April AEJ being that strong whereas the reasons for the rainfall deficit might rather lie in the movement of the ITD and the depth of the monsoonal layer.

Summary - Large-Scale Patterns Annual mean temperature shows an increase of 1.2°C with a high signal to noise ratio. The maximum increase in April and May of over 1.8°C was observed. Also SST of the tropical Atlantic showed an increase of around 0.4-1°C. Precipitation increases for both, the Sahel and the Guinea coast region. A signal to noise value greater than 1 could be delineated for mean annual precipitation change only for the Sahel region. Mean monthly rainfall change was only significant for the months of June for the Guinea coast, and for September for the Sahel region. June and July serve as examples for a variability signal in precipitation that is mainly driven by jet stream dynamics, either enhancing the signal of higher moisture availability (June) or reducing it (July). Another result of the two months' dynamics is a strong dipole pattern with an enhancement of precipitation along the coast (June) or in the Sahel region (July) and a reduction of rainfall along the coast (July) and in the Sahel (June). The rainfall change signals in September and April are mostly dependent on how far the moist monsoonal layer reaches inland and so depends on the position of the ITD.

7.1.2 Climate Change Signals in the Volta Basin

Temperature Mean annual temperature shows a clear trend of an increase for the region of the Volta Basin, similar to the larger scale simulations shown in section 7.1.1.

Table 7.4: Mean monthly and annual temperatures (1991-2000 and 2030-2039) [°C], and temperature changes [°C], D3

	$\overline{1991-2000}$ [°C]	$\overline{2030-2039}$ [°C]	ΔT [°C]
January	28.1	28.9	0.8
February	30.1	31.3	1.2
March	32.4	33.6	1.2
April	32.2	34.3	2.1
May	30.1	32.2	2.0
June	28.8	30.1	1.3
July	28.4	29.6	1.2
August	28.2	29.3	1.1
September	29.1	29.8	0.7
October	30.9	31.9	1.0
November	30.4	32.0	1.6
December	27.9	29.6	1.6
year	29.7	31.0	1.3

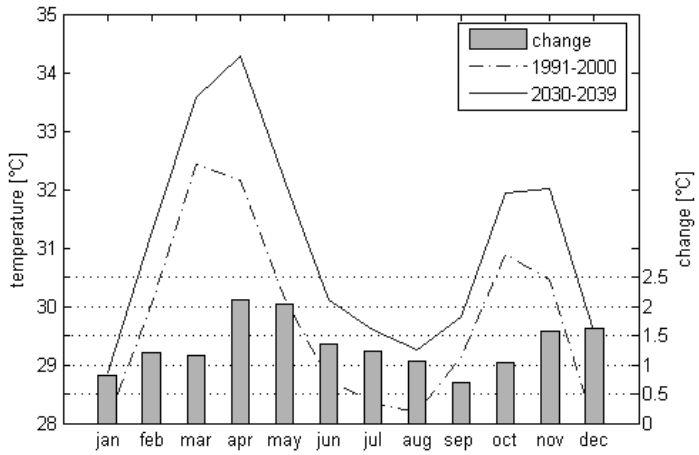

Figure 7.14: Spatially averaged mean monthly temperature [°C] (1991-2000 and 2030-2039) and temperature change [°C], D3

This increase ranges from 1°C in the maritime South to 1.5°C in the continental North. The increase in temperature can be detected not only for the mean annual value, but also over the entire annual cycle (figure 7.14, table 7.4), with a maximum in April (2.1 °C) and a minimum in September (0.7 °C).

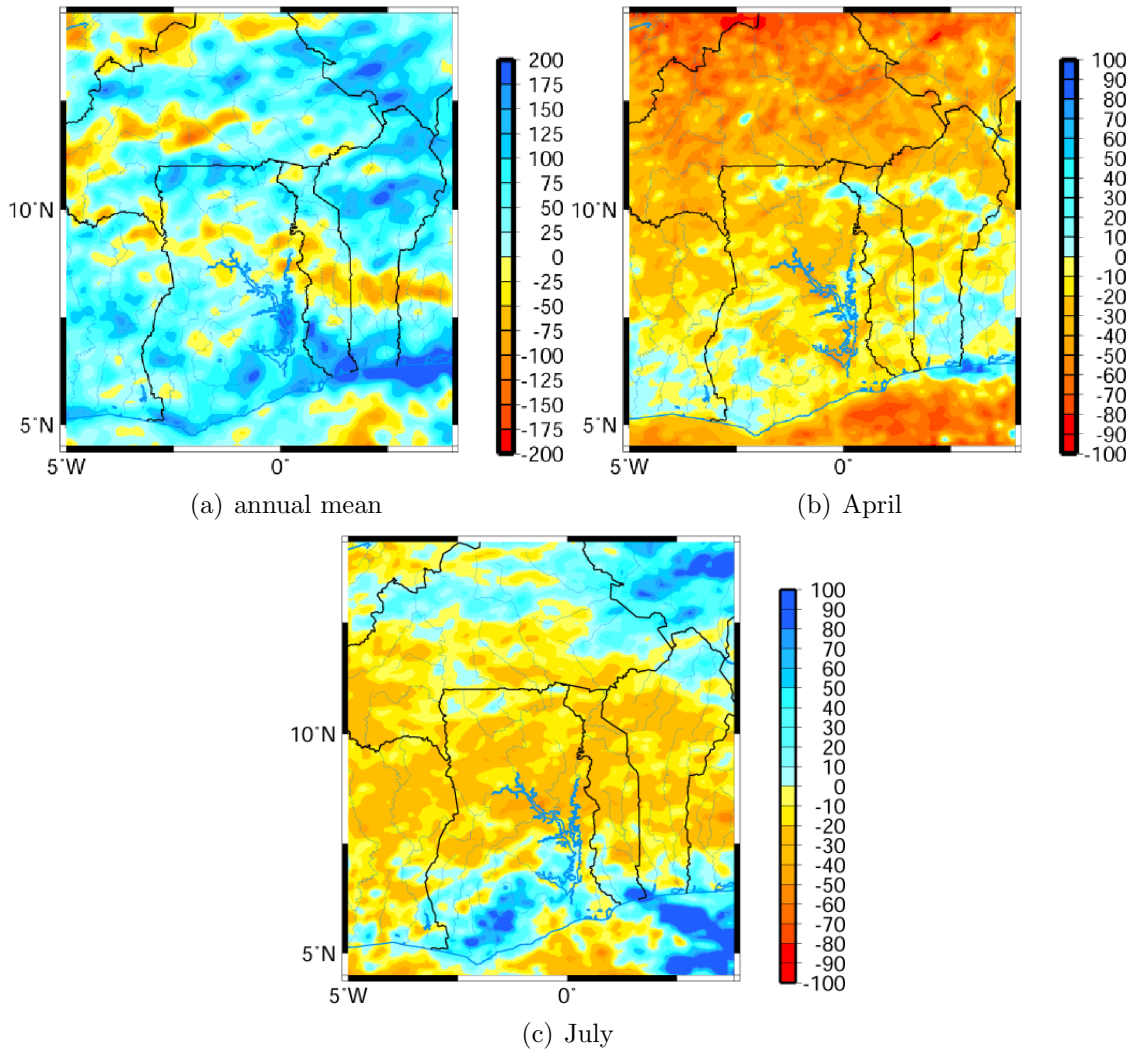

(a) annual mean

(b) April

(c) July

Figure 7.15: Mean precipitation change (2030-2039 vs. 1991-2000) [%], D3

Precipitation The climate change signal is less obvious for precipitation, than for temperature. First, mean annual precipitation change in the Volta region reveals a heterogeneous pattern, ranging from -20 to +50% of precipitation change, depending on the observed region. The highest precipitation decrease can be found in a south-east to north-west directed band that reaches from Nigeria to Ghana and in south-western Burkina Faso. The highest percentage increase is found along the coast from Benin to Nigeria. This is also the strongest signal in absolute values due to its location in the rainfall intense regions of the tropical South. Therefore, the highest amounts of precipitation increase occur in regions bordering the Volta Basin, but not within the basin itself. Absolute precipitation change, spatially averaged over the land area of model domain D3 sums up to a quite small amount of 44.7 mm of precipitation change, which is 5.1% of the spatially averaged annual precipitation. Although the change in annual mean precipitation is small, some changes in the intra-seasonal distribution can be observed for the spatial average.

The precipitation deficit in April that was already detected for the first RCM domain persists in downscaling to the region of the Volta Basin (D3). Figure 7.15 shows a clear

decrease in rainfall over almost the entire D3, leaving a positive anomaly only to the coastal regions of Ivory Coast, the south-western edge of Ghana and southern Benin. In percentage values this precipitation change signal in April, as a mean over the entire model domain, is the strongest signal in the annual cycle, even though this does not mean a lack of large precipitation amounts. Precipitation change for July shows a strong decrease north of the coast (figure 7.15). The month with the strongest increase in rainfall in absolute values is September, as it was already discussed in the large-scale results in section 7.1.1. Figure 7.16

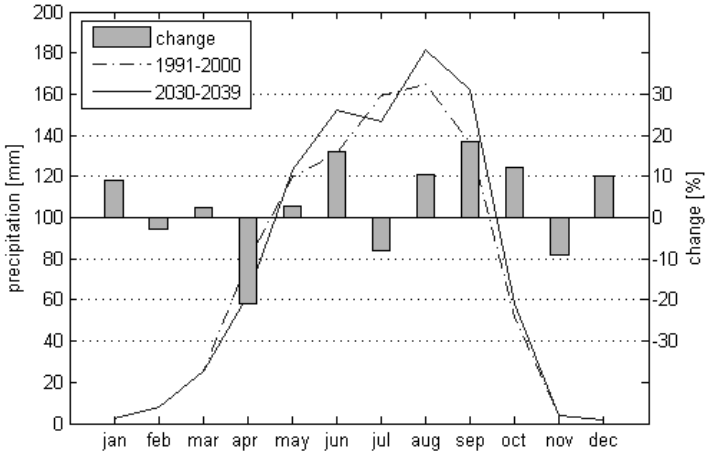

Figure 7.16: Spatially averaged mean monthly precipitation [mm] (1991-2000 and 2030-2039) and precipitation change [%], D3

Table 7.5: Mean monthly and annual precipitation sums (1991-2000 and 2030-2039) [mm], and absolute [mm] and relative [%] changes, D3

	$\overline{1991-2000}$	$\overline{2030-2039}$	ΔP [mm]	ΔP [%]
January	2.3	2.5	0.2	9.2
February	8.0	7.8	-0.2	-2.9
March	25.1	25.7	0.6	2.4
April	79.2	62.6	-16.6	-20.9
May	119.7	123.0	3.3	2.7
June	131.1	152.2	21.1	16.1
July	159.4	146.9	-12.5	-7.9
August	164.6	181.9	17.3	10.5
September	136.5	161.9	25.4	18.6
October	51.9	58.3	6.4	12.4
November	4.2	3.8	-0.4	-9.0
December	1.4	1.6	0.1	10.0
year	883.5	928.1	44.7	5.1

and table 7.5 illustrate the mean annual cycles and changes in all months. The dominant

direction of change during the rainy season (except July) is towards an increase in rainfall in the range of 10 to 20%.

The significance of a precipitation change signal with respect to the regions' simulated climate variability is essential for an assessment of the reliability and uncertainty of a detected signal of change. For this purpose, the signal to noise ratio was examined. Considering both, the Sahel and the Guinea Coast region separately, the only months where we have considerably high levels of reliability ($SN > 1$) are April in the Sahel, and June in the coastal region (figure 7.17). This result also underpins the theory of a dipole pattern of rainfall variability in the two regions.

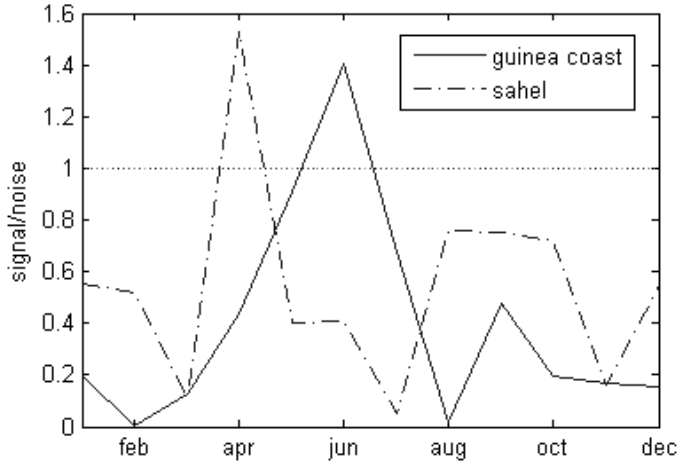

Figure 7.17: Signal to Noise ratio for precipitation change (2030-2039 vs. 1991-2000), D3

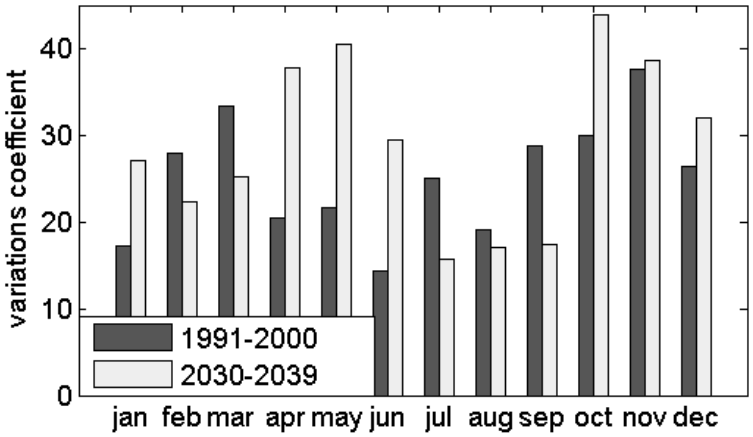

Figure 7.18: Spatially averaged mean monthly variations coefficient of precipitation [-] (1991-2000 and 2030-2039), D3

Inter-annual Variability A comparison of the variations coefficient for the observed present-day climate obtained from long-term station time series ($varc = 11.03\%$) to the

present-day climate simulation ($varc = 18.55\%$) shows an overestimation of the inter-annual variability within the reference state climate conditions. This can not be solely explained through the fact that a 10 years' signal was compared to a much longer time series' signal, because averaging shorter periods of the stations time series yielded similar results.

For the future simulation with respect to the reference state time slice, the monthly values of the variations coefficient show a strong increase in inter-annual variability for the months of April-June (figure 7.18). This leads to the conclusion that a trend towards an increase in inter-annual variability can be detected in the simulations for the early stage of the rainy season.

Onset of the Rainy Season From the afore mentioned fact that we can observe a strong relative change in rainfall at the very beginning of the rainy season in April, the question arises, whether this signal is just due to a reduction in the precipitation amount, which is generally small in that month or whether this signal gives us a hint about a delay in the onset of the rainy season. As defined in section 2.3 the onset dates were calculated

Table 7.6: Mean onset dates and change of the onset date [days]

	Sahel	Coast
Onset $\overline{1991-2000}$ [DOY]	123.6	104.6
Onset $\overline{2030-2039}$ [DOY]	133.3	108.1
Change [days]	9.6	3.5

for the two time slices experiment. Table 7.6 demonstrates, that the mean onset dates for the Sahel and the Guinea coast region are both delayed in the future for 9.6 and 3.5 days respectively. A delay in the onset of the rainy season is found connected with a considerably good signal-to-noise-ratio of 1.8 for the Sahelian region. For the Guinean part the signal-to-noise-ratio is low (0.4). This is a result of the high standard deviation, σ, for the coastal region for the present-day climate scenario.

Aridity Index How changes in the two climatic variables temperature and precipitation collaborate is an even more important question for the hydrological cycle as well as for the livelihood of the population of semi-arid to sub-humid areas, like the Volta Basin.

This is especially true, when rainfall changes are not striking, but a strong increase in temperature might influence the hydrological cycle via an increase in evapotranspiration. As a measure of this impact, the aridity index after DE MARTONNE (1920) was selected, which is defined as

$$dMI = \frac{P}{T+10} \tag{7.3}$$

where P is annual precipitation and T the sum of monthly mean temperature of those months with monthly mean temperature greater then 0°C, divided by 12. For simplicity in the present study this turns out to be the annual mean temperature. From this definition, lower values indicate a higher aridity.

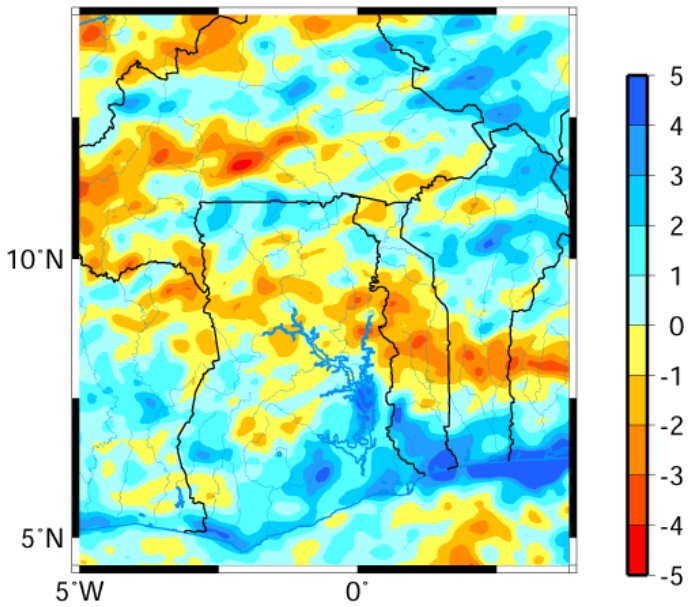

Figure 7.19: Change in the de Martonne aridity index (dMI) [-] (2030-2039 vs. 1991-2000), D3

Following DE MARTONNE (1920), a dMI below 20 indicates the necessity for irrigation in agriculture. If the dMI lies in the range of 20 to 30 irrigation is often undertaken, but not indispensable. Just below a dMI of 10 dry farming is generally not possible. Altogether the values found for present and future climate conditions, as spatially averaged values, are summarized in table 7.7. Though temperature change is striking, the dMI averaged over the

Table 7.7: De Martonne Aridity Index (dMI), D3

	Sahel	Coast
$\overline{1991-2000}$	21.46	22.9
$\overline{2030-2039}$	21.75	23.3

two defined regions (Sahel and Guinea Coast) reveals only a weak signal of change. Even though there is an increase in temperature, the aridity of the region is slightly reduced due to the higher amounts of rainfall. Therefore, from the present study no major changes in aridity can be detected.

Evapotranspiration and Infiltration Excess As MM5 already includes a sophisticated SVAT-model (section 4.2) the the climate change signal that might be detectable in evapotranspiration and infiltration excess will be examined. Both variables are expected to react to changes in rainfall and temperature.

Evapotranspiration The spatial distribution of annual evapotranspiration change indicates a high level of conformity with precipitation change (figure 7.20).

A pronounced band of decrease can be found, following the decrease in rainfall, but spatially more extended. This is due to higher amounts of potential evapotranspiration

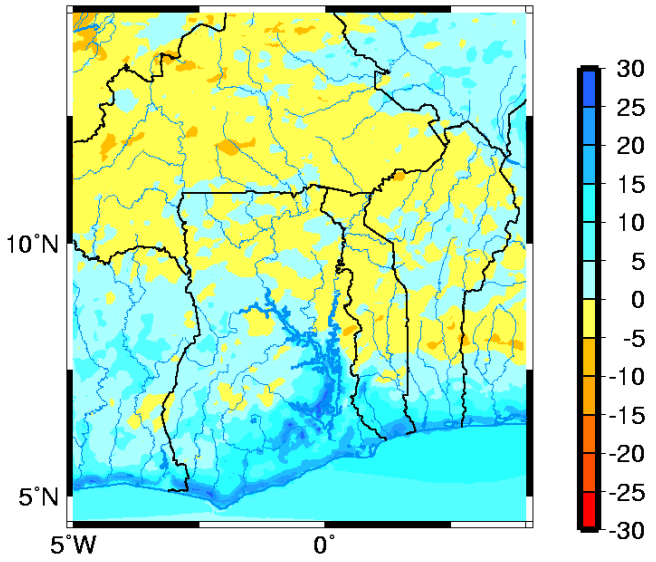

Figure 7.20: Change in evapotranspiration [%] (2030-2039 vs. 1991-2000), D3

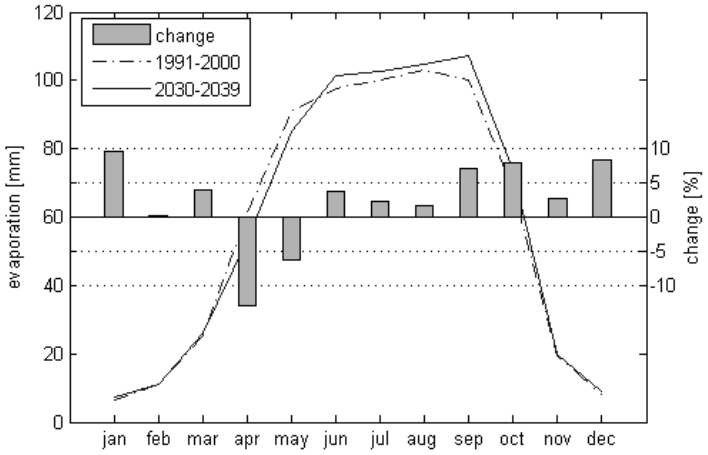

Figure 7.21: Spatially averaged monthly mean evapotranspiration [mm], (1991-2000 and 2030-2039) and evapotranspiration change [%], D3

following an increase in temperature, that affect the change in regions with only poor increases in precipitation especially in the North, where temperature increase is highest.

The monthly change signal (figure 7.21) shows some differences between rainfall and evapotranspiration. A strong decrease in evapotranspiration can be observed in May due to lower soil moisture, following the rainfall deficit of April, even if precipitation shows hardly any change. During the rainy season, where in July rainfall decreases, evapotranspiration shows an increase, due to the potential evapotranspiration increase through higher temperature and sufficient availability of moisture. In November a similar signal can be observed. Generally the magnitude of percentage, as well as absolute change in evapotranspiration is smaller than that in precipitation.

Infiltration Excess Similar to the results on evapotranspiration, infiltration excess shows a spatially distributed signal of change that is strongly determined by the signal in rainfall (figure 7.22). Figure 7.23 indicates that the percentage changes in infiltration excess in most months show the same sign as precipitation changes, but the relative signal is stronger in magnitude. Only in November, in the early dry season, does infiltration excess increase, despite a decrease in rainfall. This spatially averaged signal is introduced through a small region along the coast, where soil is still saturated after the surplus rainfall in October and so, even if less precipitation is observed in November a higher percentage of water can not infiltrate.

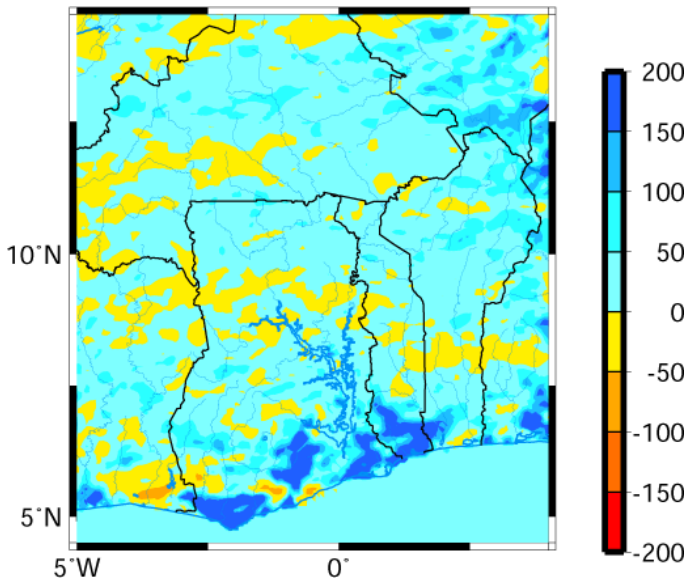

Figure 7.22: Change in infiltration excess [%] (2030-2039 vs. 1991-2000), D3

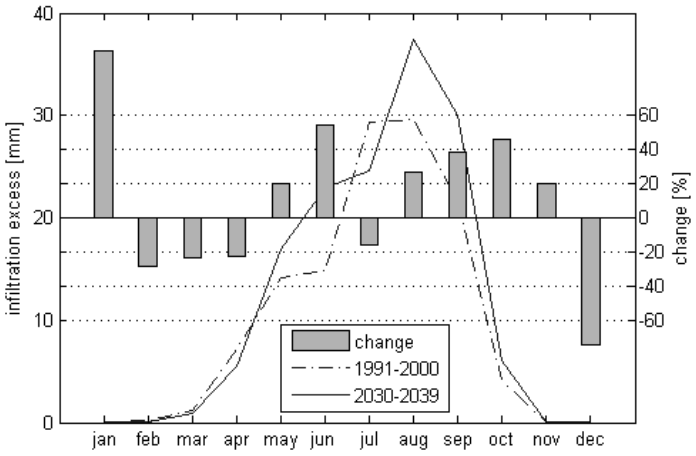

Figure 7.23: Spatially averaged monthly mean infiltration excess [mm], (1991-2000 and 2030-2039) and change in infiltration excess [%], D3

Summary - Climate Change in the Volta Basin Whereas temperature change shows a clear signal of increase in the future simulations, rainfall does not. Changes in precipitation are on one hand small in average and on the other hand only two months, April for the Sahel region and June for the Guinea Coast region, turned out to have a distinct signal-to-noise ratio. Therefore, these signals can be traced back to inter-decadal or even lower frequency variability or climate change. For the other months, the precipitation change signal, simulated by MM5/ECHAM4 lies within inter-annual variability and is consequently to be seen as such. The onset of the rains in the Volta region shows a decrease, with a distinct signal to noise ratio, for the Sahel. Inter-annual variability increases at the beginning and in the early stage of the rainy season. No major changes could be detected for the de Martonne aridity index, that considers the influence of temperature, as well as precipitation. Evapotranspiration shows a change in the future simulation that can only be explained by rainfall and temperature variabilities. For infiltration excess, rainfall turned out to be the most important variable, but also soil moisture, and therefore previous rainfall events, have to be taken into consideration. The magnitude of percentage change of infiltration excess exceeds that of rainfall. For relative evapotranspiration change, the magnitude is smaller than for precipitation.

7.2 Terrestrial Hydrological Response to Regional Climate Change

Due to the increase in temperature and consequently in potential evaporation, as well as due to the spatial and temporal heterogeneity of the simulated climate change, an investigation of the regional climate change impact on hydrology is ingenious, even though the rainfall change signal in the Volta Basin is rather small. The variables that are analyzed and presented in the following are:

etp	potential evaporation
etr	real evapotranspiration
gwn	groundwater recharge
prec	precipitation
qdir	direct runoff/infiltration excess
qifl	interflow+baseflow
qrout	routed river runoff
qtot	total runoff (=qdir+qifl)
soilm	soil moisture

Additionally the runoff regime was considered. For this purpose, the normalized frequency distribution of daily runoff values was investigated for possible future changes.

Annual Mean Hydrological Response in the Volta Basin

Runoff and Evaporation As expected, discharge change from the present-day coupled simulation (1991-2000) to the future scenario coupled simulation (2030-2039) does not show a linear response to changes in precipitation. Figure 7.24 reveals, that most of the

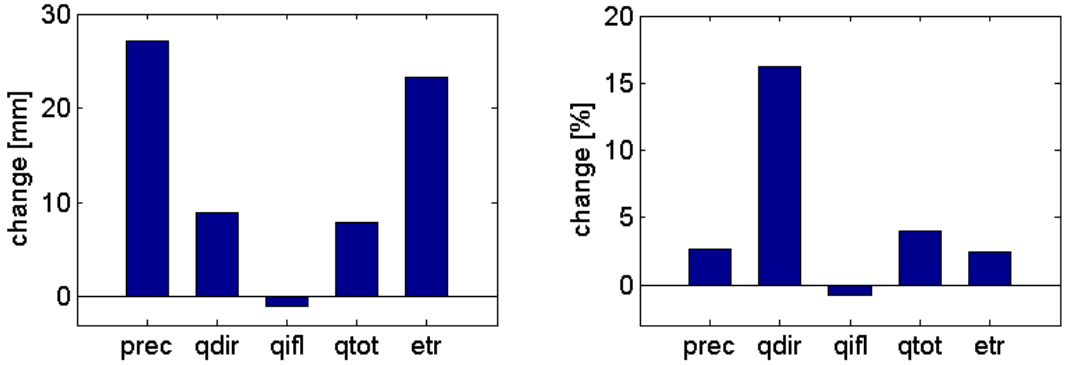

Figure 7.24: Changes in the most important hydrological variables, left: Absolute values [mm], right: Relative to (1991-2000) [%]

surplus rainfall reaching the Volta Basin goes off as increased evapotranspiration. This is easily explained by higher temperatures in the future climate scenario, that lead to higher potential evaporation and, in case of sufficient soil moisture availability, to an increase in real evapotranspiration. Therefore only a small amount of surplus rainfall runs off as additional direct runoff and interflow.

Interflow shows hardly any change, only a small negative deviation. Due to the small amount of direct runoff in general, and the sensitive reaction towards rainfall events in case of high soil saturation, the percentage change is largest for direct runoff, with a change of 16.5%.

Annual Cycle of Hydrological Response in the Volta Basin

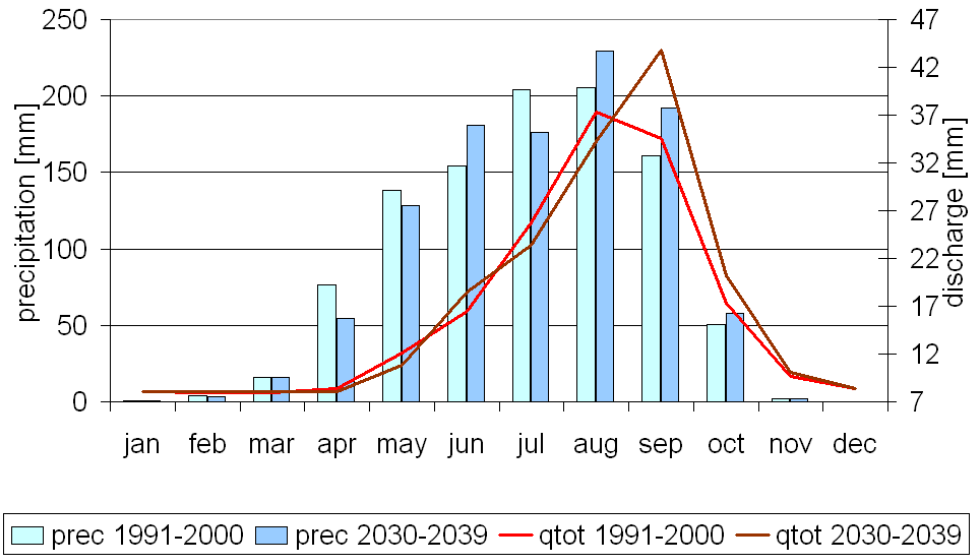

Figure 7.25: Monthly amounts of precipitation and discharge (1991-2000 and 2030-2039) [mm]

Rainfall-Runoff Response The annual cycle of runoff with respect to climate change, first of all shows a shift in the month of discharge maximum from August to September (figure 7.25). Where runoff in August is only slightly lower for 2030-2039 (7.3 mm less than in 1991-2000), in September it is higher for the simulated future scenario (26.1 mm plus) due to the strong increase in precipitation. This can be explained by the finding, that in the present-day time slice runoff peaks in August for half of the years, in September for the rest of the years. In contrast, in the future simulation all years show a peak runoff in September. The respective annual rainfall peak occurs in August in 7 out of 10 years in the 2030-2039 time slice, whereas in the present-day simulation it is more variable, with 3 years showing peak rainfall in July and 5 in August.

In the reference state simulation, the discharge curve shows a direct response to precipitation, with the highest amounts of discharge and rainfall in August and the second highest in September. For the future climate scenario, the rainfall maximum is found in August, whereas the discharge maximum occurs in September.

As indicated in section 7.1.2 the large percentage change in precipitation in the Volta Basin in April does not show a corresponding signal in river runoff.

Impact on Evapotranspiration and Soil Moisture Figure 7.26 illustrates the sensitivities of runoff, evapotranspiration and soil moisture to climate change for the total

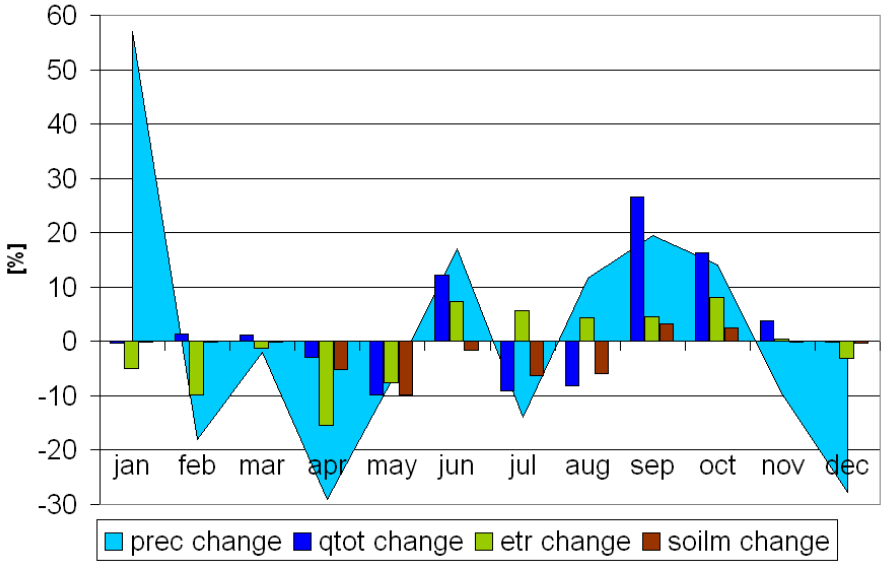

Figure 7.26: Monthly changes in precipitation, runoff, evapotranspiration and soil moisture [%] (2030-2039 vs. 1991-2000)

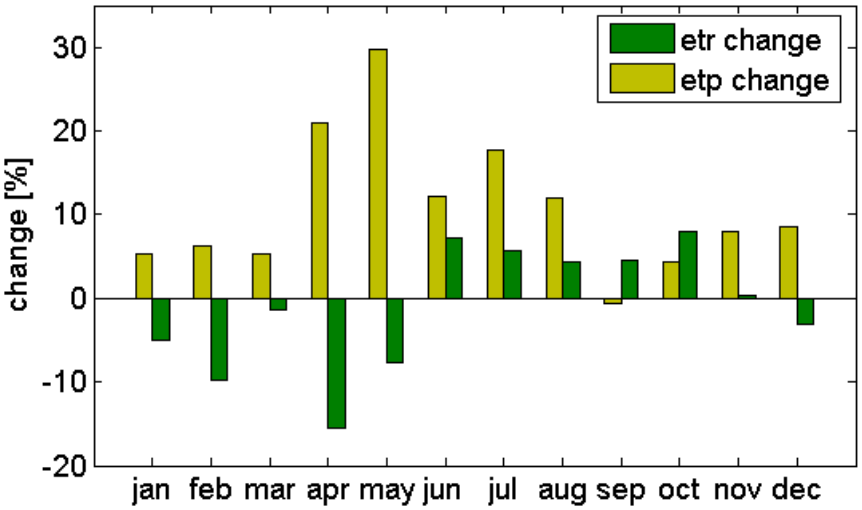

Figure 7.27: Monthly values of real and potential evapotranspiration (1991-2000 and 2030-2039)

catchment. The small response signal in April can be easily explained through the small rainfall deficit in terms of rainfall amount and the extremely dry soil at the end of the long dry season. Due to these factors, the small amount of surplus rainfall in the present-day reference state simulation (1991-2000) is most likely infiltrated and leads to a higher soil moisture amount in April in the present-day simulation compared to the future run. Therefore, the soil moisture deficit in the future time slice is enhanced by higher potential evaporation, due to an increase in temperature. This holds true for May, where in contrast to the third MM5 model domain, where in total a small increase in precipitation could be observed, for the region of the Volta Basin rainfall decreases by almost half of the amount of April. In June a clear increase in discharge follows the increase in precipitation. In July the opposite is observed. In both months, the percentage change in rainfall exceeds the change in river runoff. In August, discharge shows a decrease though rainfall increases, whereas in September both signals show an increase, leading to a delay in the peak runoff, with respect to the peak rainfall amount. In November, an increase in runoff together with a decrease in discharge can be observed. September and October uniformly show an increase of both variables.

These features can be explained through an additional consideration of soil moisture and evapotranspiration. Soil moisture reveals a characteristics that is determined by past rainfall amounts and evapotranspiration.

For the variability of the runoff response signal, rainfall is more important, as evapotranspiration increases in all months, from June to November, in which water availability is sufficient, and does not show a strong variability (figure 7.27). The months with the highest increase in potential evaporation, April and May, show a decrease in real evapotranspiration due to the lack of soil moisture. The delay in the runoff maximum with respect to rainfall in the future simulation can be explained by the soil moisture deficit of August, that leads to a decrease in discharge generation despite a surplus of precipitation reaching the basin. This means that the part of the additional rainfall that is not evapotranspirated is infiltrated. In September, though potential evaporation slightly decreases, real evapotranspiration shows an increase because moisture availability is higher in the future scenario than in the present-day time slice due to higher rainfall amounts.

Therefore, in September a large amount of water can not infiltrate and runs off, dominantly as direct runoff.

There are two reasons for the increase in precipitation in August not leading to an increase in runoff. First, from the rainfall deficit in July soil moisture is lower and therefore a higher amount of rainfall infiltrates in August. Second, evapotranspiration increase takes away most of the surplus rainfall. In some regions, it is even larger than rainfall change. The opposite signal in November can be explained by higher soil moisture amounts, resulting from the increase in precipitation in September and October, leading to a smaller amount of infiltrated rainwater. Consequently, even though an increase in evapotranspiration can be observed, river runoff increases, despite a decrease in rainfall.

Signal to Noise The signal to noise ratio was also analyzed for selected output variables of the hydrological model. In table 7.8 it is shown, that the simulated annual mean climate change signal, lies clearly within simulated inter-annual variability. The annual cycle of the SN ratio for precipitation (here in comparison to chapter 7 only the Volta Basin is

Table 7.8: Signal to Noise ratio for selected hydrological variables

	prec	etr	qtot	qdir	qifl	soilm
January	0.49	0.09	0.17	0.48	0.3	0.1
February	0.21	0.18	1.05	2.48	0.7	0.08
March	0.03	0.07	0.97	2.18	1.04	0.09
April	1.14	0.5	0.7	0.46	0.74	0.93
May	0.28	0.39	0.35	0.27	0.41	0.61
June	1.0	1.53	0.43	0.69	0.18	0.11
July	0.48	0.7	0.23	0.16	0.29	0.38
August	0.55	0.47	0.18	0.75	0.45	0.32
September	0.66	0.52	0.55	0.7	0.36	0.17
October	0.41	0.28	0.42	0.54	0.33	0.12
November	0.09	0.01	0.34	0.59	0.19	0.02
December	0.22	0.09	0.01	0.26	0.11	0.1
year	0.16	0.33	0.15	0.35	0.05	0.19

considered), evaporation and runoff is illustrated in figure 7.28. Total runoff only exceeds a SN of 1 in February, which is not a significant signal due to the small amounts of runoff generally observed in the dry season. Precipitation, like for the regional climate model domain D3, also shows a $SN \geq 1$ in April and June for the basin. Due to the increase in rainfall in June, evapotranspiration shows a signal higher than inter-annual variability in this month. The monthly values for soil moisture, direct runoff and interflow are additionally summarized in table 7.8.

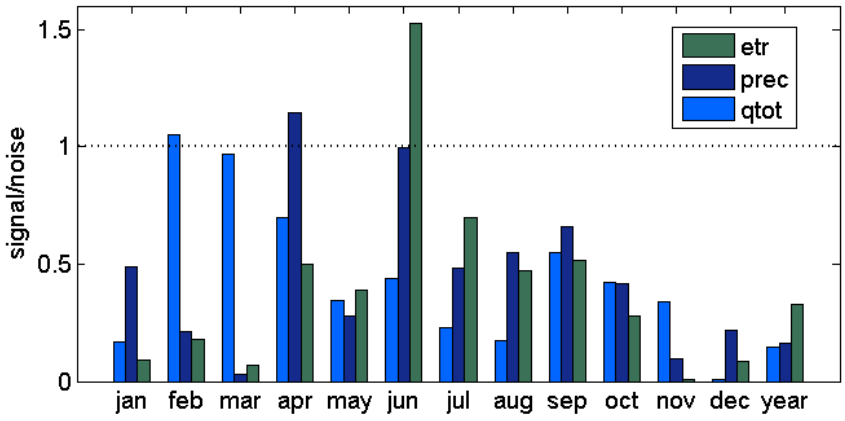

Figure 7.28: Monthly values of SN ratio (1991-2000 and 2030-2039)

Inter-annual Variability According to the variations coefficient, the inter-annual variability of total runoff was additionally considered (figure 7.29). Like for precipitation, the

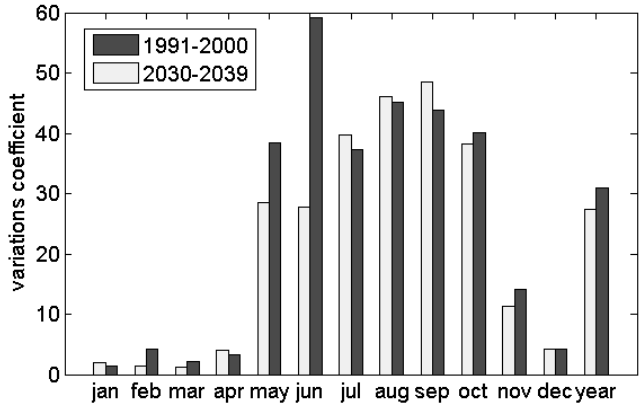

Figure 7.29: Monthly variations coefficient for runoff (1991-2000 and 2030-2039) [%]

inter-annual variability increases in the early rainy season, but no increase can be observed for April.

Annual Mean Changes for Selected Subcatchments

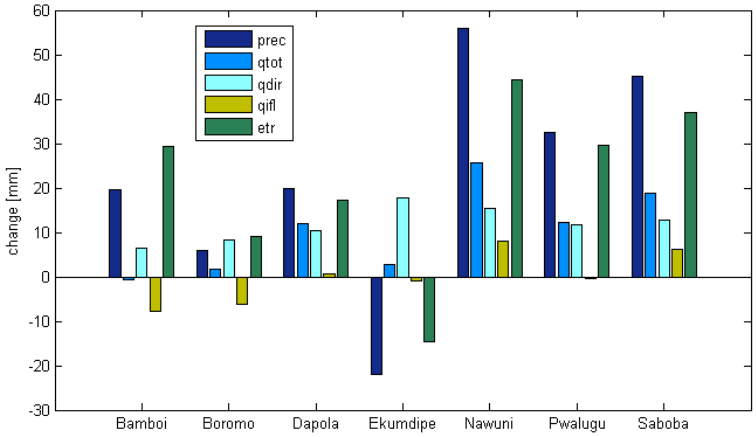

Figure 7.30: Changes in precipitation, evapotranspiration and discharge, selected gauges [mm]

Rainfall-Runoff Response Tables 7.9 and 7.10 summarize the spatial variability of the change signal in hydrology for some important hydrological variables. The spatially heterogeneous rainfall-runoff response is clearly shown in figures 7.30 and 7.31 for selected subcatchments. While for all subcatchments, the percentage changes in runoff and precipitation differ, in most of them at least the algebraic sign of change is the same. This is not the case for the gauges of Ekumdipe and Bamboi. For Bamboi, an increase in precipitation goes along with a decrease in discharge. This can be explained through evapotranspiration

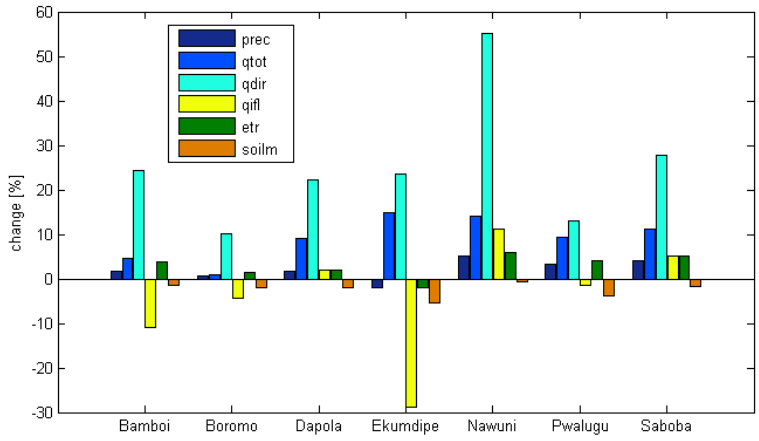

Figure 7.31: Changes in precipitation, evapotranspiration and discharge, selected gauges [%]

change exceeding rainfall change. Despite a decrease of rainfall in the subcatchment area of Ekumdipe, in the Lake Volta region, discharge increases.

Frequency Distribution The normalized frequencies of daily runoff values show only minor changes within the future climate scenario, with respect to the reference run. Figures 7.32 and 7.33 demonstrate the only two gauges, where distinct differences occur. These are the gauges Saboba on the Oti river and Pwalugu on the White Volta. In both examples, small runoff amounts are slightly more frequent in the simulated future climate.

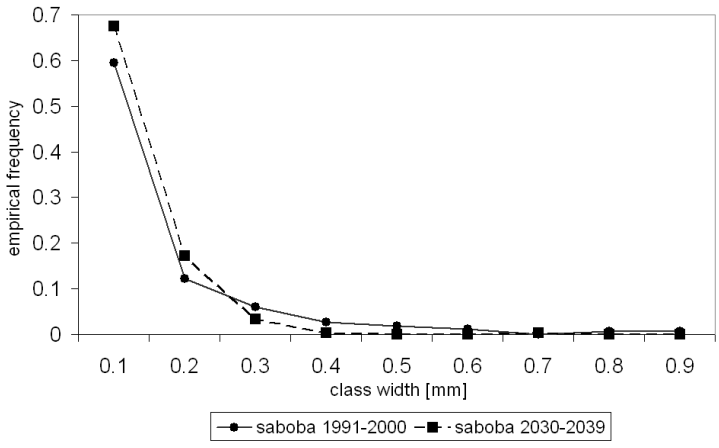

Figure 7.32: Normalized frequency distribution of daily runoff values [mm] (1991-2000 and 2030-2039), Saboba

Runoff Coefficient Figure 7.34 reveals, that no large changes in the mean runoff regime can be observed for the selected subcatchments. The higher values in the future climate

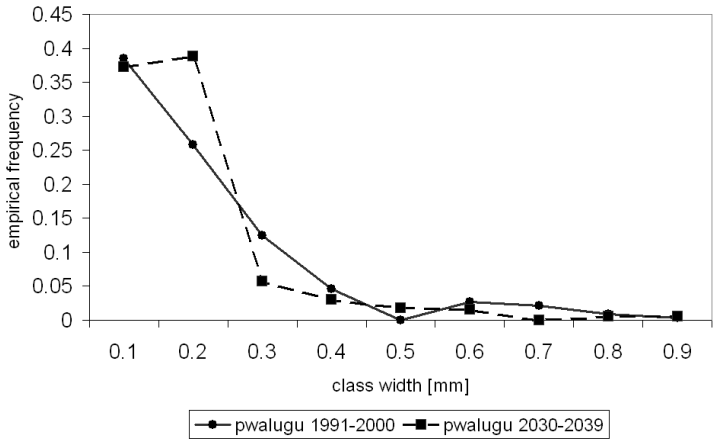

Figure 7.33: Normalized frequency distribution of daily runoff values [mm] (1991-2000 and 2030-2039), Pwalugu

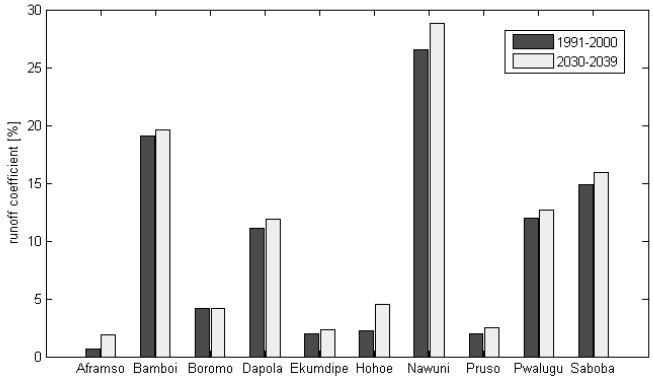

Figure 7.34: Runoff coefficient [-] for selected gauges (1991-2000 vs. 2030-2039)

scenario run were found to be due to the increase in direct runoff especially in the rainfall intense month of September.

Table 7.9: Annual means and changes of most important hydrological variables, selected gauges

	Aframso	Bamboi	Boromo	Dapola	Ekumdipe
prec 1991-2000	930.0	1086.3	937.4	1125.1	1044.3
prec 2030-2039	968.2	1105.8	943.2	1144.9	1022.4
prec change [mm]	38.2	19.5	5.8	19.8	-21.9
prec change [%]	4.1	1.8	0.6	1.8	-2.1
qtot 1991-2000	8.0	100.4	219.1	85.5	24.9
qtot 2030-2039	21.9	99.6	220.9	97.3	27.7
qtot change [mm]	13.8	-0.8	1.8	11.9	2.8
qtot change [%]	172.6	-0.8	0.8	13.9	11.1
qdir 1991-2000	4.9	26.7	81.4	46.3	17.5
qdir 2030-2039	16.7	33.2	89.6	56.7	21.6
qdir change [mm]	11.7	6.5	8.2	10.4	4.1
qdir change [%]	238.9	24.2	10.1	22.3	23.5
qifl 1991-2000	1.3	70.3	136.2	36.6	3.5
qifl 2030-2039	1.9	62.5	130.1	37.4	2.5
qifl change [mm]	0.5	-7.7	-6.1	0.8	-1.0
qifl change [%]	38.9	-11.0	-4.5	2.0	-28.7
etr 1991-2000	690.5	749.8	680.2	835.1	776.6
etr 2030-2039	719.7	779.0	689.2	852.3	761.9
etr change [mm]	29.2	29.2	9.0	17.3	-14.7
etr change [%]	4.2	3.9	1.3	2.1	-1.9
soilm 1991-2000	0.3	0.31	0.37	0.32	0.27
soilm 2030-2039	0.31	0.31	0.36	0.32	0.26
soilm change [%]	2.0	-1.5	-1.9	-1.9	-5.3

Table 7.10: Annual means and changes of most important hydrological variables, selected gauges

	Hohoe	Nawuni	Pruso	Pwalugu	Saboba
prec 1991-2000	857.7	1093.9	930.5	1019.2	1134.0
prec 2030-2039	980.7	1149.8	950.2	1051.6	1179.1
prec change [mm]	123.0	55.9	19.7	32.4	45.1
prec change [%]	14.3	5.1	2.1	3.2	4.0
qtot 1991-2000	21.7	105.1	20.2	118.4	174.8
qtot 2030-2039	47.3	128.6	26.9	130.5	193.7
qtot change [mm]	25.7	23.5	6.7	12.1	18.9
qtot change [%]	118.5	22.3	33.0	10.2	10.8
qdir 1991-2000	7.5	28.1	15.5	91.0	45.8
qdir 2030-2039	25.2	43.6	19.5	102.8	58.5
qdir change [mm]	17.7	15.5	4.1	11.8	12.7
qdir change [%]	237.6	55.1	26.3	13.0	27.7
qifl 1991-2000	12.1	72.1	3.2	30.5	122.5
qifl 2030-2039	19.4	80.2	4.3	30.1	128.7
qifl change [mm]	7.4	8.0	1.1	-0.4	6.2
qifl change [%]	61.1	11.1	34.4	-1.5	5.1
etr 1991-2000	631.4	755.5	677.7	744.4	740.0
etr 2030-2039	731.8	800.0	695.4	774.1	777.1
etr change [mm]	100.4	44.4	17.7	29.7	37.1
etr change [%]	15.9	5.9	2.6	4.0	5.1
soilm 1991-2000	0.35	0.25	0.31	0.35	0.29
soilm 2030-2039	0.36	0.25	0.31	0.34	0.29
soilm change [%]	3.0	-0.7	1.2	-3.7	-1.6

Summary - Coupled Simulations The analysis of the coupled climate-hydrology simulations shows a very heterogeneous response of river runoff to changes in climate variables. A small increase in rainfall was observed, that lead to an increase in discharge. Nevertheless, most of the rainfall surplus was found to evaporate, due to an increase in temperature and consequently in potential evaporation. The largest percentage change was observed for infiltration excess (direct runoff), but was strongly dependent on actual and past rainfall intensities, soil moisture and evapotranspiration. For the different gauges, varying response signals could be delineated, but still explainable through the most important variables of the hydrological cycle. The signal to noise ratio is weak for all considered hydrological variables and the change signal seldom exceeds inter-annual variability. Hardly any change could be observed for the mean flow regime, expressed through runoff coefficient and normalized frequency distribution.

It can be concluded, that the physically based model WaSiM proved its capability to reproduce explainable results for the different hydrological variables and their interactions.

7.3 Discussion of Simulated Climate and Hydrology Trends

A question to focus on is whether the detected change signal indicates a climate change within the chosen experiment, or whether it is to be seen as the stamping of local climate variability. Also to be considered is the suitability of the modelling system to be used for an impact analysis.

The dynamical downscaling approach offers the possibility to represent changes in the dynamical regime, as far as the responsible processes can be properly simulated by MM5.

In addition to the uncertainty that lies within the modelling cascade, there is the question of judgment of the simulated change signal within the bounds of the chosen experiment. This means: If we take this modelling approach as one state of future climate, how significant is the simulated climate change signal, with respect to the variability of the climate within our experiment?

Therefore, the signal to noise ratio was calculated, that means, the climate change signal was considered with respect to the simulated present-day climate variability.

Simulated temperature change shows a distinct signal of an increase for the entire region, with a high SN value, leaving no doubt about a climate change signal in temperature within the experiment.

For the entire West Africa a small mean increase in precipitation could be detected, with a weak SN value, and therefore, the signal is found to lie within the range of climate variability. Similar results were already found by Kamga (2000). Separately considering the Sahel and the Guinea Coast region, reveals a higher signal with respect to variability in the Sahel region. Therefore, the Sahel turned out to be an area of higher sensitivity to climate change in the simulations. Temporally the most significant signal can be found in April in the Sahelian part of the Volta Basin. In June a high signal to noise value is detected along the Guinea coast. A signal that is still within the range of climate variability, but large in the sense of absolute change, is the increase in precipitation in September over all of the Volta basin, as well as for entire West Africa.

The change signal in rainfall is clearly still lying within simulated climate variability for most months. In some cases it is larger than inter-annual variability, and therefore indicates a signal of lower frequency variability or even climate change.

Additionally a delay in the onset of the rainy season was detected in the simulated future climate, as well as an increasing inter-annual variability of precipitation in the early stage of the rainy season. The signal of the delay in the onset of the rainy season showed a larger signal to noise ratio for the Sahel. This result is in conformity with present trend studies (Neumann et al., 2005; Laux et al., 2005), which show a decrease in rainfall in the early rainy season, as well as a delay in the onset date.

The decrease in rainfall in April and the increase in September could be linked to a southward and northward displacement, respectively, of the ITD. Furthermore, some rainfall change signals could be explained by jet stream dynamics. This demonstrates the ability of MM5 to simulate the regional dynamical features and their sensitivity to climate change and variability.

The collaboration of rainfall and temperature change signal is of major concern for water availability within the region. It was demonstrated that aridity, following the de Martonne index, does not show a large change. Therefore, from this experiment no change in agricultural activities, due to climate change, is expected.

The runoff response is weak in April, the month with the most significant change signal in rainfall, due to generally low soil moisture conditions. Runoff showed only a strong signal in the month with the largest absolute rainfall increase, in September, where direct runoff strongly increases due to high precipitation amounts in combination with high soil moisture in the late rainy season. Nevertheless, the change signal in land-surface hydrology lies predominantly within the range of inter-annual variability.

Generally, a highly nonlinear and highly sensitive response to changing meteorological conditions was found in the WaSiM results. Furthermore, the hydrological response to the regional climate change signal, simulated by WaSiM turned out to be clearly explainable by the different hydrological model outputs (section 7.2).

Therefore WaSiM proved its ability to reasonably simulate processes of land-surface and sub-surface hydrology and its sensitivity to changing climatic conditions.

Chapter 8

Summary and Conclusions

The livelihood of the population of the semi-arid to sub-humid environment of the Volta Basin is highly vulnerable to changing climate conditions. Therefore, if an investigation of the impact of changing atmospheric conditions on surface and subsurface hydrology in this region on basis of environmental modelling is aimed at, a suitable model cascade is needed

A dynamical regional downscaling of ECHAM4 data (scenario: IS92a) for two 10-years time slices (1991-2000) and (2030-2039) was performed with the mesoscale meteorological model MM5, down to a resolution of 9 km and coupled one-way to the physically based, distributed hydrological model WaSiM in a resolution of 1km, after the separate validation and evaluation of the performance of all contributing models.

Despite some weakness in simulating coastal rainfall with MM5 for the region of the Volta Basin, simulated temperature, as well as rainfall was of sufficient accuracy for both reanalysis runs and regional climate simulations.

Additionally, it can be concluded, that the regional climate model MM5 is suitable for simulating the variability of the West African dynamics system. The known dipole structure of rainfall variability could be evaluated for this experiment. Furthermore, the major dynamic features (TEJ, AEJ and ITD displacement) that are important for the variability of the West Africa rainfall regime are represented within the MM5 simulations.

The hydrological model WaSiM also demonstrated its good performance in representing the hydrology of the Volta Basin, and the suitability to react sensitively towards changes in the driving meteorological conditions.

This modelling experiment has to be considered as one out of an uncountable number of possible scenarios of future climate. Therefore, when talking about climate change results, with respect to the simulated absolute values, one always has to be aware of the large number of uncertainties within the modelling cascade.

Despite these general constraints, it was possible to extract results of importance for decision makers in West Africa and the Volta Basin from the regional climate simulations.

As a central topic within this study, the climate change signal for several variables was examined with respect to the respective simulated inter-annual variability via the signal to noise ratio, in order to determine whether the modelled change signal is to be seen as a clear sign of simulated climate change, or if it lies within the range of the regions' inter-annual variability.

The simulated temperature change clearly shows an increase of around 1.2-1.3°C with a high signal to noise ratio, that is larger, but similar in trend to the observed trend of

the last century, globally, as well as in West Africa. Annual rainfall change in the regional climate simulations shows an increase of about 5% in the larger Volta region. Furthermore, the precipitation change is spatially highly heterogeneous, ranging form -20% to +50%. In contrast to the temperature change signal, this precipitation increase is not in agreement with the observed long-term trend. The observed precipitation trend for the Volta Basin is not highly significant, but is rather directed towards a decrease in rainfall, as it is observed in most of West Africa for the last century. This disagreement between simulations and observed trend signal shows the complexity of the monsoonal system of West Africa and is most likely due to the lack of the influence of land-surface changes in the climate simulations. The signal to noise ratio is in addition only remarkable (> 1) for annual rainfall in the Sahelian part of the basin (north of 10°N) and particularly for the decrease in precipitation at the beginning of the rainy season, in April. The rainfall decrease in April was found to be connected to a southward displacement of the ITD.

This decrease in rainfall is furthermore not only an indicator of a decrease in rainfall amounts at the beginning of the rainy season, but it is also connected to a delay in the onset of the rains of around 10 days in the Sahel. Also worth mentioning is the increase in inter-annual variability that was simulated for the early stage of the rainy season. The simulations did not show strong changes in aridity, expressed through the de Martonne aridity index, which is basically dependent on annual values of temperature and precipitation. From this point of view no major changes have to occur in agricultural activities. Nevertheless, the signal of a higher inter-annual rainfall variability in the early stage of the rainy season, as well as the delay in the onset of the rainy season increases the vulnerability of local farming activities, even if annual rainfall amounts do not change significantly.

No strong changes, in terms of signal to noise ratio are simulated for river runoff and infiltration excess. This is caused by the small increase in rainfall amounts, and the fact, that most of the surplus of rainfall evaporates, due to the increased potential evaporation with increasing temperatures. Therefore, future activities in agriculture, like intensification of irrigation, that might follow the increasing population pressure, but also competing water use sectors like households and industries do meet similar conditions than nowadays. From that point of view, it isn't climate change that will put additional stress on water availability, but industrialization and an intensification of agricultural activities.

Looking further into the future, the distinct signal of a temperature increase has to be considered, because a warming climate will nevertheless put additional stresses on water resources, whether or not future rainfall is significantly altered.

Outlook For future RCM simulations within the region it is advisable to consider longer time slices after the year 2050, when a stronger change signal is observed and to achieve a representative time slice length for mean climate conditions in an area with high inter-decadal variability. The increase in variability of rainfall for the simulated future time slice and the decrease of rainfall at the onset of the rainy season are signals that are worth pursuing in future studies, for the 10-year scenario gives a hint, but is to short to draw final conclusions.

Another future task would be to improve the representation of SST in MM5, through a coupling of a mesoscale ocean model, or higher resolved AOGCM input, to achieve a better model performance of the coastal meteorology.

In addition, the impact on regional climate in the Volta Basin is not only determined by global climate change, but also by changes in regional land-surface conditions and the respective feedback mechanisms. Therefore land-use change studies for both models would be interesting to estimate the impact of landuse change on climate and hydrology, with or without increasing greenhouse gases.

Furthermore, the coupling of the regional climate model to a dynamical vegetation model could be useful, to account for dynamic land-use changes following climate change and giving an additional forcing to the climate dynamics through feedback mechanisms. For a higher degree of consistency between the atmospheric and the hydrological part of the study a 2-way coupling of a hydrological model to the atmospheric part of MM5 could be also considered in order to combine the advantages of both models.

Bibliography

Adams W. M., Goudie A. S. & Orme A. R. (1996): The Physical Geography of Africa; Oxford University Press.

Agyare W. A. (2004): Soil characterization and modeling of spatial distribution of saturated hydraulic conductivity at two sites in the Volta Basin of Ghana; Ecology and Development Series No. 17; Cuvillier Verlag Göttingen.

Ajayi A. E. (2004): Surface runoff and infiltration processes in the Volta Basin, West Africa: Observation and modeling; Ecology and Development Series No. 18; Cuvillier Verlag Göttingen.

Amani A. (2001): Assessment of precipitation and ressources variability across the Sahelian region; pp. 67–72; In: Report of the International Workshop on Africa's Water Resources, Nairobi, 26-30 October 1999 (BAHC).

Amani A., Afouda A., Mayga M., Mahe G., Neguetora M., Ankomah M. O., Paturel J. E., Sigha L. & Sighoumnou D. (2002): West and Central Africa (AOC); pp. 53–60; FRIEND report Chapter 5.

Amisigo B. A.: (2005): Modelling riverflow in the Volta Basin of West Africa: A data-driven framework; PhD thesis; University of Delft.

Andreini M., van de Giesen N., van Edig A., Fosu M. & Andah W. (2000): Volta Basin Water Balance; ZEF - discussion papers on development policy 21; Center for Development Research (ZEF), Bonn.

Arnell N. W., Hudson D. A. & Jones R. G. (2003): Climate change scenarios from a regional climate model: Estimating change in runoff in southern Africa; *Journal of Geophysical Research*; Vol. 108(D16): pp. ACL 9 1–17.

Ashrit R. G., Kumar K. R. & Kumar K. K. (2001): ENSO-Monsoon relationshipos in a greenhouse warming scenario; *Geophysical Research Letters*; Vol. 28: pp. 1727–1730.

Asselin R. (1972): Frequency filter for time integrations; *Monthly Weather Review*; Vol. 100: pp. 487–490.

Bader J.: (2005): The role of the tropical indian ocean in global climate; PhD thesis; University Hamburg.

Bastidas L. A., Gupta H. V. & Sorooshian S. (2002): Mathematical Models of Large Watershed Hydrology; Water Resources Publications, LLC.

Bengtsson L. (2003): Climate modelling and prediction -Achievements and challanges-; (www.clivar.org).

Bergstroem S. & Forsman A. (1973): Development of a conceptual deterministic rainfall-runoff model; *Nordic Hydrology*; Vol. 4: pp. 147–170.

Betts A. K. (1986): A new convective adjustment scheme. Part I: Observational and theoretical basis; *Quarterly Journal of the Royal Meteorological Society*; Vol. 112: pp. 677–691.

Beven K. (1989): Changing ideas in hydrology - the case of physically-based models; *Journal of Hydrology*; Vol. 105: pp. 157–172.

Bliefert C. (1997): Umweltchemie; VCH Verlagsgesellschaft mbH.

Bormann H. & Diekkrüger B. (2003): Possibility and limitations of regional hydrological models applied within an environmental change study in Benin (West Africa); *Physics and Chemistry of the Earth*; Vol. 28: pp. 1323–1332.

Bormann H. & Diekkrüger B. (2004): A conceptual, regional hydrological model for Benin (West Africa): Validation, uncertainty assessment and assessment of applicability for environmental change analysis; *Physics and Chemistry of the Earth*; Vol. 29: pp. 759–768.

Bougeault P. (1983): A non-reflective upper boundary condition for limited-height hydrostatic models; *Monthly Weather Review*; Vol. 111: pp. 420–429.

Bro C. (2001): État des lieux des ressources en eau du Burkina Faso et de leur cadre de gestion; Ministere de l'environnement et de l'eau, Burkina Faso.

Brutsaert W. (1982): Evaporation into the Atmosphere; Kluwer Academic Publishers, Dordrecht.

Burpee R. W. (1972): The origin and structure of easterly waves in the lower troposphere of North Africa; *Journal of the Atmospheric Sciences*; Vol. 29: pp. 77–90.

Bárdossy A. (2003): Hydrologie III, Modellierung; University Stuttgart.

Charney J. G. (1975): Dynamics of desert and drought in the Sahel; *Quarterly Journal of the Royal Meteorological Society*; Vol. 101: pp. 193–202.

Chevallier P. & Planchon O. (1993): Hydrological processes in a small humid savanna basin (Ivory Coast); *Journal of Hydrology*; Vol. 151: pp. 173–191.

Chiew F. H. S., Whetton P. H., McMahon T. A. & Pittock A. B. (1995): Simulation of the impacts of climate change on runoff and soil moisture in Australian catchments; *Journal of Hydrology*; Vol. 167: pp. 121–147.

Chow V. T., Maidment D. R. & Mays L. W. (1988): Applied Hydrology; Mc Graw Hill Book Company.

Cook K. H. (1999): Generation of the African Easterly Jet and its role in determining West African precipitation; *Journal of Climate*; Vol. 12: pp. 1165–1184.

Cubasch U., Meehl G. A., Boer G. J., Stouffer R. J., Dix M., Noda A., Senior C. A., Raper S. & Yap K. S. (2001): Projections of Future Climate Change; Cambridge University Press; In: Climate Change 2001: The scientific basis.

Dickinson R. E., Errico R. M., Giorgi F. & Bates G. T. (1989): A regional climate model for the western United States; *Climate Change*; Vol. 15: pp. 383–422.

DKRZ (1993): The ECHAM3 Atmospheric General Circulation Model; techreport No. 6; Deutsches Klimarechenzentrum.

Dodd D. E. S. & Jolliffe I. T. (2001): Early detection of the start of the wet season in semiarid tropical climates of western Africa; *Journal of Climate*; Vol. 21: pp. 1251–1262.

Doherty J. (2002): PEST Model-Independent Parameter Estimation; Watermark Numerical Computing, Brisbane/Australia.

Druyan L. M. (1991): The sensitivity of sub-Saharan precipitation to Atlantic SST; *Climate Change*; Vol. 18: pp. 17–36.

Dudhia J., Gill D., Manning K., Wang W., Bruyere C., Wilson J. & Kelly S. (2003): PSU/NCAR Mesoscale Modelling System Tutorial Class Notes and User's Guide, MM5 Modeling System Version 3.

Duffy P., Govindasamy B., Iorio J., Milovich J., Sperber K., Taylor K., Wehner M. & Thompson S. (2003): High resolution simulations of global climate. Part I: Present climate; *Climate Dynamics*; Vol. 21: pp. 371–390.

Duvel J. P. (1990): Convection over Tropical Africa and the Atlantic Ocean during Northern Summer. Part II: Modulation by Easterly Waves; *Monthly Weather Review*; Vol. 118: pp. 1855–1868.

Dyck S. & Peschke G. (1995): Grundlagen der Hydrologie; Verlag für Bauwesen, Berlin.

Eltahir E. A. B. (1996): Role of vegetation in sustaining large-scale atmospheric circulations in the tropics; *Journal of Geophysical Research*; Vol. 101: pp. 4255–4268.

Evans J. P., Oglesby R. J. & Lapenta W. M. (2005): Time series analysis of regional climate model performance; *Journal of Geophysical Research*; Vol. 110: p. 1.23; D04104.

FAO (1971-81): Soil Map of the World; United Nations Food and Agriculture Organization, UNESCO, Paris.

Fink A. H. & Reiner A. (2003): Spatio-temporal variability of the relation between African Easterly Waves and West African squall lines in 1998 and 1999; *Journal of Geophysical Research - Atmospheres*; Vol. 29(14): pp. ACL 5–1 5–17.

Fontaine B., Janicot S. & Moron V. (1995): Rainfall anomaly patterns and wind field signals over West Africa in August (1958-1989); *Journal of Climate*; Vol. 8: pp. 1503–1510.

Forkel R. & Knoche R. (2005): Regional climate change and its impact on photooxidant concentrations in southern Germany: Simulations with a coupled regional climate-chemistry model; *Journal of Geophysical Research*; submitted.

van Genuchten M. T. (1976): A closed-form equation for predicting the hydraulic conductivity of unsaturated soils; *American Journal of Soil Sciences*; Vol. 44(5): pp. 892–898.

Gibson J. K., Kaelberg P., Uppala S., Hernandez A., Nomura A. & Serrano E. (1997): Era description. ECMWF Re-Analysis project report series 1, Reading, UK; techreport.

Giertz S.: (2004): Analyse der hydrologischen Prozesse in den sub-humiden Tropen Westafrikas unter besonderer Berücksichtigung der Landnutzung am Beispiel des Aguima-Einzugsgebietes in Benin; PhD thesis; University Bonn.

Giertz S. & Diekkrueger B. (2003): Analysis of the hydrological processes in a small headwater catchment in Benin (West Africa); *Physics and Chemistry of the Earth*; Vol. 28: pp. 1333–1341.

van de Giesen N. (2001): Characterization of west African shallow flood plains with L- and C-band radar; *Remote Sensing and Hydrology*; pp. 365–367; Proceedings of a symposium held at Santa Fe, New Mexico, USA, IAHS Publ. no. 267.

Giorgi F. (1990): Simulation of regional climate using a limited area model nested in a general circulation model; *Journal of Climate*; Vol. 3: pp. 941–963.

Giorgi F. (2005): Interdecadal variability of regional climate change: implications for the development of regional climate change scenarios; *Meteorology and Atmospheric Physics*; Vol. 89: pp. 1–15.

Giorgi F. & Francisco R. (2000): Evaluating Uncertainties in the Prediction of Regional Climate Change; *Geophysical Research Letters*; Vol. 27(9): pp. 1295–1298.

Giorgi F., Hewitson B., Christensen J., Hulme M., Storch H. V., Whetton P., Jones R., Mearns L. & Fu C. (2001): Regional climate information - evaluation and projections; Cambridge University Press; In: Climate Change 2001: The scientific basis.

Giorgi F. & Mearns L. O. (1999): Introduction to special section: Regional climate modeling revisited; *Journal of Geophysical Research*; Vol. 104: pp. 6335–6352.

Govindan R. B., Vyushin D., Bunde A., Brenner S., Havlin S. & Schnellnhuber H.-J. (2002): Global Climate Models Violate Scaling of the Observed Atmospheric Variability; *Physical Rewiew Letters*; Vol. 89(2): pp. 028.501 1–4.

Green W. H. & Ampt G. A. (1911): Studies on Soil Physics: I. The flow of air and water through soils; *Journal of Agricultural Sciences*; Vol. 4: pp. 1–24.

Grell G. A., Dudhia J. & Stauffer D. R. (1995): A Description of the Fifth-Generation Penn State/NCAR Mesoscale Model (MM5); NCAR technical note; NCAR/TN-398+STR.

Grell G. A., Emeis S., Stockwell W. R., Schönemeyer T., Forkel R., Michalakes J., Knoche R. & Seidl W. (2000): Application of a multiscale, coupled MM5/chemistry model to the complex terrain of the VOTALP valley campaign; *Atmospheric Environment*; Vol. 34: pp. 1435–1453.

Grell G. A. & Kuo Y.-H. (1991): Semiprognostic tests of cumulus parameterization schemes in the middle latitudes; *Monthly Weather Review*; Vol. 119(1): pp. 5–31.

Gu G. & Adler R. F. (2004): Seasonal evolution and variability associated with the West African monsoon system; *Journal of Climate*; Vol. 17: pp. 3364–3377.

Guillobez S. (1993): Le Mohoun, un ancien affluent du Neger: exemple de capture en milieu tropical aride; *Geographie physique*; Vol. 317: pp. 537–542.

Hartmann G. & Bárdossy A. (2005): Investigation of the uncertainty of hydrological modelling for climate change impact assessment; *Regional hydrological impacts of climatic change - impact assessment and decision making, IAHS Publ.*; Vol. 295: pp. 283–293.

Hay L. E., Clark M.-P., Wilby R. L., Gutowski W. J., Leavesley G. H., Pan Z., Arritt R. W. & Takle E. S. (2002): Use of regional climate model output for hydrologic simulations; *Journal of Hydrometeorology*; Vol. 3: pp. 571–590.

Hayward D. & Oguntoyinbo J. (1987): Climatology of West Africa; Hutchinson.

Hodges K. I. & Thorncroft C. D. (1997): Distribution and statistics of African mesoscale convective weather systems based on ISCCP Meteosat imagery; *Monthly Weather Review*; Vol. 125: pp. 2821–2837.

Hodnet M. G. & Tomasella J. (2002): Marked differences between van Genuchten soil-water retention parameters for temperate and tropical soils: New water-retention pedo-functions developed for tropical soils; *Geoderma*; Vol. 108: pp. 155–180.

Hong S.-Y. & Pan H. L. (1996): Nonlocal boundary layer vertical diffusion in a medium-range forecast model; *Monthly Weather Review*; Vol. 124: pp. 2322–2339.

Houghton J. T., Ding Y., Griggs D. J., Noguer M., van der Linden P. J., Dai X., Maskell K. & Johnson C. A. (2001): Climate Change 2001: The scientific basis; Cambridge University Press.

Houghton J. T., Filho L. G. M., Bruce J., Lee H., Callander B. A., Haites E., Harris N. & Maskell K. (1995): Climate Change 1994; Cambridge University Press; Radiative Forcing of Climate Change and an Evaluation of the IPCC IS92 Emission Scenarios.

Hu Z.-Z., Bengtsson L., Röckner E., Christophj M., Bacher A. & Oberhuber J. M. (2001): Impact of global warming on the interannual and interdecadal climate models in a coupled GCM; *Climate Dynamics*; Vol. 17: pp. 361–374.

Hulme M., Doherty R., Ngara T., New M. & Lister D. (2001): African climate change: 1900-2100; *Climate Research*; Vol. 17: pp. 145–168.

Janicot S. (1992): Spatiotemporal variability of West African rainfall, part II: Associated surface and airmass characteristics; *Journal of Climate*; Vol. 5: pp. 499–511.

Jones R. G., Murphy J. M. & Noguer M. (1995): Simulation of climate change over Europe using a nested regional-climate model. Part I: Assessment of control climate, including sensitivity to location of lateral boundaries; *Quarterly Journal of the Royal Meteorological Society*; Vol. 121: pp. 1413–1449.

Jung G. (2001): Niederschlags-Rückkopplungsmechanismen im Volta-Becken; Master thesis; University Innsbruck.

Kamga F. M. (2000): Validation of general circulation climate models and projections of temperature and rainfall changes in Cameroon and some of its neighbouring areas; *Theoretical and Applied Climatology*; Vol. 67: pp. 97–107.

Kendall M. G. (1975): Rank Correlations Methods; Charles Griffin, London.

Klaus D. (1978): Spatial distribution and periodicity of mean annual precipitation south of the Sahara; *Arch. Met. Geophys. Bioklim.*; Vol. B26: pp. 17–27.

Kleinn J. (2002): Climate change and runoff statistics in the Rhine Basin: A process study with a coupled climate-runoff model; No. 14663; ETH Zuerich.

Klemes V. (1993): The problems of the humid tropics - opportunities for reassessment of hydrological methodology; *Hydrology and water management in the humid tropics*; pp. 45–52; Cambridge University Press.

Klemp J. B. & Durran D. R. (1983): An upper boundary condition permitting internal gravity wave radiation in numerical mesoscale models; *Monthly Weather Review*; Vol. 111: pp. 430–444.

Klemp J. B. & Wilhelmson R. B. (1978): The simulation of three-dimensional convective storm dynamics; *Journal of the Atmospheric Sciences*; Vol. 35: pp. 1070–1096.

Kotlarski S., Block A., Boehm U., Jacob D., Keuler K., Knoche R., Rechid D. & Walter A. (2005): Regional climate model simulations as input for hydrological applications: Evaluation of uncertainties; *Advances in Geosciences*; submitted.

Kraus E. B. (1977): Subtropical droughts and cross-equatorial energy-transports; *Monthly Weather Review*; Vol. 105: pp. 1009–1018.

Kunstmann H. & Jung G. (2003): Investigation of feedback mechanisms between soil moisture, land use and precipitation in West Africa; *IAHS Publ. no. 280*; pp. 149–159; Water Ressources Systems - Water Availability and Global Change.

KUNSTMANN H., KRAUSE J. & MAYR S. (2005): Inverse distributed hydrological modeling of alpine catchments; *Hydrology and Earth System Sciences Discussions*; Vol. 2: pp. 1–43.

KUNSTMANN H., SCHNEIDER K., FORKEL R. & KNOCHE R. (2004): Impact analysis of climate change for an Alpine catchment using high resolution dynamic downscaling of ECHAM4 time slices; *Hydrology and Earth System Sciences*; Vol. 8(6): pp. 1030–1043.

KUNSTMANN H. & STADLER C. (2003): Gekoppelte hochaufgelöste Meteorologie-Hydrologie Simulationen für das alpine Einzugsgebiet der Mangfall; *Hydrologie und Wasserbewirtschaftung*; Vol. 47: pp. 151–158.

LAMB P. J. (1978a): Case studies of tropical Atlantic surface circulation patterns associated with sub-Saharan weather anomalies: 1967 and 1968; *Monthly Weather Review*; Vol. 106: pp. 482–491.

LAMB P. J. (1978b): Large-scale tropical Atlantic surface circulation patterns associated with sub-Saharan weather anomalies; *Tellus*; Vol. 30: pp. 240–251.

LARE A. R. & NICHOLSON S. E. (1994): Contrasting conditions of surface water balance in wet years and dry years as a possible land surface-atmosphere feedback mechanism in the West African Sahel; *Journal of Climate*; Vol. 7: pp. 653–668.

LAUX P., KUNSTMANN H. & BÁRDOSSY A. (2005): Analysis of the onset of the rainy season in Ghana; *2nd GLOWA Status Conference, May 17th-19th, Cologne*; poster presentation.

LEAVESLEY G. H., HAY L. E., CLARK M. P., W. J. GUTOWSKI J. & WILBY R. L. (2005): Statistical and dynamical downscaling of atmospheric model outputs: A hydrological modeler's perspective; presentation held at the ISSOAS (International Summer School on Atmospheric and Oceanic Sciences) on 'Hydrological modelling and water cycle. Coupling of the atmospheric and hydrological models', l'Aquila, Italy.

LEBARBÉ L. & LEBEL T. (1997): Rainfall climatology of the HAPEX-Sahel rgion during the years 1950-1990; *Journal of Hydrology*; Vol. 188-189: pp. 43–73.

LEBARBÉ L., LEBEL T. & TAPSOBA D. (2002): Rainfall variability in West Africa during the years 1950-90; *Journal of Climate*; Vol. 15: pp. 187–202.

LEBEL T., DELCLAUX F., BARBÉ L. L. & POLCHER J. (2000): From GCM scales to hydrological scales: rainfall variability in West Africa; *Stochastic Environment Research and Risk Assessment*; Vol. 14: pp. 275–295.

LEBEL T. & VISCHEL T. (2005): Climat et cycle de l'eau en zone tropicale: un probleme d'echélle; *C. R. Geosciences*; Vol. 337: pp. 29–38.

LEROUX M. (2001): The Meteorology and Climate of Tropical Africa; Springer-Verlag Berlin Heidelberg New York.

LIU C. & MONCRIEFF M. W. (2004): Explicit Simulations of the Intertropical Convergence Zone; *Journal of the Atmospheric Sciences*; Vol. 61: pp. 458–473.

Louis J. F. (1979): A parametric model of vertical eddy fluxes in the atmosphere; *Boundary Layer Meteorology*; Vol. 17: pp. 187–202.

Machenhauer B., Windelband M., Botzet M., Jones R. & Déqué M. (1996): Validation of present-day regional climate simulations over Europe: Nested LAM and variable resolution global model simulations with observed or mixed layer ocean boundary conditions; techreport No. 275; Max-Planck-Institute for Meteorology.

Maidment D. R. (1993): Handbook of Hydrology; McGraw Hill Inc.

Martin N.: (2005): Development of a water balance for the Atankwidi catchment, West Africa - A case study of groundwater recharge in a semi-arid climate; PhD thesis; Georg-August-Universität Göttingen.

Martin N. & van de Giesen N. (2005): Spatial distribution of groundwater production and development potential in the Volta river basin of Ghana and Burkina Faso; *Water International*; Vol. 30(2): pp. 239–249.

de Martonne E. (1920): L'indice d'aridité; *Géographie Physique*; pp. 3–5; Paris, France: Armand Colin, 3rd. ed.

Marx A. (2003): Mit SEBAL ermittelte Wärmeströme aus NOAA-AVHRR-Daten und Vergleich mit Szintillometer- und MM5-Daten in der Savannenzone Ghanas; Master thesis; Universität Trier.

May W. & Röckner E. (2001): A time-slice experiment with the ECHAM4 AGCM at high resolution: the impact of horizontal resolution on annual mean climate change; *Climate Dynamics*; Vol. 17: pp. 407–420.

Maynard K., Royer J.-F. & Chauvin F. (2002): Impact of greenhouse warming on the West African summer monsoon; *Climate Dynamics*; Vol. 19: pp. 499–514.

Mbagwu J. S. C. (1997): Quasi-steady infiltration rates of highly permeable tropical moist savannah soils in relation to landuse and pore size distribution; *Soil Technology*; Vol. 11: pp. 185–195.

Miller M. J., Palmer T. N. & Swinbank R. (1989): Parameterization and influence of sub-grid scale orography in general circulation and numerical weather prediction models; *Meteorology and Atmospheric Physics*; Vol. 40: pp. 84–109.

Monteith J. L. (1975): Vegetation and the Atmosphere, vol. 1: Principles; Academic Press, London.

Moron V., Navarra A., Ward M. N. & Röckner E. (1998): Skill and reproducibility of seasonal rainfall patterns in the tropics in ECHAM4 GCM simulations with prescribed SST; *Climate Dynamics*; Vol. 14: pp. 83–100.

Nakicenovic N. (2000): Special report on emission scenarios; IPCC.

Nash J. E. & Sutcliff J. V. (1970): River flow forecasting through conceptual models. Part I - a discussion of principles; *Journal of Hydrology*; Vol. 10(3): pp. 282–290.

Neumann R. (2005): Stochastische hydrologische Simulationen; Master thesis; Fachhochschule Regensburg.

Neumann R., Jung G., Laux P. & Kunstmann H. (2005): Climate trends of temperature, precipitation and river discharge in the Volta Basin of West Africa; *Journal of River Basin Management*; accepted.

Nicholson S. E. (1980): The nature of rainfall fluctuations in subtropical West Africa; *Monthly Weather Review*; Vol. 108: pp. 473–487.

Nicholson S. E. (1993): An overview of African rainfall fluctuations of the last decade; *Journal of Climate*; Vol. 6: pp. 1463–1466.

Nicholson S. E. (2000): Land surface processes and sahel climate; *Reviews in Geophysics*; Vol. 38: pp. 117–139.

Nicholson S. E. (2001): Climatic and environmental change in Africa during the last two centuries; *Climate Research*; Vol. 17: pp. 123–144.

Nicholson S. E. & Grist J. P. (2001): A conceptual model for understanding rainfall variability in the West African Sahel on interannual and interdecadal timescales; *International Journal of Climatology*; Vol. 21: pp. 1733–1757.

Niehoff D.: (2001): Modellierung des Einflusses der Landnutzung auf die Hochwasserentstehung in der Mesoskala; PhD thesis; Universität Potsdam.

Nijssen B., O'Donnell G. M., Hamlet A. F. & Lettenmaier D. P. (2001): Hydrologic sensitivity of global rivers to climate change; *Climatic Change*; Vol. 50: pp. 143–175.

Nobre P., Moura A. D. & Sun L. (2001): Dynamical downscaling of seasonal climate prediction over nordeste Brazil with ECHAM3 and NCEP's regional spectral models at IRI; *Bulletin of the American Meteorological Society*; Vol. 82: pp. 2787–2796.

Obeng-Asiedu P.: (2004): Allocting water ressources for agricultural and economic development in the Volta river basin; PhD thesis; University Bonn.

Oberhuber J. M. (1993): Simulation of the Atlantic circulation with a coupled sea ice-mixed layer-isopycnal general circulation model. Part I: Model description; *Journal of Physical Oceanography*; Vol. 23: pp. 808–829.

Oguntunde P. G. (2004): Evapotranspiration and complimentarity relations in the water balance of the Volta Basin: Field measurements and GIS-based regional estimates; Ecology and Development Series No. 22; Cuvillier Verlag Göttingen.

Oke T. R. (1987): Boundary Layer Climates; Routledge, London.

Opoku-Ankomah Y. & Amisigo B. A. (1998): Rainfall and runoff variability in the southwestern river system of Ghana; *IAHS Publ.*; (252): pp. 307–314; In: Water resources variability in Africa during the XXth century (Proceedings of the Abidjan '98 conference, Côte d'Ivoire, November 1998).

Ottlé C., Etchevers P., Gonzales C., Habets F., Noilhan J., Martin E., Ledoux E., Leblois E., LSauquet E., Amraoui N., Artinian E., Champeaux J. L., Guérin C., Lacarrère P., le Moigne P., Saulnier G. M., Thiéry D., Vidal-Madjar D. & Voirin S. (2001): Hydro-meteorological modelling of the Rhone Basin: General presentation and objectives; *Physics and Chemistry of the Earth*; Vol. 26(5-6): pp. 443–453.

Paeth H., Born K., Podzun R. & Jacob D. (2005): Regional dynamical downscaling over West Africa: model evaluation and comparison of wet and dry years; *Meteorologische Zeitschrift*; Vol. 14: pp. 349–367.

Paeth H. & Friederichs P. (2004): Seasonality and time scales in the realtionship between global SST and African rainfall; *Climate Dynamics*; Vol. 23: pp. 815–837.

Paeth H. & Hense A. (2004): SST versus climate change signals in West African rainfall: 20th century variations and future projections; *Climate Change*; Vol. 65: pp. 179–208.

Paturel J. E., Ouedraogo M. & Mahe G. (2003): The influence of distributed input data on the hydrological modelling of monthly river flow regimes in West Africa; *Hydrological Sciences Journal*; Vol. 48(6): pp. 881–890.

Peixoto J. P. & Oort A. H. (1992): Physics of Climate; American Institute of Physics (AIP), New York.

Penlap E. K., Matulla C., Storch H. V. & Mkankam F. K. (2003): Empirical downscaling in the tropics - possible changes of the little rainy season (March-June) in Cameroon; *GKSS*; Vol. 11.

Peugeot C., Esteves M., Rajot J. L., Vandervaere J. P. & Galle S. (1997): Runoff generation processes: results and analysis of field data collected at the central supersite of the Hapex-Sahel experiment; *Journal of Hydrology*; pp. 188–189; 179–202.

Phadnis M. J., Robe F. R., Klausmann A. M. & Scire J. S. (2003): Importance of the spatial resolution of sea-surface-temperature data in meteorological modeling; paper presented at the thirteenth PSU/NCAR mesoscale model users' workshop, NCAR.

Pichler H. (1997): Dynamik der Atmosphäre; Spektrum Akademischer Verlag GmbH.

Pielke R. A. (1984): Mesoscale Meterological modeling; Academic Press, New York.

Ramaswamy V., Boucher O., Haigh J., Hauglustaine D., Haywood J., Myhre G., Nakajima T., Shi G. Y. & Solomon S. (2001): Radiative Forcing of Climate Change; Cambridge University Press; In: Climate Change 2001: The scientific basis.

Redelsperger J.-L., Diongue A., Diedhiou A., Ceron J.-P., Diop M., Gueremy J.-F. & Lafore J.-P. (2002): Multi-scale description of a Sahelian synoptic weather system representative of the West African monsoon; *Quarterly Journal of the Royal Meteorological Society*; Vol. 128: pp. 1229–1257.

Reisner J., Rasmussen R. M. & Bruintjes R. T. (1998): Explicit forecasting of supercooled liquid water in winter storms using the MM5 mesoscale model; *Quarterly Journal of the Royal Meteorological Society*; Vol. 124: pp. 1071–1107.

Rockel B., Raschke E. & Weyres B. (1991): A parameterization of broad band radiative transfer properties of water, ice and mixed clouds; *Beiträge zur Physik der Atmosphäre*; Vol. 64: pp. 1–12.

Roux F. & Testud J. (1984): West African Squall-Line Thermodynamic Structure Retrieved from Dual-Doppler Radar Observations; *Journal of the Atmospheric Sciences*; Vol. 41(21): pp. 3104–3121.

Rowell D. P., Folland C. K., Maskell K. & Ward M. N. (1995): Variability of summer rainfall over tropical North-Africa (1906-92) - Observations and modelling; *Quarterly Journal of the Royal Meteorological Society*; Vol. 121(523): pp. 669–704; Part A.

Röckner E., Bengtsson L. & Feichter J. (1999): Transient climate change simulations with a coupled atmosphere-ocean GCM including the tropospheric sulfur cycle; *Journal of Climate*; Vol. 12: pp. 3004–3032.

Salathé E. P. (2005): Downscaling simulations of future global climate with application to hydrologic modelling; *International Journal of Climatology*; Vol. 25: pp. 419–436.

Schneider K. (2004): Anwendung von regionalisierten ECHAM4 Klimaszenarien auf das Wasserhaushaltsmodell WaSiM-ETH zur Abschätzung der Folgen von Klimaänderungen in einem alpinen Einzugsgebiet; Master thesis; LMU München.

Schnitzler K. G., Knorr W., Latif M., Bader J. & Zeng N. (2001): Vegetation feedback on Sahelian rainfall variability in a coupled climate land-vegetation model; techreport No. 329; Max-Planck-Institute for Meteorology.

Schulla J. (1997): Hydrologische Modellierung von Flussgebieten zur Abschätzung der Folgen von Klimaänderungen; Zürcher Geographische Schriften No. 69; Verlag Geograph. Institut, ETH Zürich.

Schulla J. (2005): personal conversation.

Schulla J. & Jasper K. (2002): Model Description WaSiM-ETH; techreport; ETH Zürich.

Schäfli B.: (2005): Quantification of modelling uncertainties in climate change impact studies on water resources: Application to a glacier-fed hydropower production system in the Swiss Alps; PhD thesis; École Polytechnique Fédérale de Lausanne, EPFL.

Sellers P. J., Mintz Y., Sud Y. C. & Dalcher A. (1986): A simple biosphere model (Sib) for use within general circulation models; *Journal of the Atmospheric Sciences*; Vol. 43: pp. 505–531.

Servant E., Patureel I., Kouamé B., Ouédraogo T., Boyer J.-F., Lubés-Neil H., Fritsch J.-M., Masson J.-M. & Marieu B. (1998): Identification, characterisation and consequences of a hydrological variability in West and Central Africa; pp. 307–314; In: Proc. Int. Conf. at Abidjan on the variability of water ressources in Africa in the 20th century, IAHS Publ. no. 252.

Shahin M. (2002): Hydrology and Water Ressources of Africa; Vol. 41 of *Water Science and Technology Library*; Kluwer Academic Publisher.

Shukla J. (1998): Predictability in the midst of chaos: A scientific basis for climate forecasting; *Science*; Vol. 282: pp. 728–731.

Singh V. P. & Frevert D. K. (2002): Mathematical Models of Large Watershed Hydrology; Water Resources Publications, LLC.

Skamarok W. C. & Klemp J. B. (1994): The stability of time-split numerical methods for the hydrostatic and nonhydrostatic elastic equations; *Monthly Weather Review*; Vol. 120: pp. 2109–2127.

van der Sommen J. J. & Geirnaert W. (1988): On the continuity of aquifer systems on the crystalline basement of Burkina Faso; NATO ASI Series: Mathem. and Phys.Sci., Vol.222; D. Reidel Publishing Company; In: Estimation of natural groundwater rechage.

Stehlík J. & Bàrdossy A. (2002): Multivariate stochastic downscaling model for generating daily precipitation series based on atmospheric circulation; *Journal of Hydrology*; Vol. 256: pp. 120–141.

Stern R. D., Dennett M. D. & Garbutt D. J. (1981): The start of the rains in West Africa; *Journal of Climatology*; Vol. 1: pp. 59–68.

Sultan B. & Janicot S. (2000): Abrupt shift of the ITCZ over West Africa and intraseasonal variability; *Geophysical Research Letters*; Vol. 27: pp. 3353–3356.

Sultan B. & Janicot S. (2003): The West African Monsoon Dynamics. PartII: The "Preonset" and "Onset" of the Summer Monsoon; *Journal of Climate*; Vol. 16(21): pp. 3407–3427.

Sundquist H. (1978): A parameterization scheme for non-convective condensation including prediction of cloud water content; *Quarterly Journal of the Royal Meteorological Society*; Vol. 104: pp. 677–690.

Tiedtke M. (1989): A comprehensive mass flux scheme for cumulus parameterization in large-scale models; *Monthly Weather Review*; Vol. 117: pp. 1779–1800.

Vescovi F. D. (2001): Classification of African complex environments based on a contextual spatial approach (SPARK); international workshop on Geo-Spatial Knowledge Processing for Natural Resource Management. June 28-29, University of Insubria, Varese (Italy).

Vizy E. K. & Cook K. H. (2001): Mechanisms by which Gulf of Guinea and eastern North Atlantic sea surface temperature anomalies influence African rainfall; *Journal of Climate*; Vol. 14: pp. 795–821.

Vizy E. K. & Cook K. H. (2002): Development and application of a mesoscale climate model for the tropics: Influence of sea surface temperature anomalies on the West African monsoon; *Journal of Geophysical Research - Atmosphere*; Vol. 107: pp. ACL – 2 1–21.

Vollmert P., Fink A. H. & Besler H. (2003): Ghana Dry Zone und Dahomey Gap: Ursachen für eine Niederschlagsanomalie im tropischen Westafrika; *Beitrag zur physischen Geographie*; Vol. 4: pp. 375–393.

Walker J. & Rowntree P. R. (1977): The effect of soil moisture on circulation and rainfall in a tropical model; *Quarterly Journal of the Royal Meteorological Society*; Vol. 103: pp. 29–46.

Wang G. & Eltahir E. A. B. (2000): Role of vegetation dynamics in enhancing the low-frequency variability of the Sahel rainfall; *Water Resources Research*; Vol. 36: pp. 1013–1021.

Wang Y., Leung L. R., McGregor J. L., Lee D.-K., Wang W.-C., Ding Y. & Kimura F. (2004): Regional climate modeling: Progress, challenges and prospects; *Journal of the Meteorological Society of Japan*; Vol. 82(6): pp. 1599–1628.

Warner T. T., Peterson R. A. & Treadon R. E. (1997): A tutorial on lateral boundary conditions as a basic and potentially serious limitation to regional numerical weather prediction; *Bulletin of the American Meteorological Society*; Vol. 78: pp. 2599–2617.

Washington R., Harrison M. & Conway D. (2004): African Climate Report - A report commissioned by the UK Government to review African climate science, policy and options for action; techreport; contacts: D. Brew and R. Washington.

Weisman M. L. & Rotunno R. (2004): "A theory for strong long-lived squall lines" revisited; *Journal of the Atmospheric Sciences*; Vol. 61(4): pp. 361–382.

WHO (2005): http:
www3.who.int/whosis/country.

Williamson D. L. & Rasch P. J. (1994): Water-vapor transport in the NCAR-CCM2; *Tellus Series A - Dynamic Meteorology and Oceanography*; Vol. 46(1): pp. 34–51.

WMO (2002): WMO statement on the status of the global climate in 2001; techreport 940; ISBN 92-63-10940-0.

Zheng X. & Eltahir E. A. B. (1997): The response to deforestation and desertification in a model of West African monsoons; *Geophysical Research Letters*; Vol. 24: pp. 155–158.